Supplementary Material for Report 32: Age groups that sustain resurging COVID-19 epidemics in the United States

Mélodie Monod*, Alexandra Blenkinsop*, Xiaoyue Xi*, Daniel Hebert*, Sivan Bershan*, Simon Tietze*, Valerie C Bradley, Yu Chen, Helen Coupland, Sarah Filippi, Jonathan Ish-Horowicz, Martin McManus, Thomas Mellan, Axel Gandy, Michael Hutchinson, H Juliette T Unwin, Michaela A C Vollmer, Sebastian Weber, Harrison Zhu, Anne Bezancon, Neil M Ferguson, Swapnil Mishra, Seth Flaxman, Samir Bhatt, and Oliver Ratmann[1,*], on behalf of the Imperial College COVID-19 Response Team

Department of Mathematics, Imperial College London
Foursquare Inc.
Emodo Inc.
Department of Infectious Disease Epidemiology, Imperial College London
WHO Collaborating Centre for Infectious Disease Modelling
MRC Centre for Global Infectious Disease Analytics
Abdul Latif Jameel Institute for Disease and Emergency Analytics, Imperial College London
Novartis Pharma AG, Basel, Switzerland
Department of Statistics, University of Oxford

*Contributed equally.
[1]Correspondence: oliver.ratmann@imperial.ac.uk

DOI: https://doi.org/10.25561/82551

Contents

DOI: https://doi.org/10.25561/82551

S1 Supplementary Text: National mobility indicators during the pandemic

S1.1 Age-specific U.S. foot traffic

To characterise changes in human contact patterns during the pandemic, Foursquare Labs Inc. provided longitudinal U.S. foot traffic data across the 50 U.S. states, the District of Columbia, and New York City [1]. The data are based on Foursquare's US first-party panel that includes millions of opt-in, always-on active users. Visits are derived via Foursquare's core location technology, Pilgrim [2], which leverages a variety of mobile device signals to pinpoint the time, duration, and location of panelists' visits to locations such as shops, malls, restaurants, concert venues, theaters, parks, beaches, or universities. From operated and partner apps, Foursquare Labs Inc. collect a variety of device signals against opted-in users. These include intermittent device GPS coordinate pings, WiFi signals, cell signal strength, device model, and operating system version. Additionally, a smaller set of labeled explicit check-ins are captured from a portion of the user panel. Check-ins are explicit confirmations that a user was at a given venue at a given point of time. One example source of this is Foursquare's Swarm app, where users can "check in" to venues to keep a log of where their mobility history. These check-ins then serve as training labels for a non-linear model that is used to predict visits among users with unlabeled visits in terms of probabilities as to which venue users ultimately visited. For research and insights use cases, the probabilities are processed further, projected and aggregated by state / metropolitan area, day, and age cohort. This projection accounts for changes in the number of individuals in the panel and the representativeness of panelists according to their home state or metropolitan area, age band, and gender relative to latest US Census data.

Daily projected visit volumes were available at state / metropolitan area-level from February 1, 2020 to August 21, 2020 for individuals for 6 age groups

$$\tilde{a} \in \tilde{\mathcal{A}} = \Big\{[18-24], [25-34], [35-44], [45-54], [55-64], [65+]\Big\}. \tag{S1}$$

Daily projected visit volumes were standardised to projected per capita visits $V_{m,t,\tilde{a}}$ of individuals in state / metropolitan area m and age band $\tilde{a}$ on day t by dividing the visit volumes with the number of individuals in state / metropolitan area m and age band $\tilde{a}$. Per capita visits appeared low for the first two days of the time series, and were excluded. Data updates were obtained from May 26 onwards. Per capita visits appeared low for May 25, and were replaced with the values from May 24.

Figure S11 illustrates the pre-processed time series of projected per capita visits $V_{m,t,\tilde{a}}$. Individuals in New York City, New York, and Hawai were projected to have considerably more per capita visits than other states and metropolitan areas. Across states and metropolitan areas, projected per capita visits were highest for individ-

uals aged $35-44$ years, both before and after stay at home orders were issued. Individuals aged 65 or older had lowest projected per capita visits across all states and metropolitan areas.

S1.2 Age-specific U.S. mobility trends

Age-specific mobility trends were derived from the U.S. foot traffic data described in Section S1.1. Our aim was to quantify changes in U.S. foot traffic during the pandemic relative to a baseline period for individuals in the 5-year age bands (S10) in each of the U.S. states, the District of Columbia, and New York City. The baseline period was defined from February 3 to February 9, 2020, which corresponded to the first week of the time series of projected per capita visits. We first calculated average projected per capita visits during the baseline week,

$$V_{m,\tilde{a}}^{\text{base}} = \sum_{t \in \{\text{Feb 3}-\text{Feb 9}\}} V_{m,t,\tilde{a}} \tag{S2}$$

and then derived the mobility trends

$$X_{m,t,\tilde{a}} = V_{m,t,\tilde{a}} / V_{m,\tilde{a}}^{\text{base}} \tag{S3}$$

for each state / metropolitan area m and the age bands $\tilde{a}$ available through the U.S. foot traffic data.

S1.3 Quantitative Analysis

To characterise different effects during the initial phase of the pandemic, the time when stay at home orders were introduced, and later time periods, we derived two particular time points for each state or metropolitan area. The first time point characterises the start of substantial declines in mobility across all age groups, and the second time point characterises the time after which mobility trends begin to rebound. To determine the two time points we calculated the 15-days central moving average of projected per capita visits in each location (state or metropolitan area) m,

$$X_{m,t}^{\text{m-avg}} = \frac{1}{30+1} \frac{1}{\tilde{A}} \sum_{s=-15}^{15} \sum_{\tilde{a}} X_{m,t+s,\tilde{a}}, \tag{S4}$$

where $\tilde{A}$ is the number of age groups in the mobility data specified in (S1), such that $\tilde{A} = 6$. The first time point, which we refer to as the dip date, was determined as the first day when the 15-days moving-average had fallen by over 10% compared to the one two weeks prior,

$$t_m^{\text{dip}} = \min\left\{t : X_{m,t}^{\text{m-avg}} / X_{m,t-14}^{\text{m-avg}} < 0.9\right\}. \tag{S5}$$

Figure S11: **Projected per person foot traffic per day for the 50 US states, District of Columbia and New York City.** Data were obtained using Foursquare's location technology Pilgrim that pinpoints the time, duration, and location of panelist's visits.

The second time point, which we refer to as the rebound date, was determined as the day with the smallest 15-days moving-average,

$$t_m^{\text{rebound}} = \text{argmin}_{t > t_m^{\text{dip}}} X_{m,t}^{\text{m-avg}}, \tag{S6}$$

where $t_m^{\text{dip}} < t_m^{\text{rebound}}, \forall m$. Using different time intervals in the central moving average calculations did not alter the value of change points substantially (not shown). Figure S12 shows the mobility trends (S3) for every U.S. state, the District of Columbia, and New York City, along with the dip and rebound dates.

We then assessed differences in the age-specific mobility trends around the rebound date when compared to the baseline week in early February, and similarly in the last observation week when compared to the baseline week. To do this, age-specific mobility trends were selected from the calendar week that included the rebound date. Then, Gamma regression models with log link, and location and age category interaction terms were fitted to the selected daily mobility trends. Negative regression coefficients with a two-sided p-value below 0.05 were interpreted as age groups showing statistically significantly lower mobility compared to the baseline week. Similarly, positive regression coefficients with a two-sided p-value below 0.05 were interpreted as age groups showing statistically significantly higher mobility compared to the baseline week, and regression coefficients with a two-sided p-value above 0.05 were interpreted as age groups showing mobility trends that were not significantly different compared to the baseline week. Figure S13 (left) summarises the results. In the rebound week, mobility was significantly lower when compared to the baseline week across all age groups and all locations.

We repeated the analysis for the last observed calendar week (Aug 10-Aug 16). In the last week, there was substantial variation in mobility trends when compared to baseline. Among individuals aged 18-24, mobility had remained significantly lower when compared to baseline in 42 (80.8%) states or metropolitan areas, was not significantly different when compared to baseline in 6 (11.5%) states or metropolitan areas, and significantly above baseline in 4 (7.7%) states or metropolitan areas. Among individuals aged 25-34, mobility had remained significantly lower when compared to baseline in 29 (55.8%) states or metropolitan areas, was not significantly different when compared to baseline in 17 (32.7%) states or metropolitan areas, and significantly above baseline in 6 (11.5%) states or metropolitan areas. Among individuals aged 35-44, mobility had remained significantly lower when compared to baseline in 25 (48.1%) states or metropolitan areas, was not significantly different when compared to baseline in 20 (38.5%) states or metropolitan areas, and significantly above baseline in 7 (13.5%) states or metropolitan areas. Among individuals aged 44-54, mobility had remained significantly lower when compared to baseline in 22 (42.3%) states or metropolitan areas, was not significantly different when compared to baseline in 23 (44.2%) states or metropolitan areas, and significantly above baseline in 7 (13.5%) states or metropolitan areas. Among individuals aged 55-64, mobility had remained significantly lower when compared to baseline in 23 (44.2%) states or metropolitan areas, was not significantly different when compared to baseline in 21 (40.4%) states or metropoli-

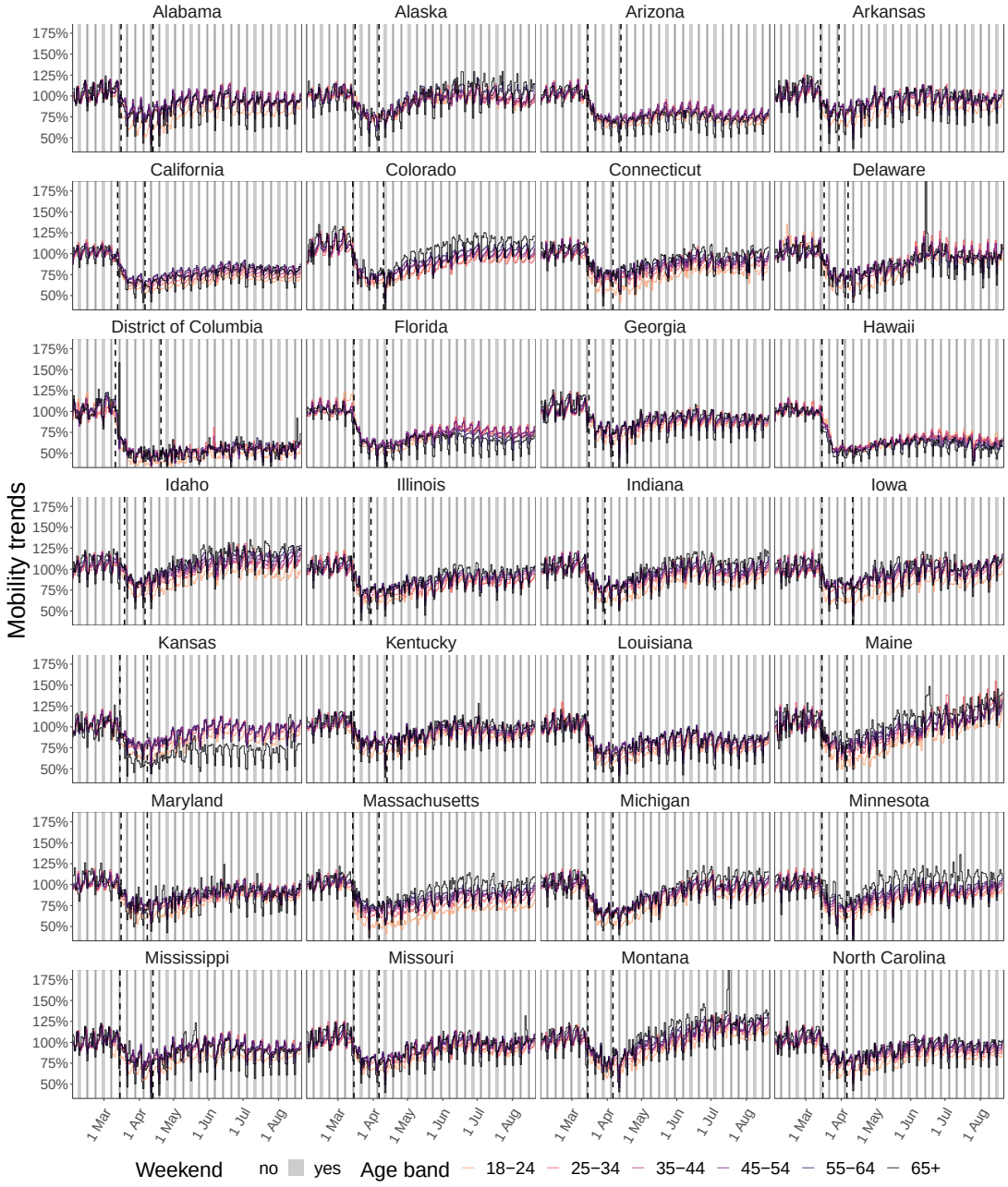

Figure S12: **Mobility trends per person per day for the 50 US states, District of Columbia and New York City (part 1).** Mobility trends quantify change in projected visits relative to the baseline week February 3 to February 9, 2020. The two dashed lines indicate the dip and rebound time, defined respectively in (S5) and (S6).

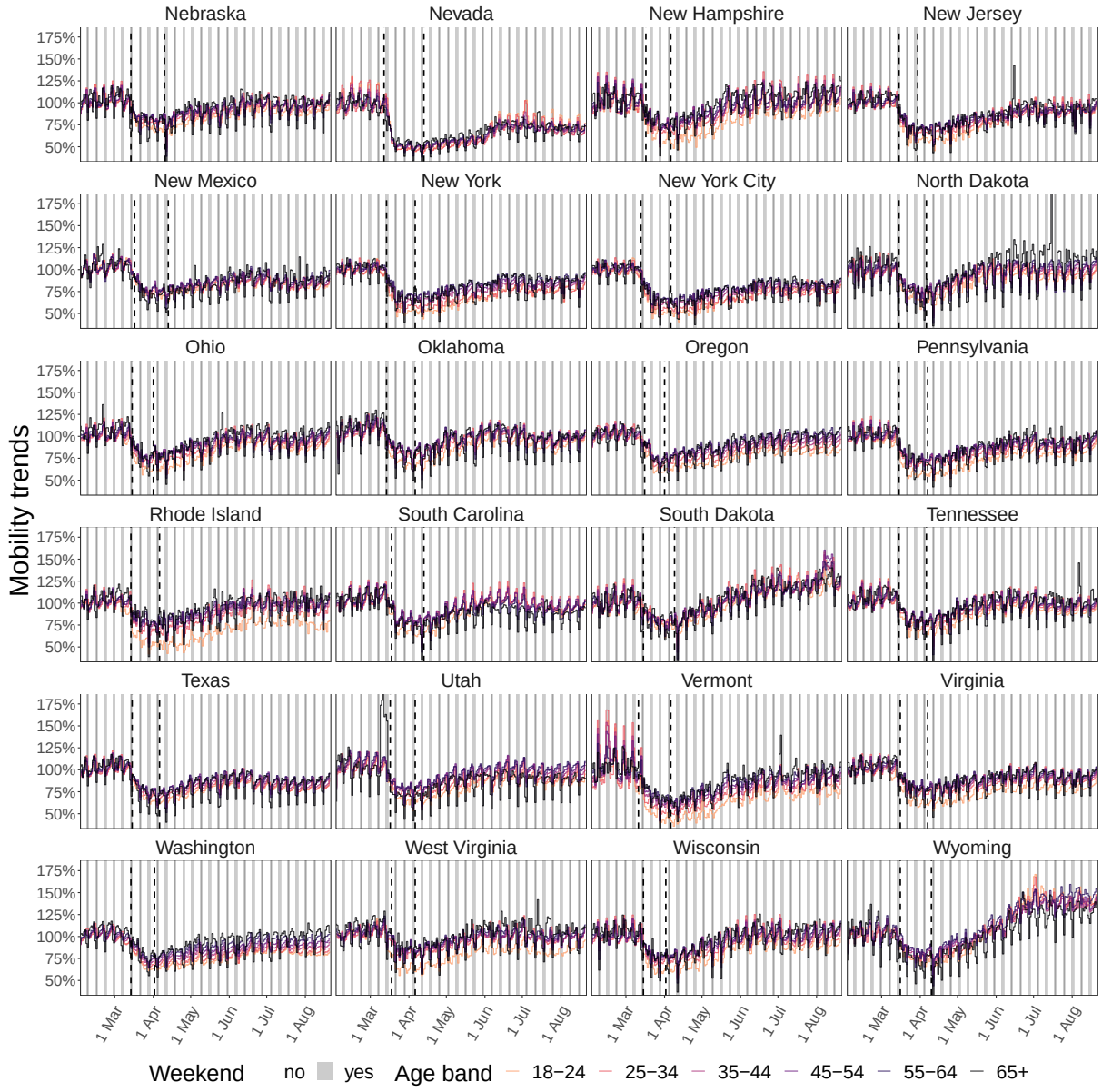

Figure S12: **Mobility trends per person per day for the 50 US states, District of Columbia and New York City (part 2).** Mobility trends quantify change in projected visits relative to the baseline week February 3 to February 9, 2020. The two dashed lines indicate the dip and rebound time, defined respectively in (S5) and (S6).

tan areas, and significantly above baseline in 8 (15.4%) states or metropolitan areas. Among individuals aged $65+$, mobility had remained significantly lower when compared to baseline in 29 (55.8%) states or metropolitan areas,

was not significantly different when compared to baseline in 14 (26.9%) states or metropolitan areas, and significantly above baseline in 9 (17.3%) states or metropolitan areas. This analysis suggests that overall, individuals aged 18-24 continue to limit their mobility substantially when compared to early February. For individuals aged 25 and above, mobility trends are heterogeneous across the United States, with mobility levels remaining below those seen in early February in approximately half of all states or metropolitan areas.

To obtain further insights into age-specific mobility trends between age groups, we repeated the regression analysis using as predictors the contrasts between all age groups and the 35-44 age group. Figure S13 (right) summarises the results. In the rebound week, individuals aged 18-24 had significantly lower mobility trends when compared to individuals aged 35-44 in 49 (94.2%) states or metropolitan areas, similar mobility trends in 2 (3.8%) states or metropolitan areas, and higher mobility trends in 1 (1.9%) states or metropolitan areas. Individuals aged 25-34, 45-54, 55-64 tended to have similar mobility trends when compared to individuals aged 35-44. Individuals aged 65+ tended to have overall significantly lower mobility trends when compared to individuals aged 35-44. Results for the last observed calendar week (Aug 10-Aug 16) are summarised in the last column of Figure S13. In the last week, individuals aged 18-24 had significantly lower mobility trends when compared to individuals aged 35-44 in 20 (38.5%) states, similar mobility trends in 31 (59.6%) states, and higher mobility trends in 1 (1.9%) trends. Individuals aged 25-34, 45-54, 55-64, 65+ tended to have similar mobility trends when compared to individuals aged 35-44. The Foursquare data suggest that

- individuals aged 18-24 reduced their mobility more strongly than individuals aged 35-44 in the initial phase of the pandemic, and continue to be significantly less mobile than individuals aged 35-44 as of the last observation week;
- individuals aged 18-34 have lower or similar, but not significantly higher mobility when compared to individuals aged 35-44 as of the last observation week;
- individuals aged 65+ showed different behaviour. In the initial phase of the pandemic individuals aged 65+ appear to have reduced their mobility significantly more than individuals aged 35-44, however by the last observation week, individuals aged 65+ appear to be as mobile as individuals aged 35-44.

S1.4 Comparison to an independent U.S. mobility trend data set

To substantiate the trends observed in the national Foursquare data set, we evaluated an independent data set of age-stratified mobility indicators that was provided by Emodo. The Emodo data set quantifies the proportion

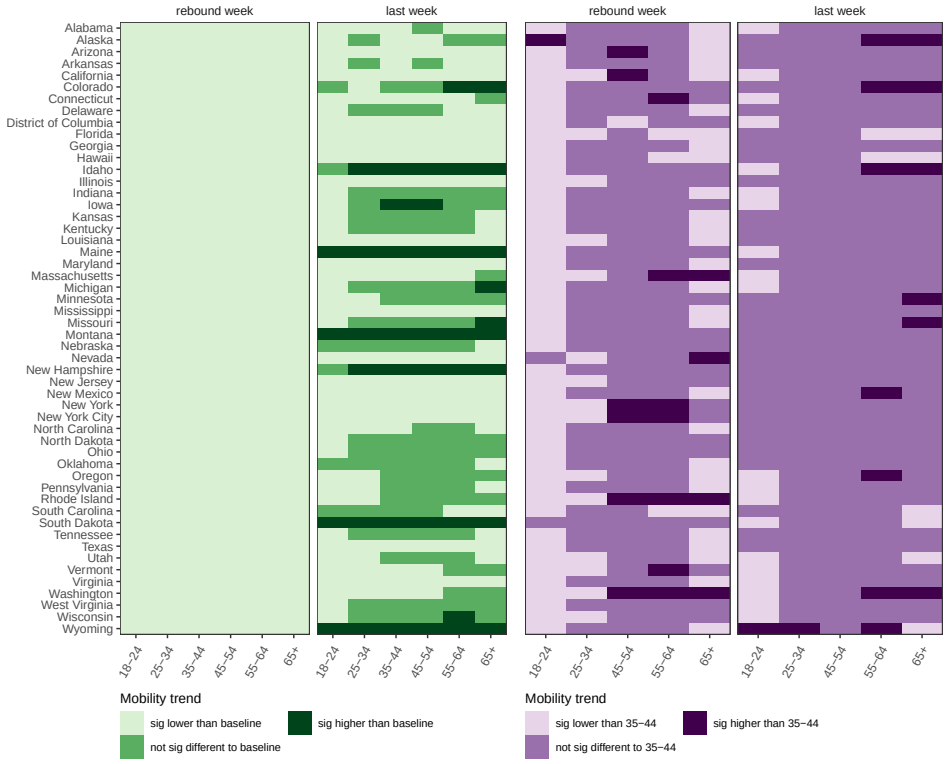

Figure S13: **Statistical analysis of mobility trends.** (**Left**) Mobility trends during the calendar week that includes the rebound date were categorised as statistically significantly lower when compared to the baseline week, not significantly different, and statistically higher. Analysis was repeated for mobility trends during the last complete calendar week. (**Right**) Mobility trends during the calendar week that includes the rebound date were categorised relative to trends among individuals aged $35 - 44$ in the same week. Analysis was repeated for mobility trends during the last complete calendar week.

of individuals with at least one observed ping outside the user's home location, out of a panel of individuals whose GPS enabled devices emitted at least one ping on the corresponding day. The observed, age-specific, daily mobility indicators within the panel were projected to location-level mobility indicators. The projection accounts for changes in the number of individuals in the panel, and the representativeness of panel members in their home area, age band, and gender relative to the latest U.S. Census.

Daily projected mobility indicators $\breve{V}_{m,t,\breve{a}}$ were available at state / metropolitan area-level m from Feb 01 to Jul 26 for individuals between the age groups

$$\breve{a} \in \breve{\mathcal{A}} = \Big\{[18-24], [25-34], [35-44], [45-54], [55+]\Big\}. \tag{S7}$$

To compare the data against the age-specific Foursquare mobility trends (S3), we derived mobility trends similarly as for the Foursquare data. We first calculated average mobility trends during the baseline period,

$$\breve{V}^{\text{base}}_{m,\breve{a}} = \sum_{t \in \{\text{Feb 19} - \text{Mar 03}\}} \breve{V}_{m,t,\breve{a}} \tag{S8}$$

and then derived the mobility trends

$$\breve{X}_{m,t,\breve{a}} = \breve{V}_{m,t,\breve{a}} / \breve{V}^{\text{base}}_{m,\breve{a}} \tag{S9}$$

for each location (states or metropolitan area) m and the age bands $\breve{a}$.

Initial analysis indicated that the mobility trends (S9) were noisy for some locations. For this reason, analysis was limited to location with an average of $20,000$ distinct panelists per day per age band, and the baseline period in (S8) was defined over 14 days. In total, data from 11 locations were used. Figure S14 compares the age-specific mobility trends derived from the Foursquare data to those derived from the Emodo data set. Overall, the trends observed in both data sets were very similar.

The primary aim of this analysis was to assess whether the Emodo data support the above observation that young individuals aged $18-24$ and $25-34$ continue to have mobility trends significantly below or similar to the baseline period, and mobility trends that are not significantly higher than those seen for older individuals. We repeated the analyses presented in Section S1.2, with the last observation week set to the last complete week of observations in both data sets (July 20-July 26). Figure S15 summarises the results. The Emodo data substantiate that individuals aged 18-24 continue to have mobility trends below those seen in the baseline period, and that individuals aged $25-34$ have mobility levels similar to those seen at baseline, and not higher than seen at baseline. We further find the Emodo data support the conclusion that individuals aged 18-24 and $25-34$ have lower or similar mobility levels than individuals aged 34-45, and not higher mobility levels than individuals aged 34-45.

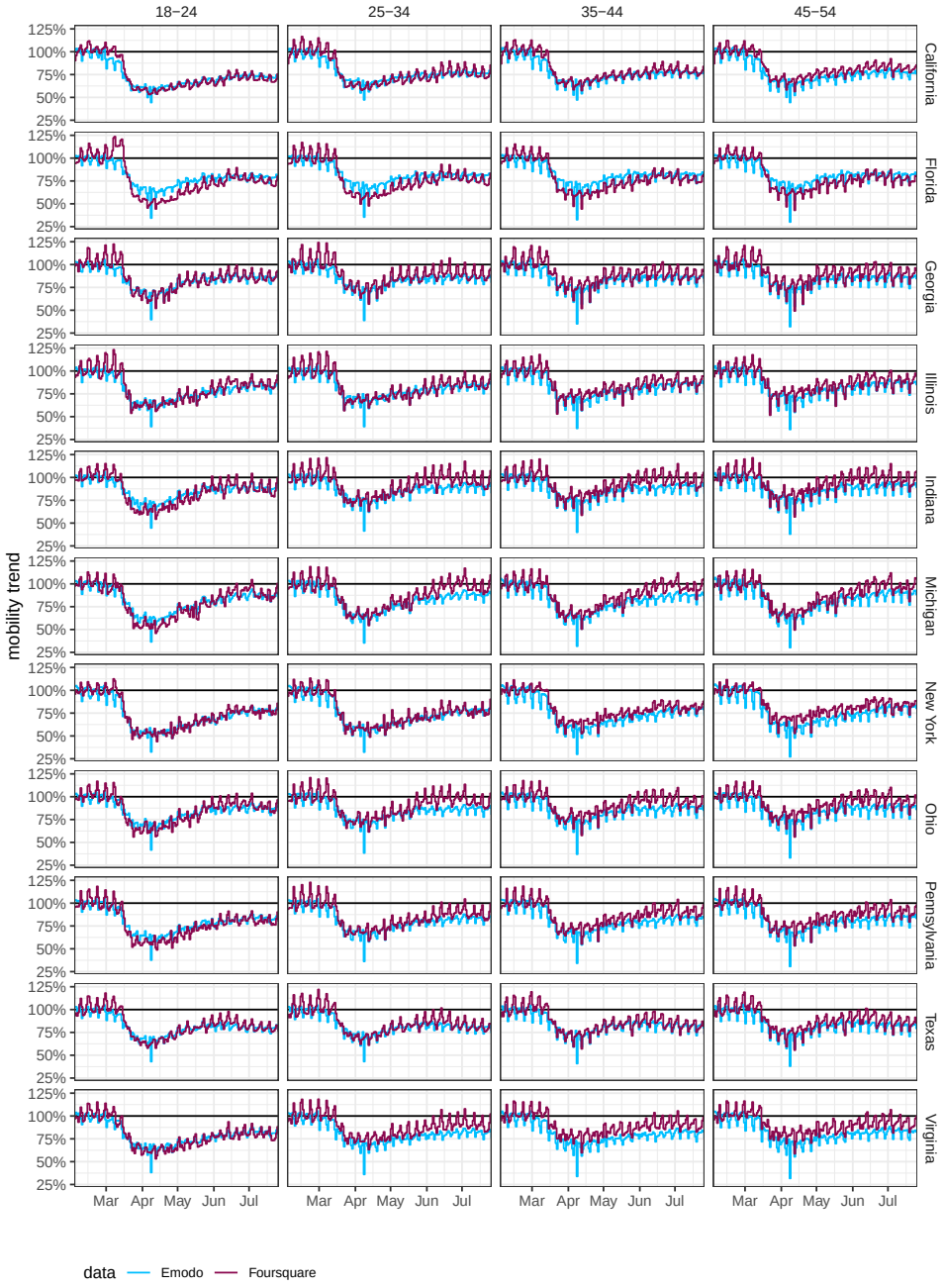

Figure S14: **Comparison of mobility trends derived with Foursquare's location technology and Emodo's mobility data.** The comparison was restricted to identical age bands in the two data sets, a common range of observation days, and states and metropolitan areas with an average of at least $20,000$ panelists per day.

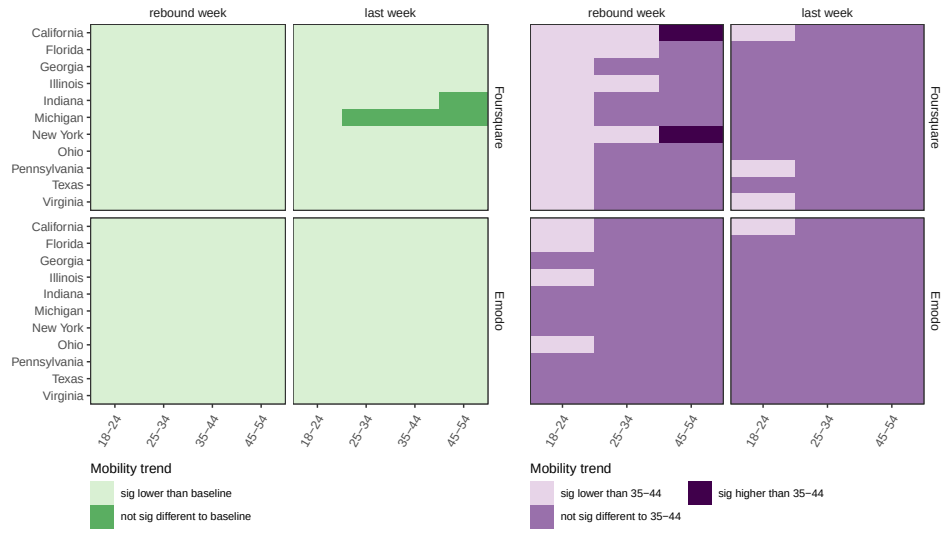

Figure S15: **Statistical analysis of mobility trends in the Foursquare and Emodo data sets.** (**Left**) Considering both data sets, mobility trends during the calendar week that includes the rebound date were categorised as statistically significantly lower when compared to the baseline week, not significantly different, and statistically higher. Analysis was repeated for mobility trends during the last complete calendar week. (**Right**) Considering both data sets, mobility trends during the calendar week that includes the rebound date were categorised relative to trends among individuals aged $35 - 44$ in the same week. Analysis was repeated for mobility trends during the last complete calendar week.

S2 Supplementary Text: Age-specific COVID-19 mortality data

Daily COVID-19 death counts from February 01, 2020 until September 02, 2020 regardless of age were obtained from John Hopkins University (JHU) for all U.S. states and the District of Columbia [3], except New York State. For New York State, daily COVID-19 death counts from February 01, 2020 until September 02, 2020 were obtained from the New York Times' (NYT) data [4]. For New York City, daily COVID-19 deaths counts were obtained from the GitHub Repository [5]. The overall death counts were used for statistical inference prior to when age-specific death counts were reported for each location (state or metropolitan areas).

Age-specific COVID-19 cumulative death counts were retrieved for 40 U.S. states, the District of Columbia and New York City from city or state Department of Health (DoH) websites, data repositories or via data requests to DoH. Table S8 lists our data sources for each location, the date since when age-specific mortality data used in this study was recorded, and the frequency of data updates.

The recorded death counts were processed to create a time series of daily deaths for every location. Some dates had missing data, typically either because no updates were reported, or because reporters changed the age bands in which the mortality data were reported. Missing daily death counts were imputed, assuming a constant increase in daily deaths between two days with data. Some updates displayed a decreasing cumulative death from one day. When this was observed, the daily death count was set to zero and the previous daily death count was reduced by the count difference. Finally, certain age bands declared by the Department of Health could not be directly associated with the age bands used in the analysis, defined in (S10). In this case, the boundaries of these problematic age bands were modified to reflect the closest age band from the analysis. Figure S16 illustrates the age-specific COVID-19 mortality data that were retrieved. To assess the completeness of the age-specific death data, we compared the time evolution of the sum of the age-specific deaths that we retrieved to the time evolution of the overall number of COVID-19 deaths reported by JHU [3] and the New York City Github Repository [5]. Figure S17 confirms that the sum of the age-specific data that we retrieved closely matched the overall death data.

DOI: https://doi.org/10.25561/82551

Location	Date record start	Frequency of updates	Source
Alabama	May 03, 2020	Daily	[6]
Alaska	June 09, 2020	Daily	[7]
Arizona	May 13, 2020	Daily	[8]
Arkansas	-	-	-
California	May 13, 2020	Daily	[9]
Colorado	March 23, 2020	Daily	[10]
Connecticut	April 05, 2020	Daily	[11]
Delaware	May 12, 2020	Daily	[12]
District of Columbia	April 13, 2020	Daily	[13]
Florida	March 27, 2020	Daily	[14]
Georgia	May 06, 2020	Daily	[15]
Hawaii	-	-	-
Idaho	May 13, 2020	Daily	[16]
Illinois	May 14, 2020	Daily	[17]
Indiana	May 13, 2020	Daily	[18]
Iowa	May 13, 2020	Daily	[19]
Kansas	May 13, 2020	Mon, Wed and Fri.	[20]
Kentucky	May 13, 2020	Daily	[21]
Louisiana	May 12, 2020	Daily except Sat.	[22]
Maine	March 12, 2020	Daily	[23]
Maryland	May 14, 2020	Daily	[24]
Massachusetts	April 20, 2020	Daily	[25]
Michigan	March 21, 2020	Daily	[26], [27]
Minnesota	-	-	-
Mississippi	April 27, 2020	Daily	[28]
Missouri	May 13, 2020	Daily	[29]
Montana	-	-	-
Nebraska	-	-	-
Nevada	June 07, 2020	Daily	[30]
New Hampshire	June 07, 2020	Daily	[31]
New Jersey	May 25, 2020	Daily	[32]
New Mexico	March 25, 2020	Daily	[33]
New York	-	-	-
New York City	July 01, 2020	Daily	[34], [5]
North Carolina	May 20, 2020	Daily	[35]
North Dakota	May 14, 2020	Daily	[36]
Ohio	-	-	-
Oklahoma	May 13, 2020	Daily	[37]
Oregon	June 05, 2020	Mon-Fri., sometimes Sat.	[38]
Pennsylvania	June 07, 2020	Daily	[39]
Rhode Island	June 01, 2020	Weekly	[40]
South Carolina	May 14, 2020	Tue and Fri.	[41]
South Dakota	-	-	-
Tennessee	April 09, 2020	Daily	[42]
Texas	July 28, 2020	Daily	[43]
Utah	June 17, 2020	Daily	[44]
Vermont	June 16, 2020	Daily	[45]
Virginia	April 21, 2020	Daily	[46]
Washington	June 08, 2020	Daily	[47]
West Virginia	-	-	-
Wisconsin	March 15, 2020	Daily	[48]
Wyoming	-	-	-

Table S8: **Age-specific Mortality Data source, date of first availability and update frequency by location (state and metropolitan area).** The data are available in the GitHub repository [49].

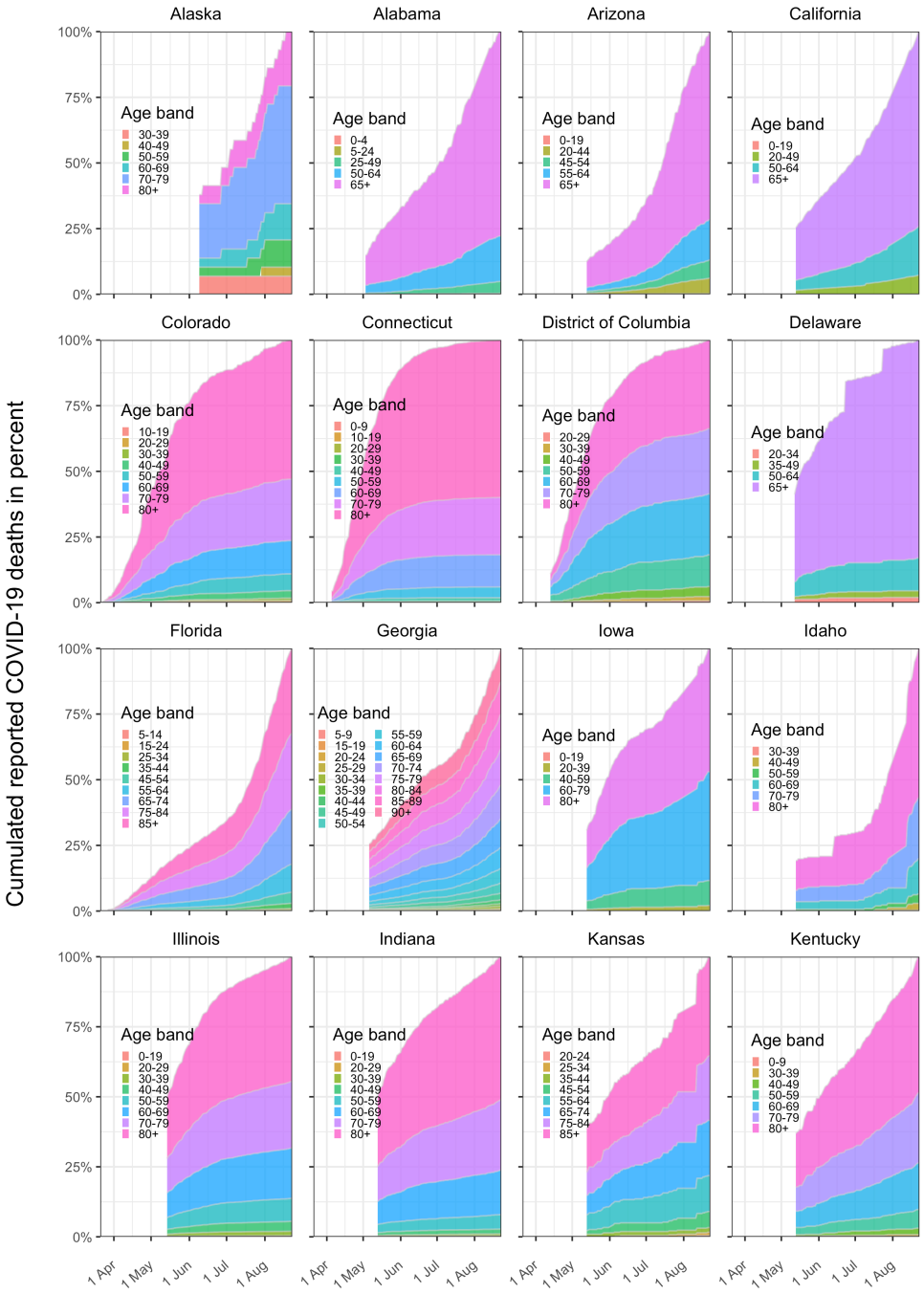

Figure S16: **Age-specific COVID-19 mortality data in the United States (part 1).** COVID-19 related deaths were recorded as reported by city or state DoH. Shown is the percent contribution of age groups to cumulated deaths (colours) from the first day on which the death by age was recorded.. The start of the x-axis is the same in every figures and corresponds to the day with the first observation of death by age across all locations (states and metropolitan areas).

DOI: https://doi.org/10.25561/82551

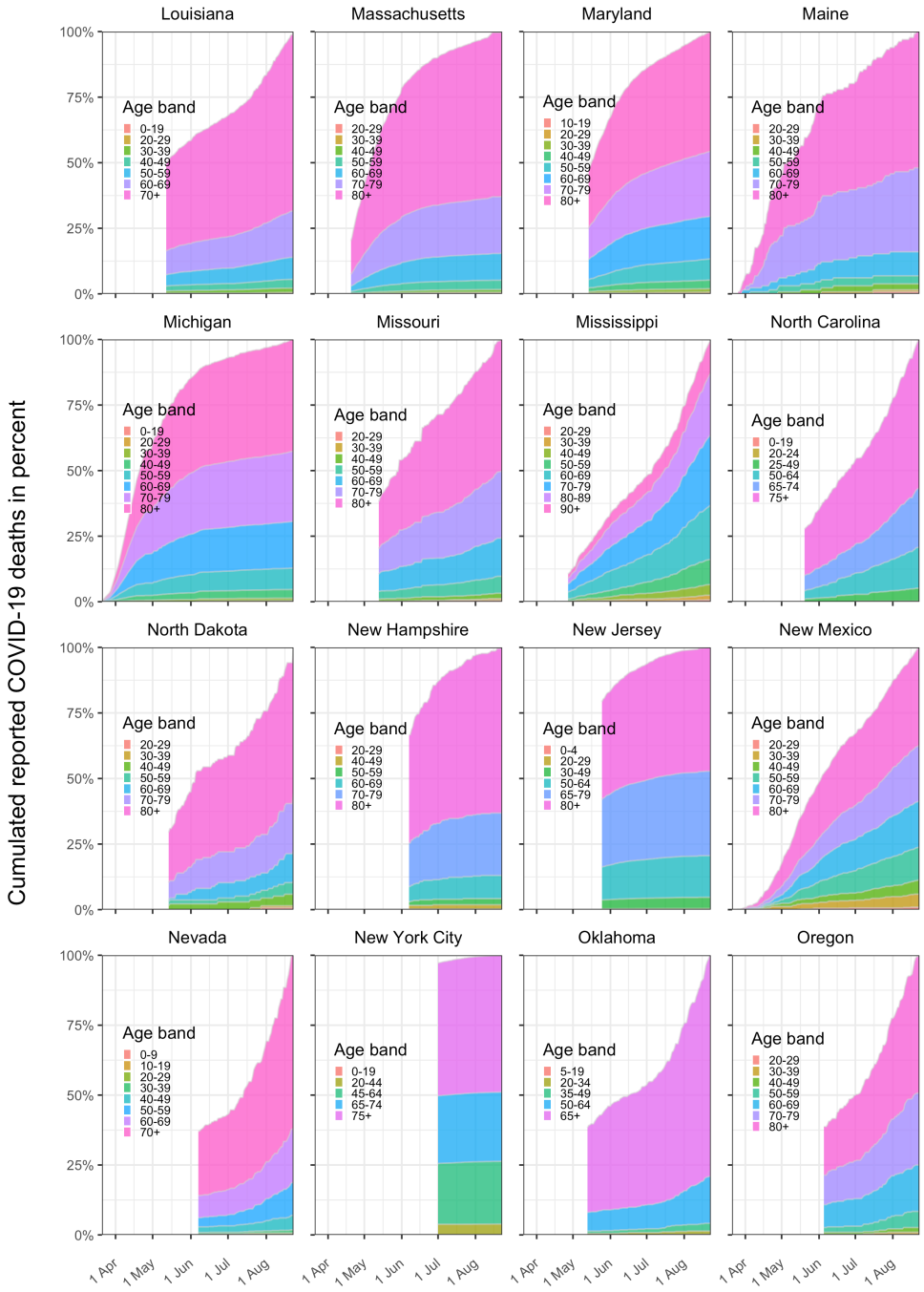

Figure S16: **Age-specific COVID-19 mortality data in the United States (part 2).** COVID-19 related deaths were recorded as reported by city or state DoH. Shown is the percent contribution of age groups to cumulated deaths (colours) from the first day on which the death by age was recorded.. The start of the x-axis is the same in every figures and corresponds to the day with the first observation of death by age across all locations (states and metropolitan areas).

DOI: https://doi.org/10.25561/82551

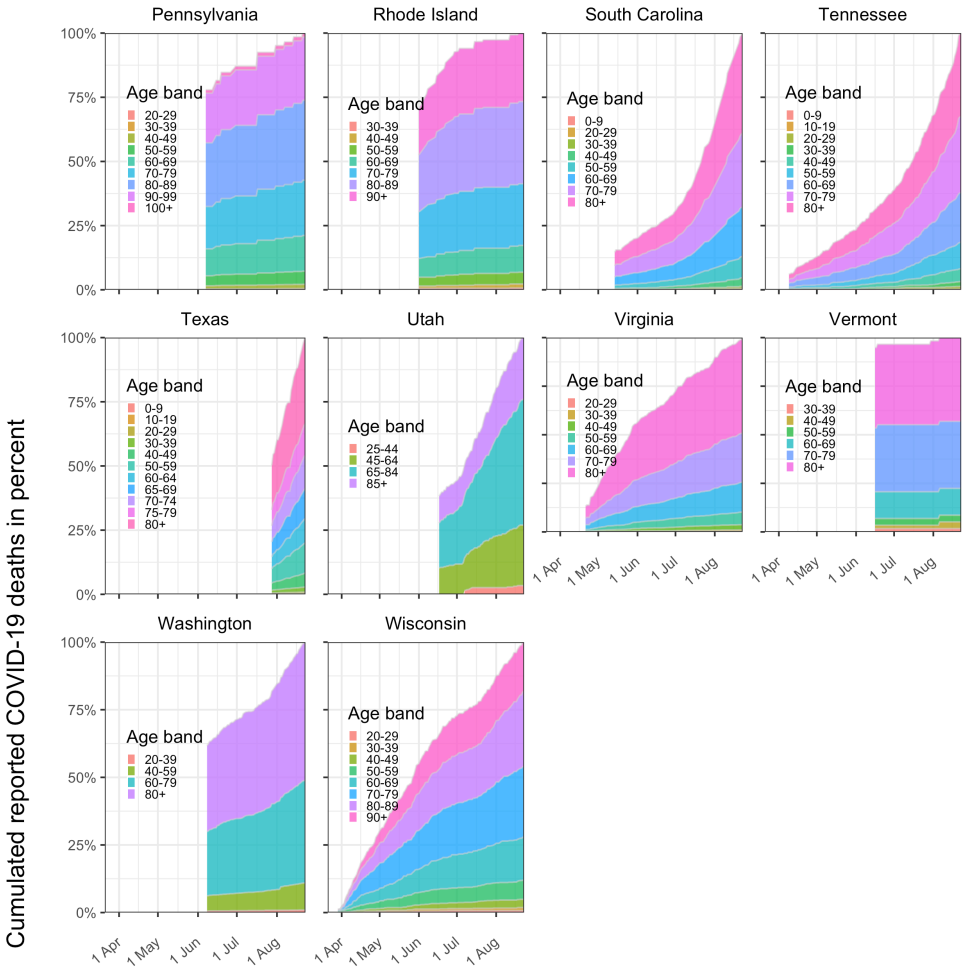

Figure S16: **Age-specific COVID-19 mortality data in the United States (part 3).** COVID-19 related deaths were recorded as reported by city or state DoH. Shown is the percent contribution of age groups to cumulated deaths (colours) from the first day on which the death by age was recorded. The start of the x-axis is the same in every figures and corresponds to the day with the first observation of death by age across all locations (states and metropolitan areas).

DOI: https://doi.org/10.25561/82551

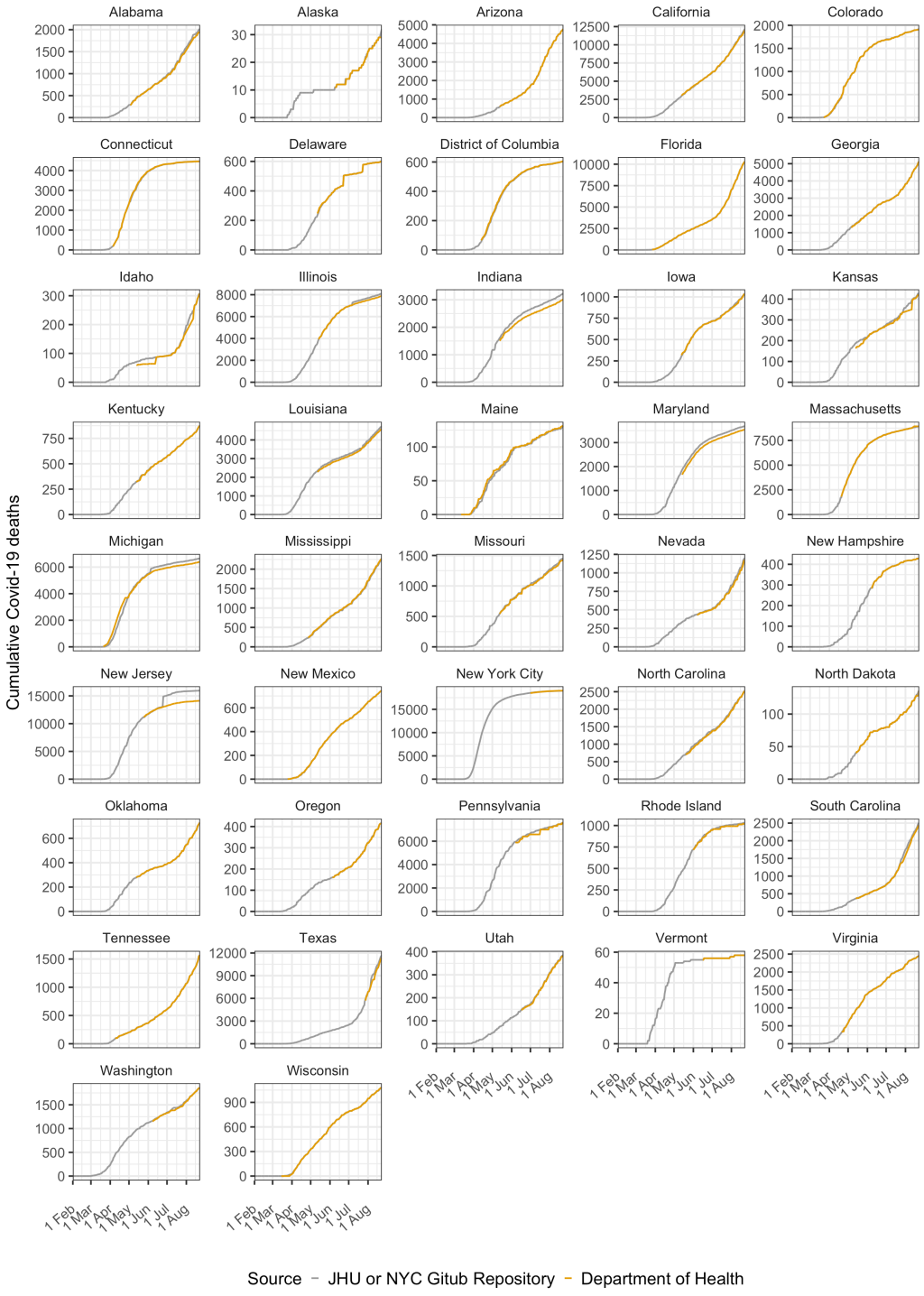

Figure S17: **Comparison of the Covid-19 overall death between the Department of Health death by age data with the overall death from JHU [3], and the New York City Github repository (for NYC) [5].**

S3 Supplementary Text: Bayesian semi-mechanistic SARS-CoV-2 infection model

Figure S2, also reproduced here as Figure S18, summarises the main components of the age-specific contact and infection model. Section S3.1 describes the infection component of the model, and Section S3.2 describes the contact component of the model. Section S3.3 describes how the model is fitted against age-specific mortality data. Section S3.4 specifies input parameters and prior distributions. Table S9 gives an overview of the model parameters and associated prior distributions. Section S3.6 describes the generated quantities of the contact and infection model. Finally, Section S3.5 provides details on computational inference.

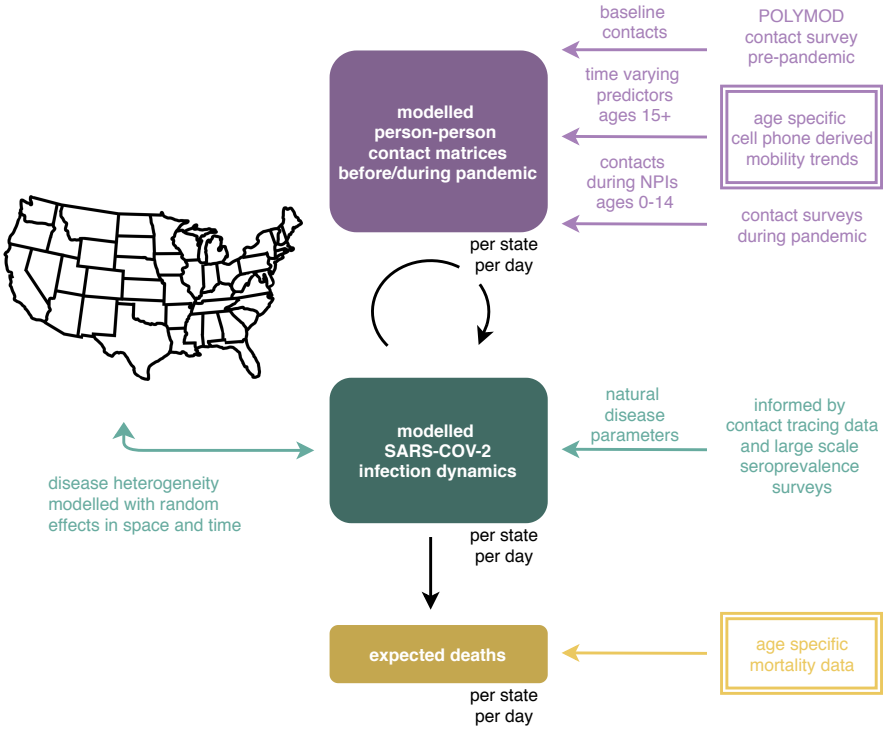

Figure S18: **Overview of the age-specific contact and infection model.**

DOI: https://doi.org/10.25561/82551

Name	Estimated	Prior	Notes	Section reference
Initial number of infections	yes	$\log c_{m,t,[20-54]} \sim \mathcal{N}(4.5, 0.62^2)$, $c_{m,t,a} = 0,$ for $a \notin [20-54]$, where $t = 1, \ldots, 6$.	infections seeded among individuals aged 20-54 with log-normal prior with mean XX	Section S3.4.1
Infection parameters	yes	$R_{0,m} \sim \mathcal{N}(3.28, \kappa)$ $\kappa \sim \mathcal{N}_{[0,\infty)}(0, 0.5)$	Based on [50]	Section S3.4.1
Susceptibility to infection	yes	$\log \rho^S_{[0-14]} \sim \mathcal{N}(-1.07, 0.22^2)$ $\log \rho^S_{[65+]} \sim \mathcal{N}(0.38, 0.16^2)$	Susceptibility was modelled relative to individuals aged 15-64, with lower susceptibility to infection among individuals aged 0-14, and higher susceptibility among individuals aged 65+. Based on [51]	Section S3.4.1
Discretized generation time distribution	no	-	Based on [52]	Section S3.4.1
Baseline age-specific contact matrix before mobility decreased	no	-	Predicted based on locations' age composition and population density for weekdays and weekends	Section S3.4.2
Mobility trend predictors	no	-	Decomposed into 3 components to allow for varying effect sizes	Section S3.4.2
Regression coefficients to describe time-varying contact intensities before the rebound date.	yes	$\beta_m^{\text{eased}} \sim \mathcal{N}(\beta^{\text{eased}}, \sigma^2_{\text{eased}})$ $\beta^{\text{eased}} \sim \mathcal{N}(0, 1)$ $\sigma_{\text{eased}} \sim \text{Exp}(10)$	Location-specific random effects to quantify the effect of rapid decreases in mobility between the dip date and the rebound date. Effects are assumed to be constant across age groups.	Section S3.4.2
Regression coefficients to describe time-varying contact intensities after the rebound date.	yes	$\beta_{mt}^{\text{upswing}} = \beta_m^{\text{upswing}} \times \beta_t^{\text{upswing}}$ $\beta_m^{\text{upswing}} \sim \mathcal{N}(\beta^{\text{upswing}}, \sigma^2_{\text{upswing}})$ $\beta^{\text{upswing}} \sim \mathcal{N}(0, 1)$ $\sigma_{\text{upswing}} \sim \text{Exp}(10)$ $\beta_t^{\text{upswing}} = \varepsilon_{\lfloor c(t)/2 \rfloor}$ $\varepsilon_1 \sim \mathcal{N}_{[0,\infty)}(0, 0.025)$ $\varepsilon_v \sim \mathcal{N}_{[0,\infty)}(\varepsilon_{v-1}, \sigma_\varepsilon)$ for $v > 1$ $\sigma_\varepsilon \sim \text{Exp}(10)$	Location-specific and time-varying random effects to quantify the effect of increasing mobility levels over the longer period after the rebound date. Effects are assumed to be constant across age groups. Time-varying effects are modelled with a bi-weekly AR(1) process that is the same across locations and age groups.	Section S3.4.2
Location and age-specific infection fatality ratios	yes	$\pi_{m,a} = \pi_a \times \delta_{m,a}$ $\log \pi_a \sim \mathcal{N}(\mu_a, \sigma_a^2)$ $\log \delta_{m,[20-49]} \sim N(0, \sigma^2_{[20-49]})$ $\log \delta_{m,[50-69]} \sim N(0, \sigma^2_{[50-69]})$ $\log \delta_{m,[70+]} \sim \text{Exp}(\lambda_{[70+]})$ $\sigma_{[20-49]}, \sigma_{[50-69]} \sim \text{Exp}(10)$ $\lambda_{[70+]} \sim \text{Exp}(0.05)$	The prior distribution on age-specific fatality ratios π_a is based on a re-analysis of data from several sero-prevalence studies, and similar to the relationship estimated in [53]. μ_a, σ_a are specified in Table S13. Location-specific random effects account for spatial heterogeneity.	Section S3.4.3
Infection-to-death distribution	no	-	As in [54]	Section S3.4.3
Overdispersion parameter	yes	$\phi \sim \mathcal{N}_{[0,\infty)}(0, 5)$	As in [54]	Section S3.4.3

Table S9: List of inputs and model parameters.

In the model, SARS-CoV-2 spreads via person-to-person contacts. Person-to-person contacts are described at the population level with the expected number of contacts made by one individual, referred to as contact intensities. Contact intensities are age-specific. Contact intensities vary across locations (states and metropolitan areas) according to each location' age composition and population density, and change over time. Data from contact surveys before the pandemic are used to define baseline contact intensities. Data from age-specific, cell phone derived mobility trends are used to estimate changes in contact intensities during the epidemic in each location, among individuals aged $15+$. Contact intensities involving individuals aged 0-14 are defined based on contact surveys conducted during the pandemic. Infection dynamics in each location are modelled through age-specific, discrete-time renewal equations over time-varying contact intensities. Natural disease parameters such as age-specific susceptibility to infection, the generation time distribution, and symptom onset and onset to death distributions are informed by epidemiologic analyses of contact tracing data. Age-specific infection fatality ratio estimates are informed by large-scale sero-prevalance surveys. Disease heterogeneity is modelled with random effects in space and time on contact intensities and disease parameters. The model returns the expected number of COVID-19 deaths over time in each location, which is fitted against age-specific, COVID-19 mortality data. New data sources presented in this study are indicated in double-framed boxes.

S3.1 Infection model

The time evolution of SARS-CoV-2 infections is quantified in terms of a discrete-time age-specific renewal model. The discrete renewal model arises as the expected value of an age dependent branching process. The model extends a previous version to age-specific disease dynamics [54]. In the renewal equations, we model populations stratified by the 5-year age bands $\mathcal{A}$, such that

$$a \in \mathcal{A} = \Big\{[0-4], [5-9], \ldots, [75-79], [80-84], [85+]\Big\}, \tag{S10}$$

resulting in $A = 18$ population strata. We denote the number of new infections, c, on day t, in age band a, and location m as $c_{m,t,a}$, with $c_{m,t,a} \geq 0$ for all t, m, a. Here infections are taken to be both symptomatic and asymptomatic. We introduce a series of daily contact intensity matrices $\mathbf{C}_{mt}$ of dimension 18×18 in each location m. The time changing contact intensities $\mathbf{C}_{m,t}$ were modelled in a regression framework that uses as input pre-pandemic contact intensities, which will be presented in Section S3.4.2, as well as the age-specific mobility trends $X_{m,t,a}$ that are described in Supplementary Text S1. Entry $\mathbf{C}_{m,t,a,a'}$ quantifies the expected number of contacts that one person in age group a has with persons of another age a' on day t in location m, which we refer to as contact intensity. We further consider the probability $\rho_{a'}$ that a contact with an infectious person leads to infection of one person in a'. We interpret $\rho_{a'}$ as a natural disease parameter that is region and time independent. We

model $\rho_{a'}$ as the product of a constant baseline parameter ρ_0, and relative susceptibility parameters $\rho^S_{a'}$ for $a' \in \mathcal{A}$ through

$$\rho_{a'} = \rho_0 \times \rho^S_{a'} = \exp(\log \rho_0 + \log \rho^S_{a'}). \tag{S11}$$

To ensure a relative interpretation of the susceptibility parameters, we set $\rho^S_{a'} = 1$ for some age bands. Details are given in Supplement S3.4.1. This allows us to describe the time-varying reproduction number on day t from one infectious person in a in location m with

$$R_{m,t,a} = \sum_{a'} s_{m,t,a'}\ \rho_{a'}\ \mathbf{C}_{m,t,a,a'}, \tag{S12}$$

where $s_{m,t,a'}$ is the proportion of the population in location m and in age band a' that remains susceptible to SARS-CoV-2 infection. It is given by

$$s_{m,t,a'} = 1 - \frac{\sum_{s=1}^{t-1} c_{m,t,a'}}{N_{m,a'}}, \tag{S13}$$

where $N_{m,a'}$ denotes the population count in age group a' and location m. Extending the basic renewal model, we obtain similarly

$$c_{m,t,a'} \quad = \quad s_{m,t,a'} \rho_{a'} \sum_{a} \mathbf{C}_{m,t,a,a'} \left(\sum_{s=1}^{t-1} c_{m,s,a}\ g(t-s) \right) \tag{S14}$$

where g is the discretized generation time distribution as in [54]. This is because an individual of age a' in country m at time t makes contacts with individuals of age a at rate $\mathbf{C}_{m,t,a,a'}$, and these are successful with probability $\rho_{a'}$ if and only if 1) the individual in a' is susceptible, which is the case with probability $s_{m,t,a'}$, and 2) the individual in a is still infectious, which is the case with probability $g(t-s)$.

S3.2 Time-varying contact patterns

S3.2.1 Overview.

Several studies have collected data on age-specific contact patterns in various settings across the United States prior to emergence of SARS-CoV-2 [55, 56, 57, 58]. However, little data are available on how contact patterns changed during the pandemic. These considerations prompted us to take a predictive approach. First, we used data from the Polymod study [59] to predict baseline contact matrices during the early part of the pandemic for each location, which we denote by $\mathbf{C}_m$. The pre-pandemic contact matrices quantify the expected number of contacts from one person in age band a with individuals in age band a' per day in location m, also known as contact intensities. Populations were stratified by 5-year age bands $a \in \mathcal{A}$ defined in (S10). Reflecting differences in contact patterns during weekdays and on weekends, distinct pre-pandemic contact matrices were generated

for weekdays and weekends, $\mathbf{C}_m^{\text{wday}}$ and $\mathbf{C}_m^{\text{wend}}$. For simplicity we suppress the weekday and weekend notation in what follows, with all equations being analogous. Details are presented in Section S3.2.2.

Second, we used the age-specific mobility trend data available for individuals aged $18+$ to predict time-varying contact intensities among individuals aged $15+$. Overall, time changing contact intensities on day t in location m were modelled through

$$\mathbf{C}_{m,t,a,a'} = \eta_{m,t,a}\, \mathbf{C}_{m,a,a'}\, \eta_{m,t,a'}, \tag{S15}$$

where $a \in \{[15-19], [20-25], \ldots, [85+]\}$ and $a' \in \{[15-19], [20-25], \ldots, [85+]\}$. The multipliers $\eta_{m,t,a}$ describe the estimated effect of the age-specific mobility trends $X_{m,t,a}$ on changes in pre-pandemic contact matrices for each location. Since both the index person and the contacted individuals are changing their mobility over time, the multipliers are applied to the rows and columns of the contact intensity matrix. Details are presented in Section S3.2.3.

Third, we used data from two contact surveys conducted after school/nursery closures to specify contact intensities from and to children aged 0-14. Details are presented in Section S3.2.4.

S3.2.2 Baseline contact intensity matrices prior to changes in mobility

We first obtained estimates of weekday and weekend contact matrices for 8 European countries from the Polymod contact survey [60]. Briefly, survey participants were recruited in such a way as to be broadly representative of the whole population in terms of geographical spread, age, and sex. Participants were asked to keep a diary of their contacts. The study included 7,290 participants recruited between May 12, 2005 and September 05, 2006. Contact intensities were estimated for Belgium, Germany, Finland, Italy, Luxembourg, the Netherlands, Poland, and the United Kingdom using the approach of [61], using code at the Github repository [62]. We index each of the European countries with e. The posterior median estimates of the number of individuals in age $\tilde{a}'$ that were contacted per day by one individual in age $\tilde{a}$ were extracted. Using the available methodology, populations were stratified in 1-year age bands. Figure S19 illustrates the estimated weekend and weekday contact intensity matrices for the 8 European countries.

To match the population stratification in the SARS-CoV-2 infection model, the estimated contact intensities at 1-year resolution were aggregated to 5-year resolution using

$$\mathbf{C}_{e,a,a'} = \sum_{\tilde{a}\in a, \tilde{a}'\in a'} \frac{N_{e,\tilde{a}}}{\left(\sum_{\tilde{a}\in a} N_{e,\tilde{a}}\right)} \mathbf{C}_{e,\tilde{a},\tilde{a}'}, \tag{S16}$$

where $N_{e,\tilde{a}}$ denotes the number of individuals in 1-year age band $\tilde{a}$ in the corresponding European country e. The

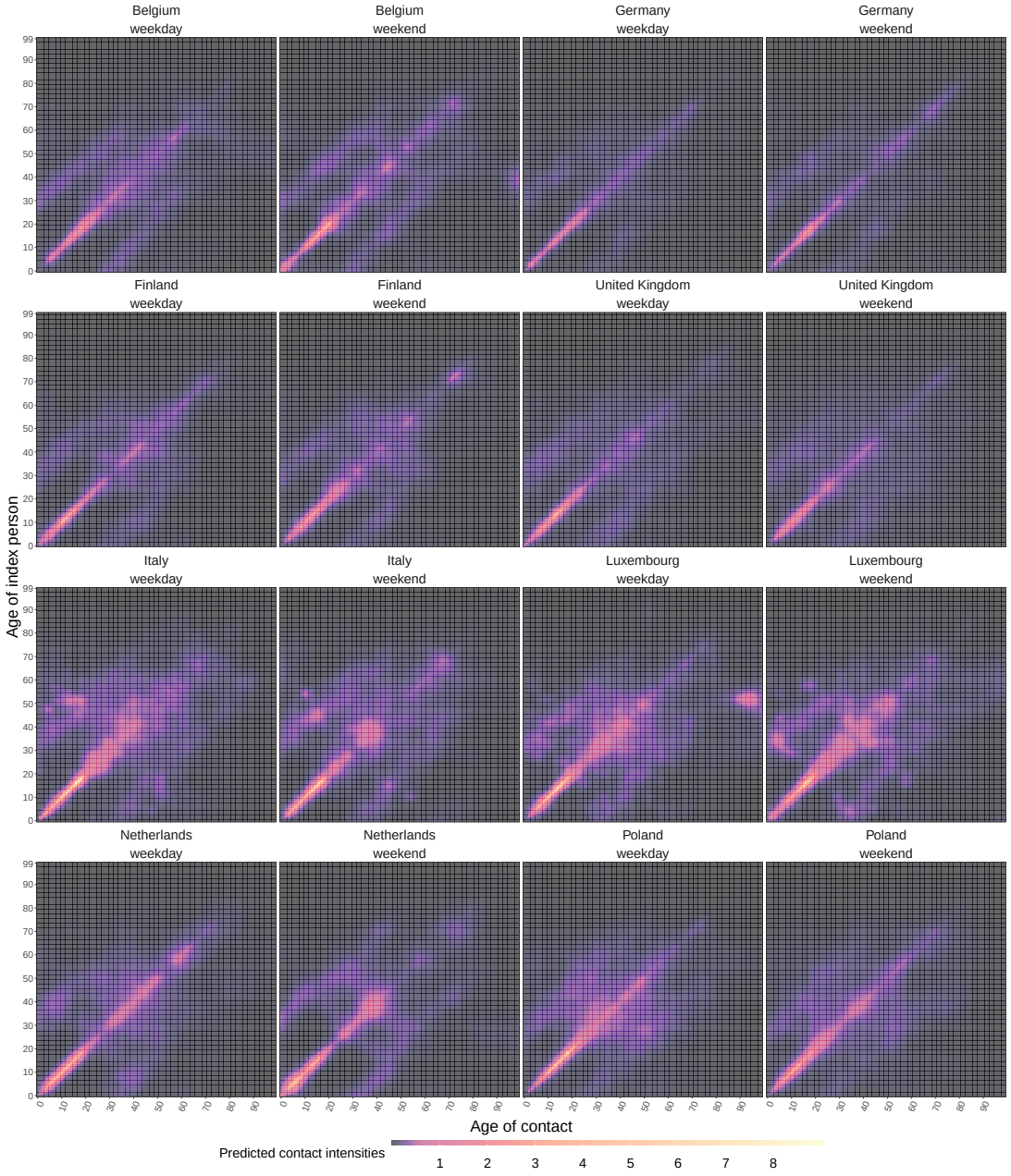

Figure S19: **Estimated contact intensities for the 8 Polymod countries by weekday and weekend.**

estimated contact intensities $\mathbf{C}_{e,a,a'}$ were real-valued and positive.

Next, we constructed a predictive statistical model of contact intensities based on population demographics including the total population size, the number of individuals in age band a', the proportion of individuals in age band a', and population density. Regression models were fitted based on the $8 * 18 * 18 = 2,592$ estimates (S16) from the European-wide Polymod survey, separately for weekdays and weekends. The chosen statistical model was of the form

$$\log \mathbf{C}_{e,a,a'} \sim \mathcal{N}(\mu_{e,a,a'}, \sigma^2) \tag{S17a}$$

$$\mu_{e,a,a'} = \theta_{a,a'} + \theta_1 \frac{N_{e,a'}}{N_e} + \theta_2 \log \frac{N_{e,a'}}{A_e}, \tag{S17b}$$

where $\theta_{a,a'}$ are pairwise age-specific baseline terms, $N_{e,a'}$ is the number of individuals in age band a' in location e, and A_e is the land area of location e in square kilometres. The least squares estimates of θ_1 and θ_2 were positive and highly significant for both weekday and weekend contact intensities, so that under model (S17) contact intensities with individuals of age a' increase as the proportion of the population of age a' increases, and as population density increases. The fits of model (S17) through the training data are illustrated in Figure S20. The leave-one-out cross-validation mean absolute error associated with model (S17) was 0.361 and 84.1% of the variance was explained.

Baseline contact matrices for the 50 U.S states, the District of Columbia and New York City were then predicted using (S17). Figure S21 shows the predicted baseline weekday contact matrices $\mathbf{C}_m$ for all locations. The predicted contact matrices are consistent with key characteristics of human contact patterns, including high number of contacts between children and teenagers of same age, parent-child interactions, broader workforce interactions, and child/parent-grandparent interactions. Figure S22 illustrates location-specific differences in predicted contact intensities relative to the national average. In locations with young populations such as Alaska, the District of Columbia, Texas or Utah, lower contact intensities are predicted with individuals in young age groups when compared to the national average. Similarly, in locations with older populations such as Maine, higher contact intensities are predicted with individuals in older age groups when compared to the national average. Figure S23 illustrates that locations with high population density such as the District of Columbia and New York City are predicted to have higher contact intensities compared to the national average. Figure S24 compares predicted contact intensities on weekdays to those predicted for weekends. Predicted contact intensities were higher between children and the elderly individuals on weekends compared to weekdays for all locations.

Figure S20: **Predicted contact intensities versus Polymod estimates.** Median predictions and 95% predictive intervals under model (S17) are shown in grey, and Polymod estimates are shown in blue.

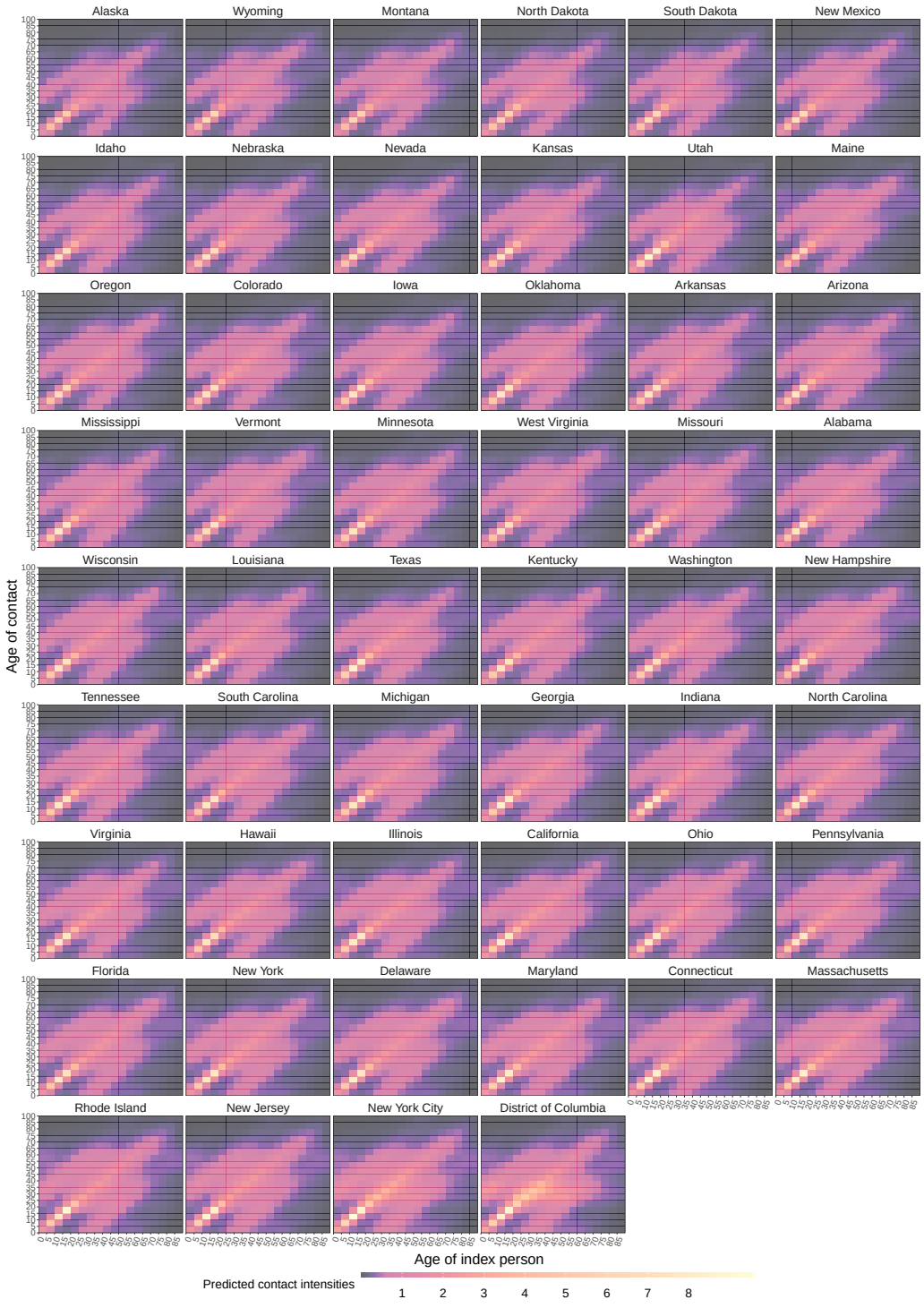

Figure S21: **Predicted age-specific contact matrices for the 50 US states, District of Columbia and New York City prior to the pandemic, on weekdays.** Shown in colour are the predicted number of contacts made by one index person of age a with individuals of age a' per day. Locations ordered by population density.

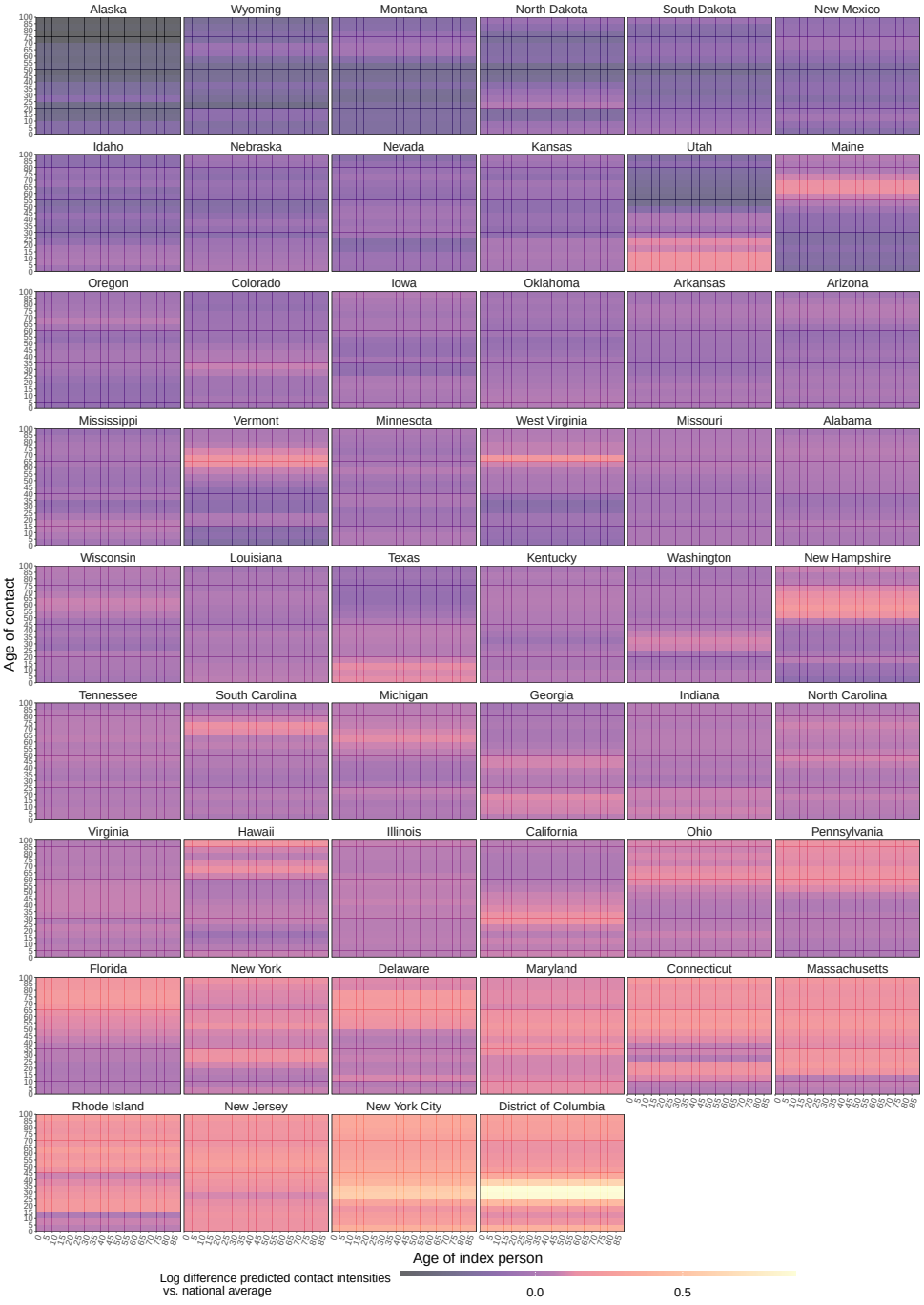

Figure S22: **Difference in predicted age-specific contact matrices for the 50 US states, District of Columbia and New York City prior to the pandemic relative to the national average, on weekdays.** Shown in colour are the log ratio of the contact intensities in each location compared to the contact intensities for the national population. Locations ordered by population density.

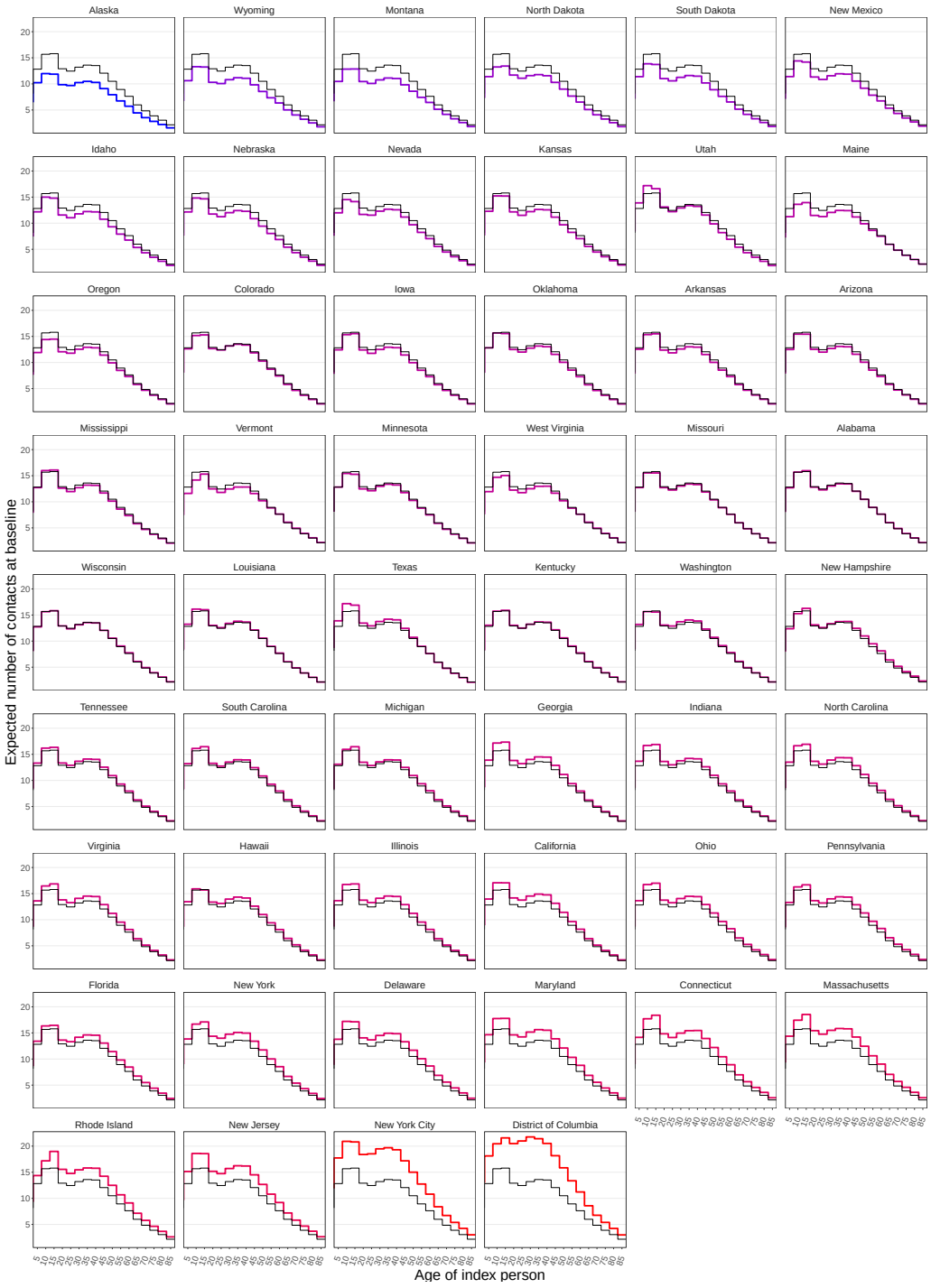

Figure S23: **Predicted number of expected contacts by one index individual of age a per day.** Locations ordered by population density, national average shown in black. Predictions shown for weekdays.

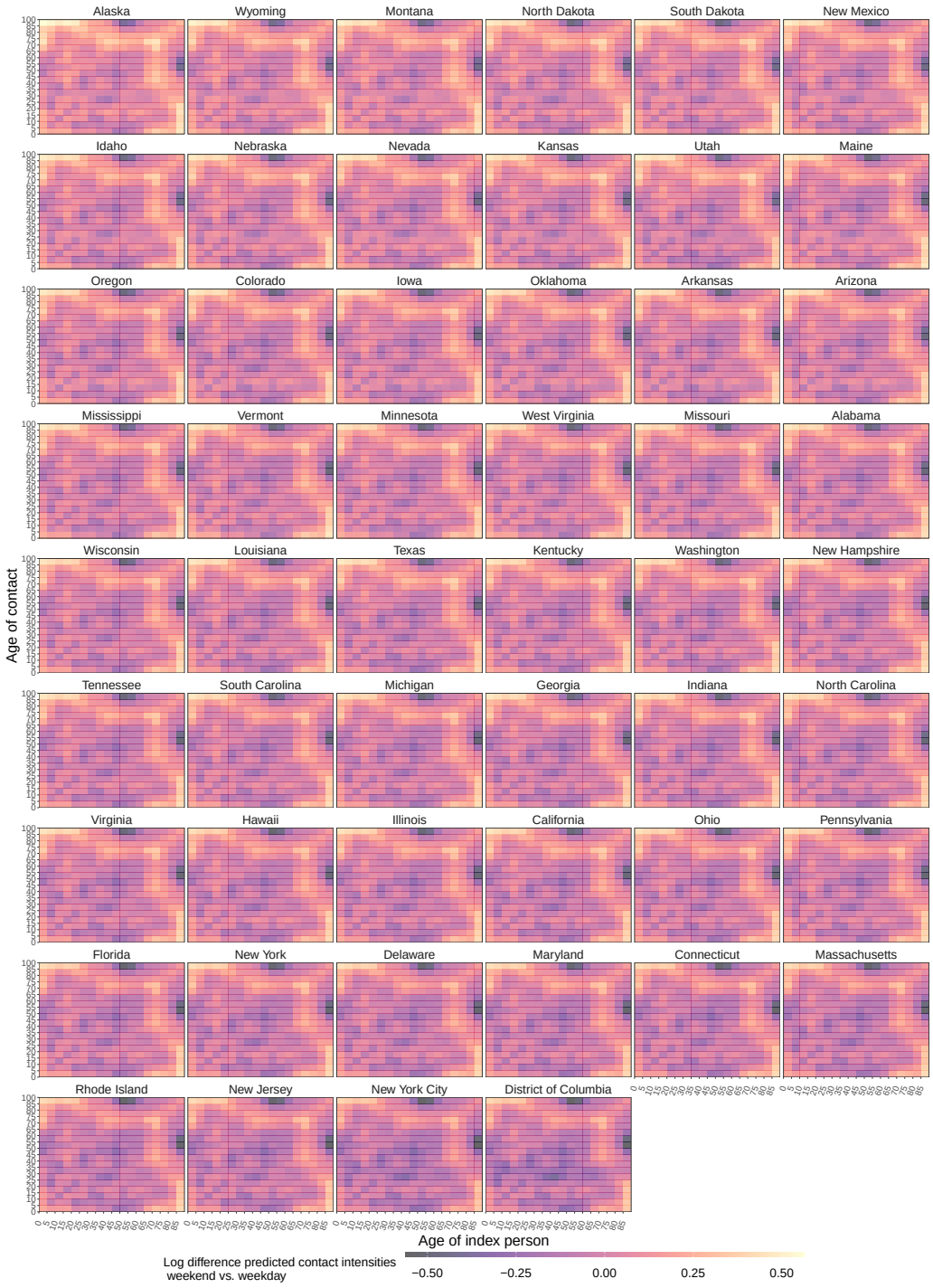

Figure S24: **Difference in contact intensities at weekends compared to weekdays.** Locations ordered by population density.

S3.2.3 Time-varying contact intensities among individuals aged $15+$

The time changing multipliers $\eta_{m,t,a}$ to the rows and columns of the pre-pandemic contact matrices were obtained through a regression model using the age-specific mobility trends S3 as predictors. To age stratification (S10) used in the model, we expanded the original mobility trends through

$$X_{m,t,a} = \begin{cases} X_{m,t,\tilde{a}} & \text{if } a \in \tilde{a} \\ X_{m,t,[18-24]} & \text{if } a \in \{[15-19],[20-24]\}. \end{cases} \tag{S18}$$

This step assumed that the mobility trends among individuals aged 15-18 are represented by the observed mobility trends among individuals aged $18-24$.

To model different effects around the time of stay at home orders and later time periods, the mobility trends S18 were decomposed into three components. The three components are a baseline mobility trend denoted by $X^{\text{base}}_{m,t,a}$, an eased mobility trend which we denote by $X^{\text{eased}}_{m,t,a}$, and an upswing multiplier that we denote by $X^{\text{upswing}}_{m,t,a}$. The decomposition satisfies the relation

$$X_{m,t,a} = X^{\text{base}}_{m,t,a} \times X^{\text{eased}}_{m,t,a} \times X^{\text{upswing}}_{m,t,a} \tag{S19}$$

for all m, t, and $a \in \{[15-19],[20-24],\ldots,[85+]\}$. Specifically, the base mobility trends, the eased mobility trends and multipliers were defined as

$$X^{\text{base}}_{m,t,a} = \begin{cases} X_{m,t,a} & \text{if } t < t^{\text{dip}}_m, \\ 1 & \text{if } t \geq t^{\text{dip}}_m, \end{cases} \tag{S20a}$$

$$X^{\text{eased}}_{m,t,a} = \begin{cases} 1 & \text{if } t < t^{\text{dip}}_m, \\ X_{m,t,a} & \text{if } t^{\text{dip}}_m \leq t < t^{\text{rebound}}_m, \\ \chi^{\text{wday}}_{m,a} & \text{if } t \geq t^{\text{rebound}}_m \text{ and } t \text{ is a weekday}, \\ \chi^{\text{wend}}_{m,a} & \text{if } t \geq t^{\text{rebound}}_m \text{ and } t \text{ is a weekend}, \end{cases} \tag{S20b}$$

$$X^{\text{upswing}}_{m,t,a} = \begin{cases} 1 & \text{if } t < t^{\text{dip}}_m, \\ 1 & \text{if } t^{\text{dip}}_m \leq t < t^{\text{rebound}}_m, \\ X_{m,t,a}/\chi^{\text{wday}}_{m,a} & \text{if } t \geq t^{\text{rebound}}_m \text{ and } t \text{ is a weekday}, \\ X_{m,t,a}/\chi^{\text{wend}}_{m,a} & \text{if } t \geq t^{\text{rebound}}_m \text{ and } t \text{ is a weekend}, \end{cases} \tag{S20c}$$

where $\chi^{\text{wday}}_{m,a}$ is the average of the mobility trend $X_{m,t,a}$ over the 5 weekdays before t^{rebound}_m, and $\chi^{\text{wend}}_{m,a}$ is the average of the mobility trend $X_{m,t,a}$ over the 4 weekend days before t^{rebound}_m. Figure S25 illustrates the decomposed mobility trends for four locations.

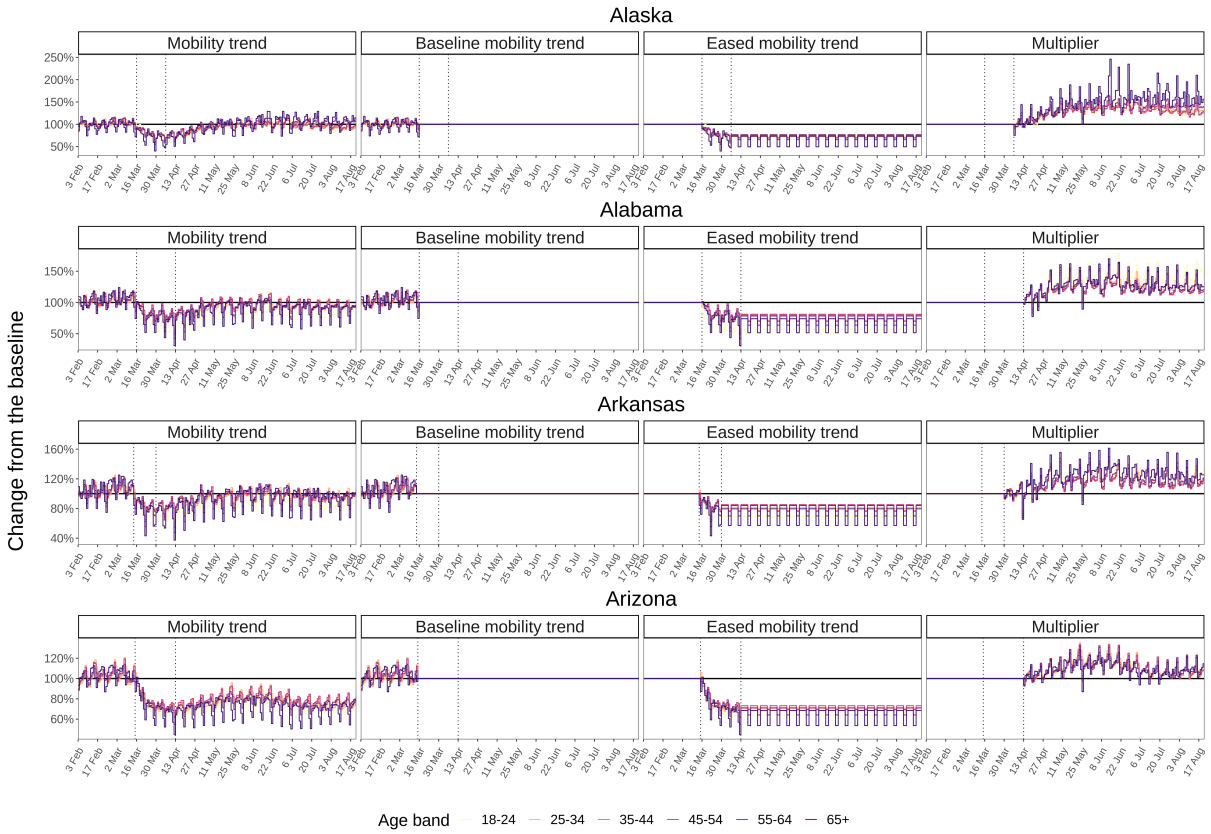

Figure S25: **Decomposition of mobility trends, shown for 4 US locations.** For each location, the change point in overall mobility trends was determined using a 10-day moving average. Age-specific mobility trends were then decomposed into eased mobility trends and multipliers as shown. The vertical dash lines indicate the change points when mobility dipped and began to rebound.

With the decomposed mobility trends, we modelled the multipliers in (S15) that quantify the time evolution in contact intensities through

$$\eta_{m,t,a} = \exp\Big(\log X^{\text{base}}_{m,t,a} + \beta^{\text{eased}}_{m} \log X^{\text{eased}}_{m,t,a} + \beta^{\text{upswing}}_{mt} \log X^{\text{upswing}}_{m,t,a}\Big) \tag{S21}$$

where β^{eased}_{m} is varying across locations, and $\beta^{\text{upswing}}_{mt}$ is varying in space and time. The purpose of the eased mobility regression coefficient β^{eased} was to capture the effect of permanent reductions in contact patterns in the early phase of the pandemic. The purpose of the upswing regression coefficients $\beta^{\text{upswing}}_{mt}$ was to capture longer-term effects after the initial reduction in contact patterns during the early phase of the pandemic. The

longer-term effects were allowed to differ in time and across the United States. Within each location, the effect of the age-specific mobility trends was assumed to be identical.

To illustrate the effect of the regression coefficients, consider the case that $\beta_m^{\text{eased}} = \beta_{mt}^{\text{upswing}} = 0$. In this case, $\eta_{m,t,a} = 1$ and the contact intensities on day t are the same as at baseline after the dip date. If instead $\beta_m^{\text{eased}} = \beta_{mt}^{\text{upswing}} = 1$, the contact intensities on day t from index persons scale with the observed mobility trend $X_{m,t,a}$. Finally, if $\beta_m^{\text{eased}} = 1$ and $\beta_{mt}^{\text{upswing}} = 0$, the contact intensities on day t from index persons scale with the derived eased mobility trend $X_{m,t,a}^{\text{eased}}$ after the dip date.

S3.2.4 Time-varying contact intensities from and to children aged 0-14

To avoid extrapolating the mobility trends to children aged 0-14, we used data from two contact surveys conducted after school/nursery closures in response to accelerating COVID-19 epidemics in the UK and China [63, 51]. Figure S27 compares the estimated contact intensities from one child aged 0-14 using the contact surveys in Wuhan and Shanghai before and during lockdown. Figure S26 compares the estimated contact intensities to individuals aged 0-14. We plot the point estimates from the original report before lockdown to those during lockdown [51] (top row) and the ratio of the contact intensities during lockdown versus the corresponding contact intensities before lockdown (bottom row). During lockdown, the estimated, average number of daily peer-to-peer contacts from one child aged 0-14 to children in the same age group was 0.03, corresponding to a contact intensity ratio of 0.02 across both cities. The total number of contacts from one child aged 0-14 during the outbreak was 2.07, corresponding to a contact intensity ratio of 0.14 across both cities. The average number of contacts from one individual randomly chosen in the population to individuals in $0-14$ was 0.23 during lockdown, associated with a contact intensity ration of 0.29. The contact survey of Jarvis and colleagues [63] in the UK included individuals aged $18+$, but interviewed individuals were also asked to report contacts to children and teenagers aged 0-17. During lockdown, the estimated, average number of daily peer-to-peer contacts from one individual older than 18 to children aged 0-17 was 0.78, corresponding to a contact intensity ratio of 0.25.

In the United States, school closures have been ordered at least to one level (elementary school, middle / junior high school, or high school) in 13 states and the District of Columbia, and to all levels in the remaining 38 states [64]. In addition, 17 states have also ordered the closure of child-care centres, with the option to provide care only for children of parents working in essential areas, and 11 states either limited the number of children that can be cared for in child-care centres or encouraged families to stay at home with their children [65]. Figure S28 illustrates the timelines of school closure dates across the United States. In the model, we accounted for changes in contact patterns as a result of school and/or day care closures as follows. First, we obtained the average daily contact

intensities involving children aged 0-14 during lockdown in Wuhan and Shanghai, and denote these by

$$\mathbf{C}_{a,a'}^{COVID-0-14} \tag{S22}$$

where either $a \in \{[0-4],[5-9],[10-14]\}$ and a' is one of the 5-year age bands of the infection-and-contact model, or a is one of the 5-year age bands and $a' \in \{[0-4],[5-9],[10-14]\}$. Next, we denoted the time indices corresponding to school closures ordered or recommended in location m by $t_m^{\text{school-close}}$, and set the time-varying contact intensities that involve children aged 0-14 as

$$\mathbf{C}_{m,t,a,a'} = \begin{cases} \mathbf{C}_{m,a,a'} & \text{if } t < t_m^{\text{school-close}} \\ \mathbf{C}_{a,a'}^{COVID-0-14} & \text{if } t \geq t_m^{\text{school-close}} \end{cases} \tag{S23}$$

where $\mathbf{C}_{m,a,a'}$ is the baseline pre-COVID-19 contact matrix described in Section S3.2.2. School re-opening times fell in the forecast period, the subsequent changes on the contact intensities (S23) during this period are described in Section S3.7.

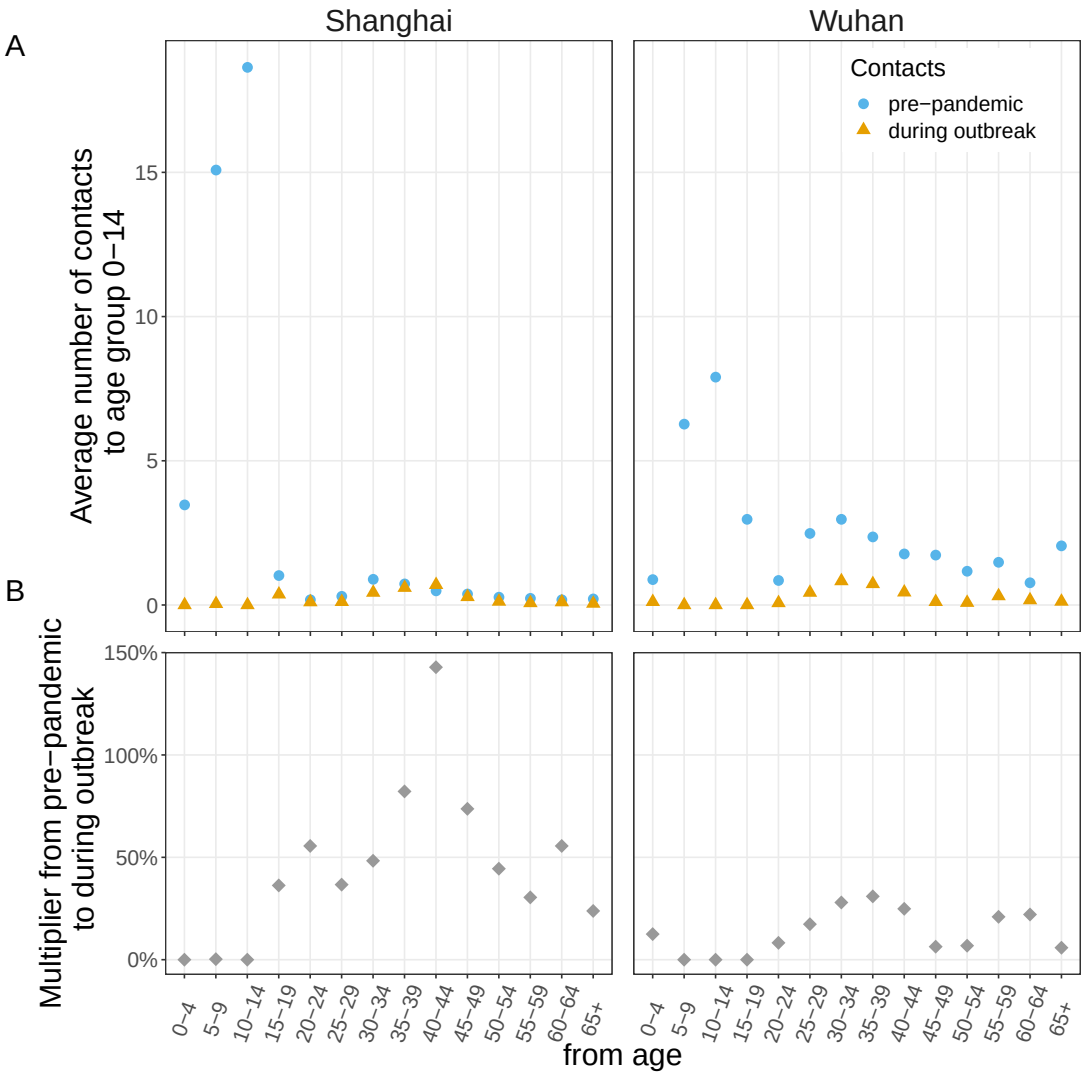

Figure S26: **Estimated changes in contact intensities to children aged 0-14 during lockdown, Shanghai and Wuhan, China.** Data from [51]. (**A**) Average number of contacts from one individual in 5-year age bands to children aged 0-14 before (blue) and during (orange) lockdown. (**B**) Contact intensity ratio (grey).

DOI: https://doi.org/10.25561/82551

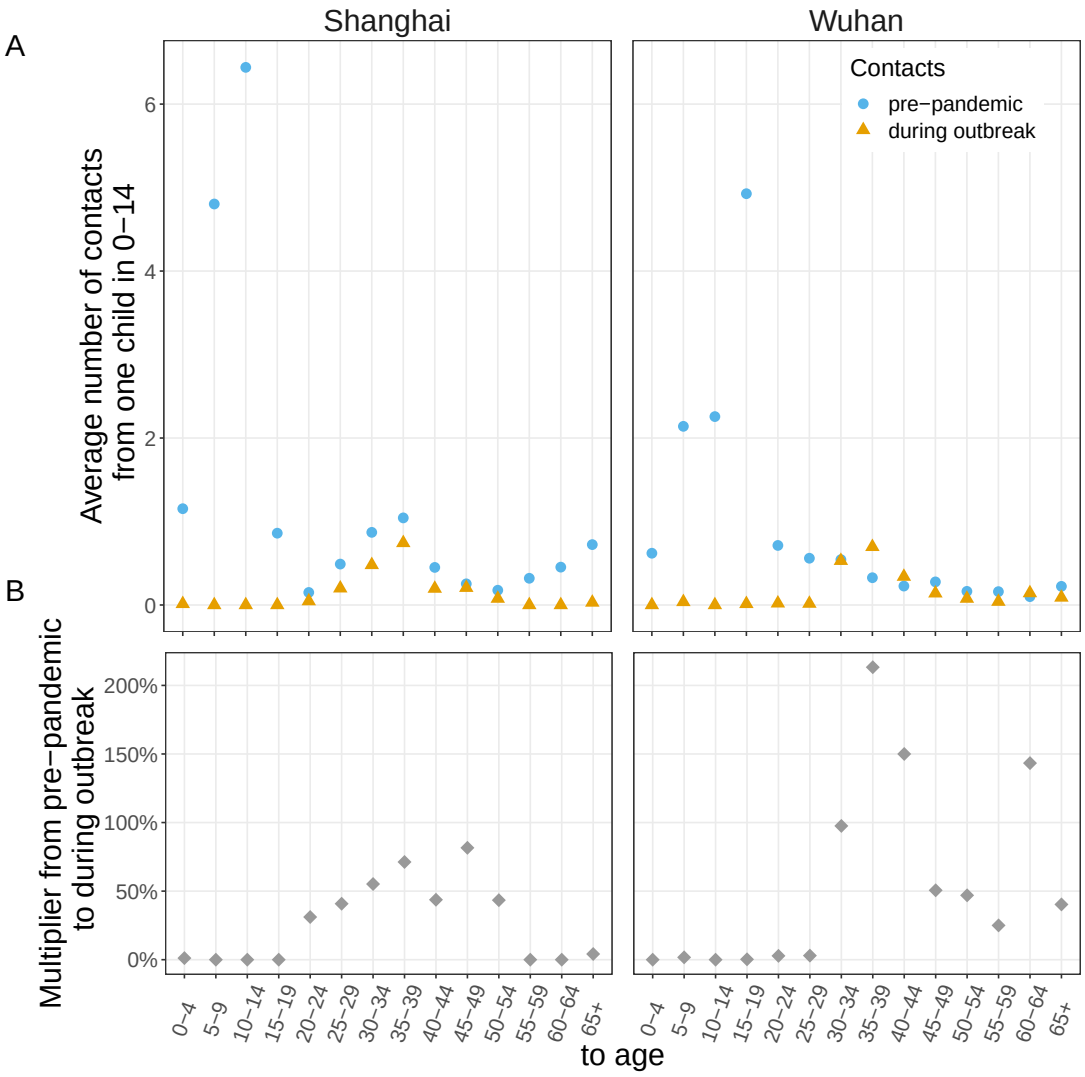

Figure S27: **Estimated changes in contact intensities from one child aged $0-14$ during lockdown, Shanghai and Wuhan, China.** Data from [51]. (**A**) Average number of contacts from one individual in $0-14$ to individuals in 5-year age bands before (blue) and during (orange) lockdown. (**B**) Contact intensity ratio (grey).

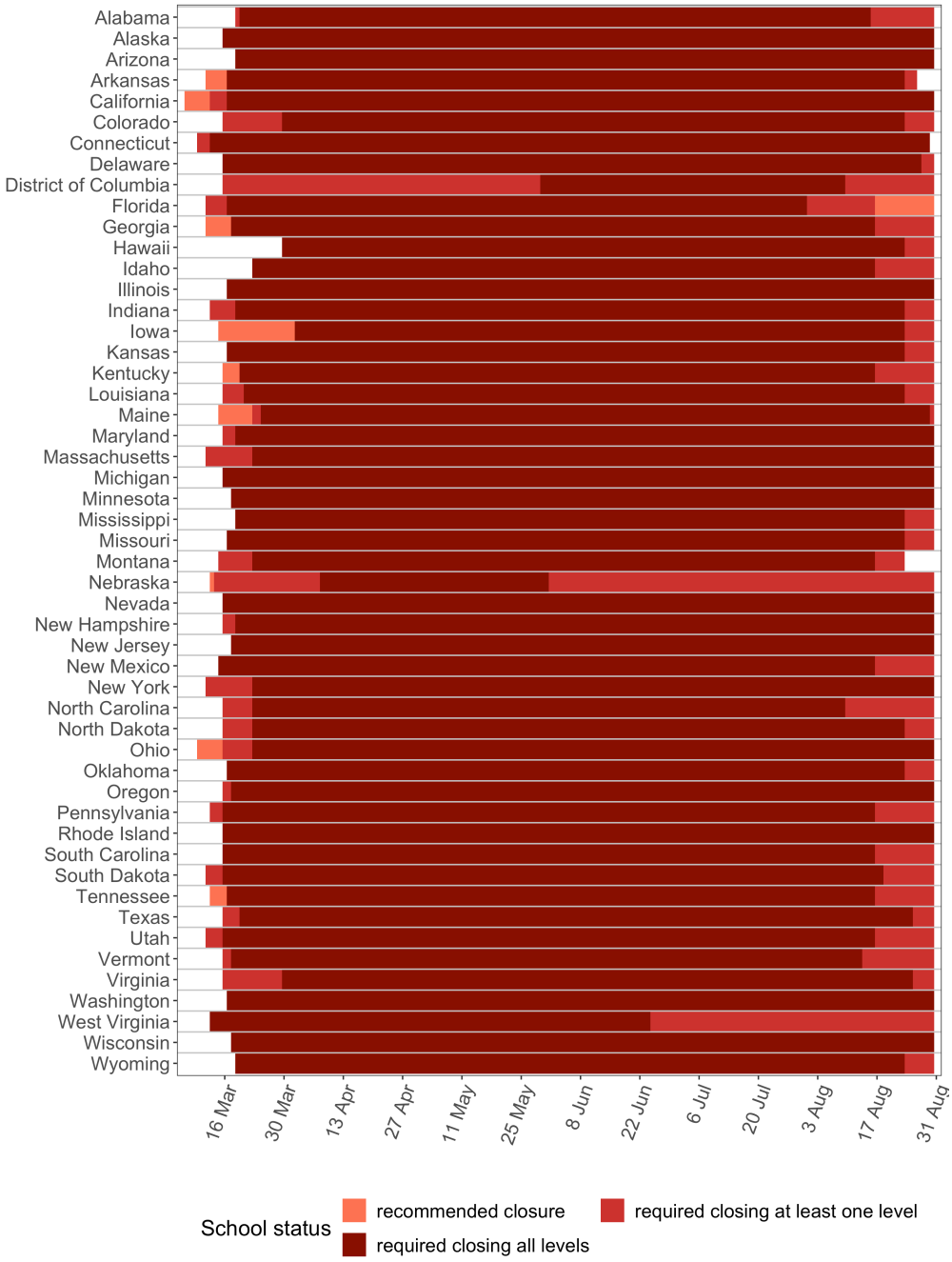

Figure S28: **School closure status in the 50 U.S states and the District of Columbia.** Data were retrieved from [64] for all U.S locations and were available until August 31, 2020.

S3.3 Likelihood

The self-renewal model is fitted to overall death counts and/or age-specific death counts for each location m. To establish a link between the data and the expected number of cases $c_{m,t,a}$ (S14), we model the probability $H_{ma}(t-s)$ that a person in age band a dies from SARS-CoV-2 infection before time $t-s$ after infection at time s in location (state or metropolitan area) m. We decompose the probability into the infection fatality ratio in location m and age band a, $\pi_{m,a}$, and the infection-to-death distribution h that describes when a death occurs conditional on non-survival. We decompose $H_{ma}(t-s)$ in this manner because estimates of both terms are available from the literature [66, 54]. Our model is

$$H_{ma}(t-s) = \pi_{ma} \int_0^{t-s} h(u)du, \tag{S24}$$

where $t-s$ is in continuous time and h integrates to 1. Using (S24), we can express the probability that a person in location m and age band a dies on day s after SARS-CoV-2 infection as

$$h_{msa} = \int_{s-0.5}^{s+0.5} \pi_{ma} h(u)du = \pi_{ma} \int_{s-0.5}^{s+0.5} h(u)du \quad \forall s = 2, 3, \ldots, \tag{S25}$$

and $h_{m1a} = \pi_{ma} \int_0^{1.5} h(u)du$ for $s = 1$. Using (S25), the expected number of COVID-19 deaths on day t in age band a in location m is

$$d_{mta} = \sum_{s=1}^{t-1} c_{msa} h_{m\,(t-s)\,a}, \tag{S26}$$

where c_{msa} is the expected number of new cases on day s in age band a in location m, (S14).

We link the expected number of death under the self-renewal model to the observed number deaths through an over-dispersed count model. For each location m, the data consist of daily, overall reported COVID-19 related deaths regardless of age until day $t_m^{\text{age-start}}$. For each location, time was re-scaled to 30 days prior to the first day when the cumulative number of deaths was 10 or larger. We denote the overall number of deaths on day t in location m by y_{mt} for $t < t_m^{\text{age-start}}$. From day $t_m^{\text{age-start}}$ onwards, COVID-19 related deaths are reported in location-specific age bands $b \in \mathcal{B}_m$. We denote the number of deaths on day t in location m in age band $b \in \mathcal{B}_m$ by y_{mtb} for $t \geq t_m^{\text{age-start}}$. To match the location-specific death data, we aggregate the expected number of deaths under the self-renewal model to

$$d_{mt} = \sum_{a \in \mathcal{A}} d_{mta} \quad \forall t < t_m^{\text{age-start}} \tag{S27}$$

$$d_{mtb} = \sum_{a \in b} d_{mta} \quad \forall t \geq t_m^{\text{age-start}}, \forall b \in \mathcal{B}_m. \tag{S28}$$

The log likelihood then consists of three parts,

$$\ell(\mathbf{y}|\theta) = \sum_m \Bigg[\sum_{t_m^{\text{start}} \le t < t_m^{\text{age-start}}} \log \text{NegBin}\big(y_{mt} \big| d_{mt}, \phi\big) + \tag{S29a}$$

$$\sum_{t=t_m^{\text{age-start}}} \sum_{b \in \mathcal{B}_m} \log \text{NegBin}\Big(\sum_{s=1}^{t_m^{\text{age-start}}} y_{msb} \Big| \sum_{s=1}^{t_m^{\text{age-start}}} d_{msb}, \phi\Big) + \tag{S29b}$$

$$\sum_{t_m^{\text{age-start}} < t \le t_m^{\text{end}}} \sum_{b \in \mathcal{B}_m} \log \text{NegBin}\big(y_{mtb} \big| d_{mtb}, \phi\big) \Bigg], \tag{S29c}$$

where t_m^{start} is the first day on which at least 10 cumulated deaths were reported in location m, and t_m^{end} corresponds to the last day with overall death, or death by age data, see Table S10.

S3.4 Inputs and prior distributions on model parameters

The COVID-19 age-specific transmission model has the following inputs, which we consider fixed, and model parameters, which we consider unknown and estimate (see Table S9). The total number of estimated parameters in the model is $30 + N_V + 7 \times M$, where M is the number of locations and N_V is the number of bi-weekly intervals, which for the central analysis amounted to 298 estimated parameters.

S3.4.1 Infection dynamics

Initial number of infections. For each location, the number of SARS-CoV-2 infections in the first 6 days of the observation period among individuals aged 20-54 are given the prior distribution

$$\log c_{m,t,[20-54]} \sim \mathcal{N}(4.5, 0.62^2), \quad t = 1, \ldots, 6 \tag{S30}$$

Recall that the observation period starts 30 days prior to the first day when the cumulative number of deaths in location m was 10 or larger. A priori we thus expect 90 infections to have occurred in the first 6 days among individuals aged 20-54 years. The new infections are then equally distributed across the corresponding age bands,

$$c_{m,t,a} = \begin{cases} c_{m,t,[20-54]}/7 & \text{if } a \in \mathcal{A}_0 \\ 0 & \text{otherwise,} \end{cases} \tag{S31}$$

where $\mathcal{A}_0 = \{[20-24], [25-59], [30-34], [35-39], [40-44], [45-49], [50-54]\}$ and $t = 1, \ldots, 6$. This prior specification is similar to the base model [54].

Location	Dates with overall data	Dates with death by age data	Number of age groups
Alabama	March 29, 2020 - May 02, 2020	May 03, 2020 - August 23, 2020	5
Alaska	-	-	-
Arizona	March 27, 2020 - May 12, 2020	May 13, 2020 - August 23, 2020	5
Arkansas	-	-	-
California	March 17, 2020 - May 12, 2020	May 13, 2020 - August 23, 2020	4
Colorado	March 25, 2020 - March 25, 2020	March 26, 2020 - August 23, 2020	9
Connecticut	March 23, 2020 - April 04, 2020	April 05, 2020 - August 23, 2020	9
Delaware	March 31, 2020 - May 11, 2020	May 12, 2020 - August 23, 2020	6
District of Columbia	April 02, 2020 - April 12, 2020	April 13, 2020 - August 23, 2020	8
Florida	March 20, 2020 - March 26, 2020	March 27, 2020 - August 23, 2020	10
Georgia	March 19, 2020 - May 05, 2020	May 06, 2020 - August 23, 2020	18
Hawaii	-	-	-
Idaho	April 04, 2020 - May 12, 2020	May 13, 2020 - August 23, 2020	8
Illinois	March 23, 2020 - May 13, 2020	May 14, 2020 - August 23, 2020	8
Indiana	March 24, 2020 - May 12, 2020	May 13, 2020 - August 23, 2020	8
Iowa	April 02, 2020 - May 12, 2020	May 13, 2020 - August 23, 2020	5
Kansas	-	-	-
Kentucky	March 30, 2020 - May 12, 2020	May 13, 2020 - August 23, 2020	9
Louisiana	March 19, 2020 - May 11, 2020	May 12, 2020 - August 23, 2020	7
Maine	-	-	-
Maryland	March 29, 2020 - May 13, 2020	May 14, 2020 - August 23, 2020	9
Massachusetts	March 24, 2020 - April 19, 2020	April 20, 2020 - August 23, 2020	8
Michigan	March 23, 2020 - March 23, 2020	March 24, 2020 - August 23, 2020	8
Minnesota	-	-	-
Mississippi	March 28, 2020 - April 26, 2020	April 27, 2020 - August 23, 2020	8
Missouri	March 28, 2020 - May 12, 2020	May 13, 2020 - August 23, 2020	8
Montana	-	-	-
Nebraska	-	-	-
Nevada	March 26, 2020 - June 06, 2020	June 07, 2020 - August 23, 2020	8
New Hampshire	April 08, 2020 - June 06, 2020	June 07, 2020 - August 23, 2020	9
New Jersey	March 20, 2020 - May 24, 2020	May 25, 2020 - August 23, 2020	7
New Mexico	April 03, 2020 - April 03, 2020	April 04, 2020 - August 23, 2020	8
New York	-	-	-
New York City	March 16, 2020 - June 30, 2020	July 01, 2020 - August 23, 2020	5
North Carolina	March 31, 2020 - May 19, 2020	May 20, 2020 - August 23, 2020	6
North Dakota	-	-	-
Ohio	-	-	-
Oklahoma	March 28, 2020 - May 12, 2020	May 13, 2020 - August 23, 2020	6
Oregon	March 25, 2020 - June 04, 2020	June 05, 2020 - August 23, 2020	9
Pennsylvania	March 25, 2020 - June 06, 2020	June 07, 2020 - August 23, 2020	8
Rhode Island	April 01, 2020 - May 31, 2020	June 01, 2020 - August 23, 2020	9
South Carolina	March 27, 2020 - May 13, 2020	May 14, 2020 - August 23, 2020	9
South Dakota	-	-	-
Tennessee	March 30, 2020 - April 08, 2020	April 09, 2020 - August 23, 2020	9
Texas	March 24, 2020 - July 27, 2020	July 28, 2020 - August 23, 2020	11
Utah	April 06, 2020 - June 16, 2020	June 17, 2020 - August 23, 2020	6
Vermont	-	-	-
Virginia	March 26, 2020 - April 20, 2020	April 21, 2020 - August 23, 2020	9
Washington	March 04, 2020 - June 07, 2020	June 08, 2020 - August 23, 2020	5
West Virginia	-	-	-
Wisconsin	March 26, 2020 - March 26, 2020	March 27, 2020 - August 23, 2020	9
Wyoming	-	-	-

Table S10: **Dates with overall and death by age data included in the likelihood.** Our analysis include 37 locations with death by age.

Infection parameters. The infection parameters described in (S11) comprise the baseline infection parameter in location m, ρ_{0m} (real-valued), as well as relative susceptibility (S) parameters ρ^S (vector-valued of length A).

To place a prior density on $\rho_{0,m}$, we consider prior estimates on the basic reproduction number [50], and specify the following prior distribution on the basic reproduction number $R_{0,m}$ in location m,

$$R_{0,m} \sim \mathcal{N}(3.28, \kappa), \tag{S32a}$$

$$\kappa \sim \mathcal{N}_{[0,\infty)}(0, 0.5). \tag{S32b}$$

where $\mathcal{N}_{[a,b)}$ denotes a truncated normal distribution between a and b. A common prior standard deviation is chosen to allow information to be shared between locations. This specification follows the base model [54]. To obtain $\rho_{0,m}$, we re-scale $R_{0,m}$ by the average number of contacts of one person in location m at baseline,

$$\rho_{0,m} = R_{0,m}/\bar{C}_m \tag{S33a}$$

$$\bar{C}_m = \sum_a p_{m,a} \sum_{a'} \mathbf{C}^{\text{wday}}_{m,a,a'}, \tag{S33b}$$

where $\mathbf{C}^{\text{wday}}_m$ is the baseline weekday contact matrix defined in S3.4.2 and $p_{m,a}$ is the proportion of the population of location m in age band a.

To place prior densities on the relative susceptibility parameters, we used available data from contact tracing and testing in mainland China [51]. Based on the available data, we considered relative susceptibility parameters for the age bands $[0-14]$, $[15-64]$ and $[65+]$, and specified the prior densities

$$\log \rho^S_{[0-14]} \sim \mathcal{N}(-1.0702, 0.2170^2) \tag{S34a}$$

$$\log \rho^S_{[65+]} \sim \mathcal{N}(0.3828, 0.1638^2), \tag{S34b}$$

were the hyperparameters were obtained by fitting a lognormal distribution to the reported 95% confidence intervals in [51] with the `lognorm` R package, version 0.1.6 [67].

The log susceptibility parameters for age band $[15-64]$ were set to 0, so that ρ^S is interpreted relative to infection dynamics from/to individuals in age band $[15-64]$. Considering the 18 age bands of the COVID-19 transmission model, the age-specific relative susceptibility parameters were set to

$$\log \rho^S_a = \begin{cases} \log \rho^S_{[0-14]} & \text{if } a \in [0-14] \\ \log \rho^S_{[15-64]} & \text{if } a \in [15-64] \\ \log \rho^S_{[65+]} & \text{if } a \in [65+]. \end{cases}, \tag{S35}$$

Discretised generation time distribution. The generation time distribution (S14) was kept fixed. Using estimates of [52], we specified the continuous-time version

$$g^{CT}(s) = \text{Gamma}(6.5, 0.62). \tag{S36}$$

Equation (S36) was then discretised to units of days,

$$g(s) = \int_{s-0.5}^{s+0.5} g^{CT}(u)\, du \quad \forall s = 2, 3, \ldots \tag{S37}$$

and $g(1) = \int_0^{1.5} g^{CT}(u)\, du$ for $s = 1$. This input specification is the same as in the base model [54].

S3.4.2 Time changing contact patterns

Baseline age-specific contact matrices The pre-pandemic contact intensity matrices were constructed using S1 and are illustrated in Figures S21-S24.

Mobility trend predictors. Changes in contact intensities were modelled through a regression on decomposed, age- and location-specific mobility trends. The mobility trend data used in this study are described in Section S1.2. The decomposition into baseline mobility trends $X^{\text{base}}_{m,t,a}$, eased mobility trends $X^{\text{eased}}_{m,t,a}$ and upswing multipliers $X^{\text{upswing}}_{m,t,a}$ on day t in location m and age band a is defined in (S20). The mobility predictors were kept fixed.

Mobility trend regression coefficients. Equations (S15) and (S21) describe our model of changing contact intensities, which depends on the regression coefficients β^{eased}_m and $\beta^{\text{upswing}}_{mt}$. We model the effect of the mobility trends prior to the rebound time (S6) through a spatial random effect,

$$\begin{aligned} \beta^{\text{eased}}_m &\sim \mathcal{N}(\beta^{\text{eased}}, \sigma^2_{\text{eased}}) \\ \beta^{\text{eased}} &\sim \mathcal{N}(0, 1) \\ \sigma_{\text{eased}} &\sim \text{Exponential}(5). \end{aligned} \tag{S38}$$

The effect of the mobility trends after the rebound time (S6) was allowed to vary in space and time to capture the observed heterogeneity in the mobility and death data. We modelled $\beta^{\text{upswing}}_{mt}$ through the factorisation

$$\beta^{\text{upswing}}_{mt} = \beta^{\text{upswing}}_m \times \beta^{\text{upswing}}_t \tag{S39}$$

where the spatial component was modelled as a random effect,

$$\begin{aligned}\beta_m^{\text{upswing}} &\sim \mathcal{N}(\beta^{\text{upswing}}, \sigma^2_{\text{upswing}})\\ \beta^{\text{upswing}} &\sim \mathcal{N}(0,1)\\ \sigma_{\text{upswing}} &\sim \text{Exponential}(10),\end{aligned} \tag{S40}$$

and the time component was modelled as a bi-weekly AR(1) process centered at zero,

$$\begin{aligned}\beta_t^{\text{upswing}} &= \varepsilon_{\lfloor c(t)/2 \rfloor},\\ \varepsilon_1 &\sim \mathcal{N}_{[0,\infty)}(0, 0.025),\\ \varepsilon_v &\sim \mathcal{N}_{[0,\infty)}(\varepsilon_{v-1}, \sigma_\varepsilon) \text{ for } v > 1,\\ \sigma_\varepsilon &\sim \text{Exponential}(10),\end{aligned} \tag{S41}$$

and $c(t)$ is a function that maps the time indices in location m to calendar weeks.

S3.4.3 Likelihood

Location and age-specific infection fatality ratio. The infection fatality ratio in location m and age band a is decomposed into

$$\pi_{m,a} = \exp(\log \pi_a + \log \delta_{m,a}), \tag{S42}$$

where $\log \pi_a$ are age-specific fixed effects, and $\log \delta_{m,a}$ are random effects for each location on a subset of age classes. To specify prior distributions on the age-specific fixed effects, we considered data from the meta-analysis of Levin and colleagues [68], and then adapted the statistical analysis to better reflect increasing uncertainty in infection fatality ratio estimates for young age groups. For the meta-analysis, we included data from Belgium, Sweden, and Geneva as in the original analysis [68], but excluded Spain due to difficulties in retrieving count data from the original sources cited in [68]. In addition, we included in the meta-analysis data from Iceland, New Zealand, and Korea, which were previously used for validation purposes [68]. Tables S11 and S12 present the sero-prevalence studies and comprehensive tracing programs data used in our re-analysis. Our meta-analysis is based on the actual death counts $d_{s,a}^{IFR}$ and estimated ranges for the number of infected individuals $c_{s,a}^{IFR}$ reported across 6 large scale studies s and various age bands, which are indexed in terms of the median age a of reported age bands as in [68]. We modelled the count data with a Beta-Binomial observation model, which allowed us to include observations with no reported deaths, and to account for overdispersion in the data. We used a logit link function for simplicity; results using a log link function were very similar. We allowed for non-linear departures

from linear, age-specific trends using a zero-mean Gaussian process model. The full model is

$$\begin{aligned} d_{s,a}^{\text{IFR}} &\sim \text{Beta-Binomial}\Big(c_{s,a}^{\text{IFR}},\ p_{s,a}^{\text{IFR}}\Phi,\ (1-p_{s,a}^{\text{IFR}})\Phi\Big) \\ \text{logit}\, p_{s,a}^{\text{IFR}} &= \beta_0^{\text{IFR}} + \beta_1^{\text{IFR}} * a + f_a + \nu_{s,a}^{\text{IFR}}, \end{aligned} \tag{S43}$$

with prior densities

$$\begin{aligned} \beta_0^{\text{IFR}} &\sim \mathcal{N}(0, 20) \\ \beta_1^{\text{IFR}} &\sim \mathcal{N}(0, 1) \\ \nu_{s,a}^{\text{IFR}} &\sim \mathcal{N}(0, \sigma_{\text{Meta}}^2) \\ \sigma_{\text{Meta}} &\sim \text{Half-Cauchy}(0, 1) \\ \mathbf{f} &\sim \text{GP}\big(0, K(\alpha^{\text{GP}}, \rho^{\text{GP}})\big) \\ \alpha^{\text{GP}} &\sim \mathcal{N}(0, 2) \\ \rho^{\text{GP}} &\sim \text{Inverse-Gamma}(11, 400) \\ 1/\Phi &\sim \text{Half-Cauchy}(0, 1), \end{aligned} \tag{S44}$$

where the Gaussian process covariance function is specified by the exponential quadratic kernel K with marginal variance parameter α^{GP} and length scale ρ^{GP}. We sought to capture long-range non-linear age trends through the GP, and for this reason specified for the length scale a prior density with 1% and 99% quantiles of 20 and 84 years. The model was fitted with CmdStan release 2.23.0 (22 April 2020), using 3 adaptive Hamiltonian Monte Carlo Sampler [69] with 10,000 iterations each, of which the first 5,000 iterations are considered as a burn-in. The chains mixed and converged, the minimum and maximum effective sample sizes were respectively $1,961$ and $34,270$. Moreover, the Rhat statistics range was 0.9998 and 1.001. Figure S29 shows the posterior predictive distribution of the infection fatality ratio on the log scale, along with the data used in the meta-analysis. We estimate substantial uncertainty in predicted infection fatality ratios among individuals below age 40, and this uncertainty allows the model to explore the possibility of large case numbers among individuals below age 40. We then fitted log-normal distributions to the numerical estimates of the 95% credible intervals associated with the posterior predictive infection fatality ratios using the `lognorm` R package, version 0.1.6 [67], and specified the prior distribution on the log infection fatality ratio for each age band used in the model through

$$\log \pi_a \sim \mathcal{N}(\mu_a, \sigma_a^2), \tag{S45}$$

where μ_a and σ_a for the 18 increasing age bands in this study are reported in Table S13. Figure S29b compares our prior distribution (S45) to that obtained from the meta-analysis of Levin and colleagues [68].

The prior (S42) further included a location-specific random effect for adults aged $[20-49]$, which we denote by $\delta_{m,[20-49]}$, a location-specific random effect for adults aged $[50-69]$, which we denote by $\delta_{m,[50-69]}$, and a

location-specific random effect for individuals aged 70 or older, which we denote by $\delta_{m,[70+]}$. The corresponding prior distributions were

$$\log \delta_{m,[20-49]} \sim N(0, \sigma^2_{[20-49]}), \tag{S46a}$$

$$\log \delta_{m,[50-69]} \sim N(0, \sigma^2_{[50-69]}), \tag{S46b}$$

$$\sigma_{[20-49]}, \sigma_{[50-69]} \sim \text{Exponential}(10), \tag{S46c}$$

$$\log \delta_{m,[70+]} \sim \text{Exponential}(\lambda_{[70+]}), \tag{S46d}$$

$$\lambda_{[70+]} \sim \text{Exponential}(0.05). \tag{S46e}$$

The parameter $\log \delta_{m,[70+]}$ was restricted to be positive in order reduce collinearity between model parameters.

Location	Dates	Age bands	Population size	(Sero-)prevalence estimates (in %) (mean and 95% confidence interval)	Deaths	Source
Belgium	March - April, 2020 / May 9, 2020	$0-24$	$3,228,894$	$6.00\ [4.20, 8.60]$	2	[70]
		$25-44$	$2,956,684$	$5.90\ [4.20, 8.30]$	30	
		$45-64$	$3,080,528$	$6.20\ [4.70, 8.30]$	409	
		$65-74$	$1,147,009$	$4.10\ [2.30, 7.20]$	$1,061$	
		$75-84$	$690,685$	$7.00\ [4.20, 11.70]$	$2,144$	
		$85+$	$326,659$	$13.20\ [8.90, 19.60]$	$5,087$	
England	June 20 - July 13, 2020 / July 17, 2020	$18-44$	$18,1904,73$	$7.13\ [6.69, 7.64]$	524	[71]†
		$45-64$	$13,449,179$	$6.17\ [5.77, 6.67]$	$4,657$	[72]†
		$65-74$	$4,552,283$	$3.20\ [2.80, 3.60]$	$7,105$	[73]†
		$75+$	$3,704,429$	$3.30\ [2.90, 3.80]$	$36,341$	
Geneva	May 6, 2020 / June 1, 2020	$5-9$	$26,466$	$4.53\ [1.51, 9.07]$	0	[74]
		$10-19$	$53,180$	$11.47\ [7.33, 16.55]$	0	
		$20-49$	$219,440$	$13.12\ [9.75, 17.00]$	2	
		$50-64$	$98,528$	$10.45\ [7.31, 14.11]$	16	
		$65+$	$83,574$	$6.82\ [3.83, 10.53]$	268	
Spain	March 20 - June 22, 2020 / July 15, 2020	$0-9$	$4,283,800$	$3.73\ [2.28, 6.04]$	5	[75]
		$10-19$	$4,954,600$	$4.01\ [3.09, 5.19]$	6	
		$20-29$	$4,883,200$	$5.74\ [4.66, 6.97]$	35	
		$30-39$	$5,990,500$	$4.95\ [4.11, 5.95]$	77	
		$40-49$	$7,794,500$	$5.33\ [4.59, 6.19]$	295	
		$50-59$	$7,057,300$	$5.22\ [4.49, 6.07]$	$1,023$	
		$60-69$	$5,401,600$	$4.95\ [4.12, 5.95]$	$2,653$	
		$70-79$	$3,921,800$	$4.66\ [3.68, 5.87]$	$6,131$	
		$80+$	$2,599,100$	$4.84\ [3.48, 6.69]$	$9,003$	
Sweden	May 18 - May 24, 2020 / June 1 - June 7, 2020	$0-19$	$2,297,477$	$5.30\ [3.31, 7.93]$	1	[76]†
		$20-64$	$5,711,699$	$7.60\ [5.14, 10.81]$	604	[77]†
		$65+$	$2,008,354$	$3.89\ [2.06, 6.52]$	$4,433$	[78]†

Table S11: **Summary of the sero-prevalence studies used to formulate the infection fatality rate prior.** Dates presented are the seroprevalence study date / deaths data date. †: England and Sweden's references are, in order, for the population size, seroprevalence estimates and mortality counts.

Location	Dates	Age bands	Population size	Prevalence estimates (in %) (mean and 95% confidence interval)	Deaths	Source
Iceland	Feb 1-Jun 15	$0-29$	$135,576$	$0.41\ [0.30, 0.50]$	0	[68]
		$30-39$	$46,871$	$1.10\ [0.80, 1.60]$	1	
		$40-49$	$42,966$	$1.50\ [1.10, 2.00]$	0	
		$50-59$	$42,111$	$0.80\ [0.50, 1.30]$	0	
		$60-69$	$37,536$	$0.50\ [0.30, 1.00]$	2	
		$70-79$	$23,415$	$0.30\ [0.20, 1.30]$	3	
		$80+$	$12,775$	$0.20\ [0.10, 2.50]$	4	
Korea	Feb 1-May 17	$0-29$	$15,623,365$	$0.06\ [0.03, 0.08]$	0	[68]
		$30-39$	$7,079,839$	$0.04\ [0.02, 0.07]$	2	
		$40-49$	$8,218,844$	$0.04\ [0.02, 0.06]$	3	
		$50-59$	$8,476,699$	$0.06\ [0.03, 0.08]$	15	
		$60-69$	$6,453,706$	$0.05\ [0.03, 0.08]$	41	
		$70-79$	$3,560,646$	$0.05\ [0.03, 0.07]$	84	
		$80+$	$1,856,084$	$0.06\ [0.03, 0.09]$	144	
New Zealand	Feb 1-Jul 9	$0-29$	$1,911,472$	$0.06\ [0.03, 0.08]$	0	[68]
		$30-39$	$619,066$	$0.08\ [0.04, 0.12]$	0	
		$40-49$	$591,874$	$0.07\ [0.04, 0.11]$	0	
		$50-59$	$628,691$	$0.08\ [0.04, 0.12]$	0	
		$60-69$	$522,312$	$0.07\ [0.04, 0.10]$	3	
		$70-79$	$361,832$	$0.04\ [0.02, 0.07]$	7	
		$80+$	$186,985$	$0.04\ [0.02, 0.06]$	12	

Table S12: **Summary of the countries with a comprehensive tracing program used to formulate the infection fatality ratio prior.** Dates presented are the period of cases and deaths observation. In countries with a comprehensive tracing program, the number of cases detected is considered representative of the actual number of cases.

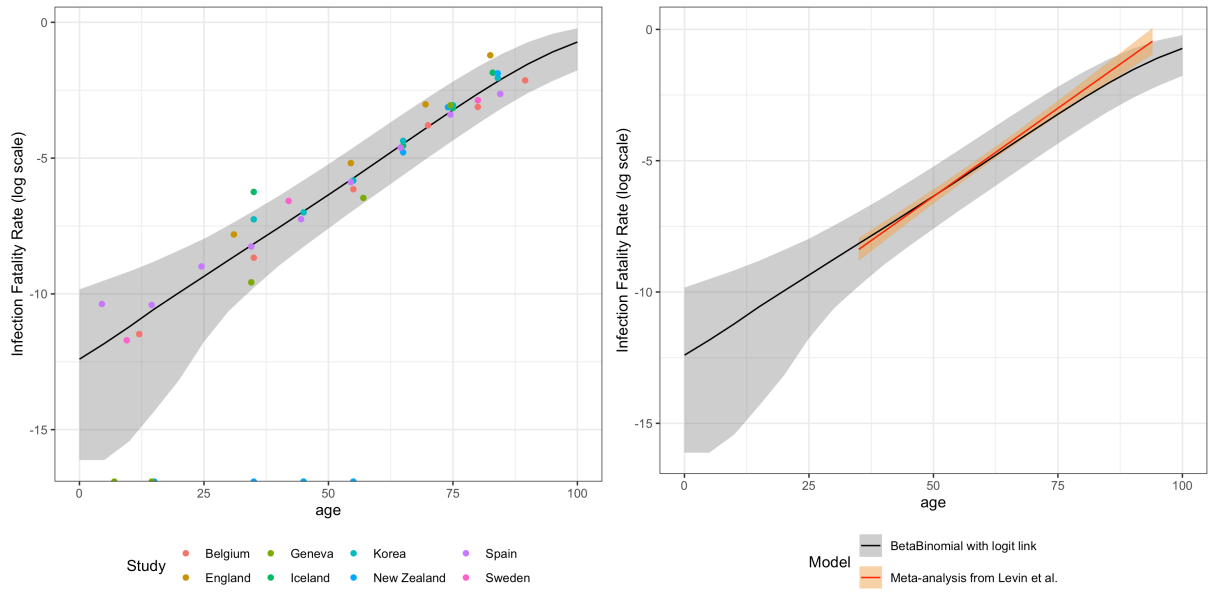

(a) Comparison to data

(b) Comparison to analysis in [68]

Figure S29: **Predicted infection fatality ratios.** (a) Comparison of the posterior predictive infection fatality ratios against the data used to fit model (S43). Shown are the posterior predictive median (line), 95% posterior predictive credible interval, and ratios of observed deaths over expected number of cases on the log scale (points). (b) Comparison of the posterior predictive infection fatality ratios with the prediction intervals from the meta-analysis of Levin and colleagues [68] (provided in their Supplementary Material).

The age-specific random effects $\log \delta_{m,a}$ for each of the 18 age bands in this study were then set to

$$\log \delta_{m,a} = \begin{cases} \log \delta_{m,[20-49]} & \text{if } a \in [20-49] \\ \log \delta_{m,[50-69]} & \text{if } a \in [50-69] \\ \log \delta_{m,[70+]} & \text{if } a \in [70+] \\ 0 & \text{otherwise.} \end{cases} \tag{S47}$$

Infection-to-death distribution. The infection-to-death distribution h in (S24) was kept fixed. Following [79, 66], we first specified the infection-to-onset-of-symptoms distribution and the onset-to-death, and modelled the infection-to-death distribution as the sum of both components through

$$h(s) = \text{Gamma}(s; 5.1, 0.86) + \text{Gamma}(s; 17.8, 0.45), \tag{S48}$$

where s is in continuous time. This input specification is the same as in the base model [80].

	$[0-4]$	$[5-9]$	$[10-14]$	$[15-19]$	$[20-24]$	$[25-29]$
μ_a	-12.4045236	-11.8276362	-11.2128209	-10.5612676	-9.9547808	-9.3553661
σ_a	1.2848842	1.1614624	1.017873	0.8757987	0.7785512	0.6912288
	$[30-34]$	$[35-39]$	$[40-44]$	$[45-49]$	$[50-54]$	$[55-59]$
μ_a	-8.7522828	-8.15568	-7.5638957	-6.9594171	-6.3526927	-5.7362489
σ_a	0.6404053	0.6055523	0.582907	0.5704648	0.5636325	0.562268
	$[60-64]$	$[65-69]$	$[70-74]$	$[75-79]$	$[80-84]$	$[85+]$
μ_a	-5.1077053	-4.4738832	-3.848234	-3.229631	-2.6304859	-1.3551168
σ_a	0.5588437	0.5518728	0.5418635	0.5229684	0.4969032	0.3616957

Table S13: **Hyperparameters of the prior density on age-specific infection fatality ratios, equation** (S45)**.**

Overdispersion parameter. The prior distribution on the overdispersion parameter ϕ in the Negative Binomial observation model (S29) was given by the prior density

$$\phi \sim \mathcal{N}_{[0,\infty)}(0,5). \tag{S49}$$

S3.5 Computational inference

The Bayesian hierarchical model was fit with CmdStan release 2.23.0 (22 April 2020), using an adaptive Hamiltonian Monte Carlo (HMC) sampler [69]. 8 HMC chains were run in parallel for $2,000$ iterations, of which the first $1,500$ iterations were specified as warm-up. Calculations for each HMC chain were distributed over 1 processor per U.S location (state or metropolitan area) with CmdStan's `reduce_sum` functionality. Posterior convergence was assessed using the Rhat statistics and by diagnosing divergent transitions of the sampler. There are 4,000 iterations after burn-in across 8 chains, and 10 parameters with the lowest effective sample sizes were assessed. Those effective sample sizes of are from 589 to 781, and Rhats are from 1.0034 to 1.0159. There were 4092 divergent transitions, and that the average posterior step size was around 0.004. The pair plot of parameters for New York City is in Figure S30.

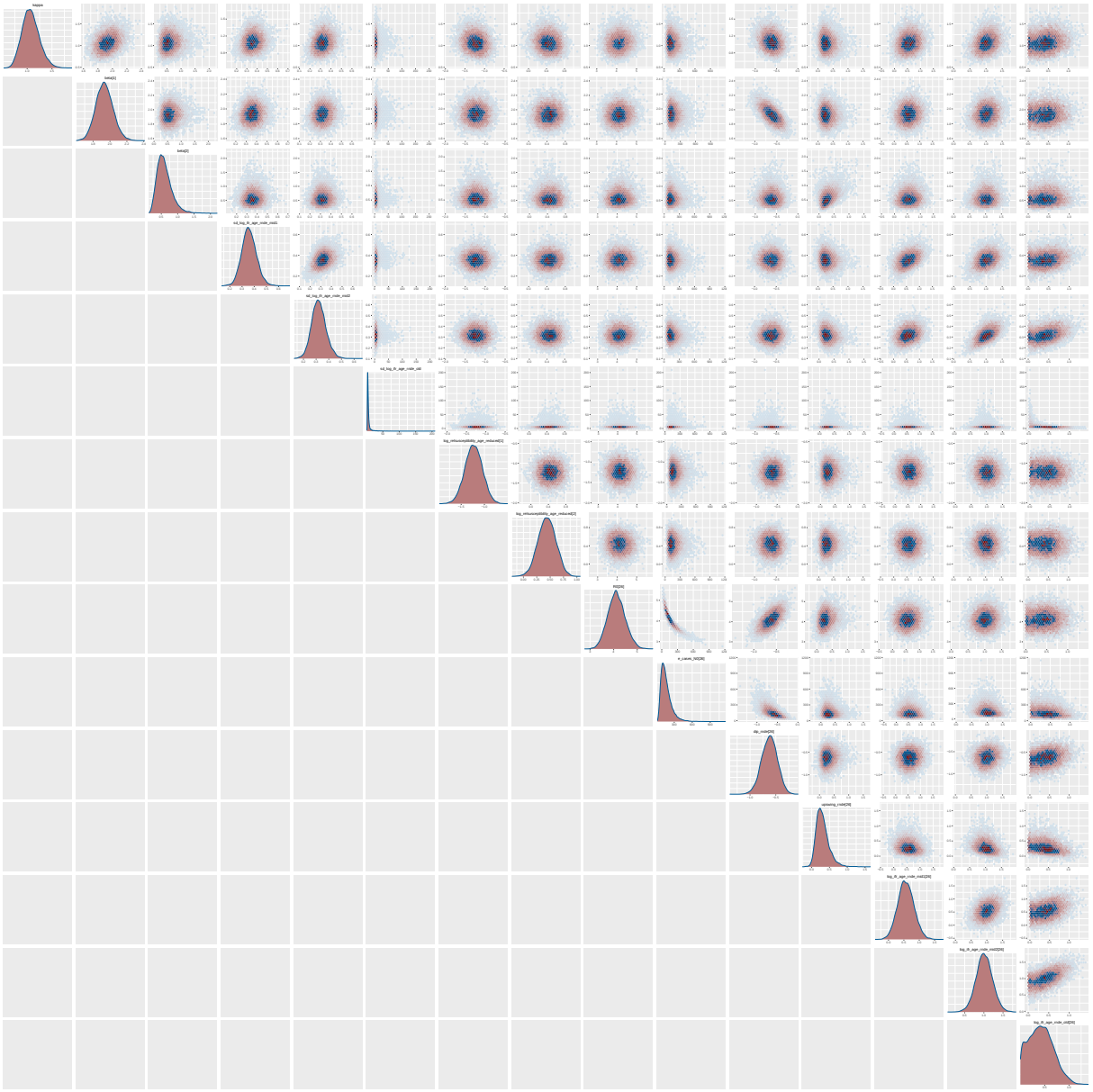

Figure S30: **Pair plots of the joint posterior distribution of the model parameters for New York City.**

DOI: https://doi.org/10.25561/82551

S3.6 Generated quantities

Age stratification for reporting purposes. In the manuscript results are reported using the following 8 age bands

$$d \in \mathcal{D} = \Big\{[0-9], [10-19], [20-34], [35-49], [50-64], [65-79], [80+]\Big\}. \tag{S50}$$

Posterior samples were recorded in the 18 age bands used in the model ($[0-4]$, $[5-9]$, $\ldots$, $[85+]$) and then aggregated to the stratification $\mathcal{D}$ using

$$\begin{aligned} R_{m,t,d} &= \sum_{a \in d} \frac{c^*_{m,t,a}}{\sum_{k \in d} c^*_{m,t,k}} R_{m,t,a}, \\ c_{m,t,d} &= \sum_{a \in d} c_{m,t,a}, \\ d_{m,t,d} &= \sum_{a \in d} d_{m,t,a}, \end{aligned} \tag{S51}$$

where $c^*_{m,t,a}$ is the number of infectious individuals in location m and time t that is in age band a defined in (S54), $R_{m,t,a}$ is defined in (S12), $c_{m,t,a}$ is defined in (S14) and $d_{m,t,a}$ is defined in (S8).

Estimated cumulated COVID-19 attack rates by age and over time. We calculate the percentage of the population in m and in age band d that has been infected up to day t through

$$A_{m,t,d} = \frac{\sum_{s=1}^{t} c_{m,s,d}}{N_{m,d}}, \tag{S52}$$

where $N_{m,d}$ is the number of individuals in location m and age band d, and $c_{m,s,d}$ is defined in (S51). We also refer to (S52) as the age-specific cumulative attack rate. Similarly, we calculate the percentage of the population in m that has been infected up to day t through

$$A_{m,t} = \frac{\sum_d \sum_{s=1}^{t} c_{m,s,d}}{\sum_d N_{m,d}} = \sum_d \frac{N_{m,d}}{N_m} A_{m,t,d}, \tag{S53}$$

where N_m is the number of individuals in location m. We also refer to (S53) as the cumulative attack rate.

Estimated number of infectious individuals by age and over time. The effective number of infectious individuals c^* in location m and age band d on day t is calculated by weighing how infectious a previously infected individual is on day t,

$$c^*_{m,t,d} = \sum_{s=1}^{t-1} c_{m,s,d}\, g(t-s), \tag{S54}$$

where g appears in (S14). Similarly, the effective number of infectious individuals c^* in location m on day t is calculated by

$$c^*_{m,t} = \sum_d \sum_{s=1}^{t-1} c_{m,s,d}\, g(t-s) = \sum_{s=1}^{t-1} c_{m,s}\, g(t-s). \tag{S55}$$

Estimated time-varying reproduction number of COVID-19 over time. The overall time-varying reproduction number on day t in location m is given by

$$R_{m,t} = c_{m,t}/c^*_{m,t} \tag{S56}$$

where $c_{m,t}$ is the number of new cases on day t in location m, and $c^*_{m,t}$ is the number of infectious individuals on day t in location m [81]. Equation (S56) can be re-arranged to

$$R_{m,t} = \sum_a c^*_{m,t,a}/c^*_{m,t} R_{m,t,a}, \tag{S57}$$

where $R_{m,t,a}$ is defined in (S12).

Estimated age-specific SARS-CoV-2 transmission flows. Following on from Equation (S14), the transmission flows from age group a to age group a' at time t in location m are,

$$F_{m,t,a,a'} = s_{m,t,a'}\, \rho_{a'}\, \mathbf{C}_{m,t,a,a'} \left(\sum_{s=1}^{t-1} c_{m,s,a}\, g(t-s) \right), \tag{S58}$$

where $s_{m,t,a'}$ is defined in (S13), $\rho_{a,a'}$ is defined in (S11), and $\mathbf{C}_{m,t,a,a'}$ is defined in (S15). In terms of the age bands reported in the main text, the transmission flows by aggregated age groups are

$$F_{m,t,d,d'} = \sum_{a \in d, a' \in d'} F_{m,t,a,a'}. \tag{S59}$$

Estimated contribution of age groups to SARS-CoV-2 transmission. Following on from Equation (S58), the age-specific contribution of infections from age band a in location m on day t is

$$S_{m,t,a} = \left(\sum_{a'} F_{m,t,a,a'} \right) \Big/ \left(\sum_a \sum_{a'} F_{m,t,a,a'} \right). \tag{S60}$$

The age-specific contribution of infections are proportions, such that $\sum_a S_{m,t,a} = 1$ for all a. In terms of the age bands reported in the main text, the aggregated contribution of infections in age band d in location m on day t are equal to

$$S_{m,t,d} = \left(\sum_{d'} F_{m,t,d,d'} \right) \Big/ \left(\sum_d \sum_{d'} F_{m,t,d,d'} \right). \tag{S61}$$

National averages. Several quantities are reported at the national level by age,

$$R_{t,d} = \sum_m \frac{c^*_{m,t,d}}{\sum_l c^*_{l,t,d}} R_{m,t,d}, \tag{S62}$$

$$c_{t,d} = \sum_m c_{m,t,d}, \tag{S63}$$

$$d_{t,d} = \sum_m d_{m,t,d}, \tag{S64}$$

where $c^*_{m,t,d}$ is the number of infectious individuals at time t in location m and age band d, defined in (S54), and $R_{m,t,d}$, $c_{m,t,d}$ and $d_{m,t,a}$ are defined in (S51). Finally, for reporting at the national level regardless of age, we calculated

$$R_t = \sum_m \sum_{d \in \mathcal{D}} \frac{c^*_{m,t,d}}{\sum_l \sum_{k \in \mathcal{D}} c^*_{l,t,k}} R_{m,t,d}, \tag{S65}$$

$$c_t = \sum_d c_{t,d}, \tag{S66}$$

$$d_t = \sum_d d_{t,d}. \tag{S67}$$

S3.7 Forecasts

Forecast period. School re-opening scenarios were generated for 90 days, for the time period August 24, 2020 to November 24, 2020.

Contact and transmission intensities during school re-opening scenarios. In the school re-opening scenarios, children aged 0-11 were modelled to resume their typical contact intensities. As the contact-and-infection model is specified in terms of the 5-year age bands (S10), the contact intensities for children aged 10-14 were modelled through a mixture approach,

$$\mathbf{C}_{m,t,a,a'} = \begin{cases} \mathbf{C}_{m,a,a'} & \text{if } t < t_m^{\text{school-close}} \\ \mathbf{C}_{a,a'}^{COVID-0-14} & \text{if } t \in [t_m^{\text{school-close}}, t_m^{\text{school-reopen}} - 1] \\ \mathbf{C}_{m,a,a'} & \text{if } t \geq t_m^{\text{school-reopen}} \text{ and } a < 10 \text{ or } a' < 10 \\ \frac{2}{5}\mathbf{C}_{m,a,a'} + \frac{3}{5}\mathbf{C}_{a,a'}^{COVID-0-14} & \text{if } t \geq t_m^{\text{school-reopen}} \text{ and } a = 10-14 \text{ or } a' = 10-14 \end{cases} \tag{S68}$$

where the school re-opening date $t_m^{\text{school-reopen}}$ was set to August 24, 2020 in all locations, $\mathbf{C}_{m,a,a'}$ is the baseline pre-COVID-19 contact matrix described in Section S3.2.2, and $\mathbf{C}_{a,a'}^{COVID-0-14}$ is the average contact matrix during lockdown of [51] described in Section S3.2.4, and a or a' are one of $[0-4]$, $[5-9]$, $[10-14]$.

We further considered that due to other preventative interventions, transmissions rates involving children aged

0-11 are modulated by a factor $\beta^{\text{fc-0-11}}$, and we considered school re-opening scenarios using the values

$$\beta^{\text{fc-0-11}} = 0.2, 0.33, 0.5, 1.0, \tag{S69}$$

which were motivated by the effect sizes reported in [82]. Due to the mixture approach in (S68), we incorporated the prevention effect parameter $\beta^{\text{fc-0-11}}$ on the contact intensities rather than the transmission intensities in the renewal equation (S14),

$$\mathbf{C}_{m,t,a,a'} = \begin{cases} \mathbf{C}_{m,a,a'} & \text{if } t < t_m^{\text{school-close}} \\ \mathbf{C}_{a,a'}^{COVID-0-14} & \text{if } t \in [t_m^{\text{school-close}}, t_m^{\text{school-reopen}} - 1] \\ \beta^{\text{fc-0-11}}\mathbf{C}_{m,a,a'} & \text{if } t \geq t_m^{\text{school-reopen}} \text{ and } a < 10 \text{ or } a' < 10 \\ \frac{2}{5}\beta^{\text{fc-0-11}}\mathbf{C}_{m,a,a'} + \frac{3}{5}\mathbf{C}_{a,a'}^{COVID-0-14} & \text{if } t \geq t_m^{\text{school-reopen}} \text{ and } a = 10-14, \\ & \text{or } a' = 10-14 \end{cases} \tag{S70}$$

where a or a' are one of $[0-4]$, $[5-9]$, $[10-14]$.

Contact intensities among individuals aged $15+$ were modelled as before based on the mobility trends in equations (S15) and (S21) where the required mobility trend predictors were imputed, and for weekdays set to the average over the last 5 weekdays, and for weekends set to the average over the last 4 weekend days.

Contact and transmission intensities during school re-opening scenarios. In the school closure scenarios, contact intensities remained unchanged, and corresponded to (S70) with $t_m^{\text{school-reopen}} = \infty$. Contact intensities among individuals aged $15+$ were modelled as before based on the mobility trends in equations (S15) and (S21) where the required mobility trend predictors were imputed, and for weekdays set to the average over the last 5 weekdays, and for weekends set to the average over the last 4 weekend days.

Age stratification for school re-opening forecasting scenarios. To investigate the impact of re-opening day care, kindergartens, and elementary schools, we used the age bands

$$\tilde{d} \in \tilde{\mathcal{D}} = \Big\{[0-11], [12-19], [20-34], [35-49], [50-64], [65-79], [80+]\Big\}. \tag{S71}$$

and then aggregated to the stratification $\tilde{\mathcal{D}}$ analogously to (S51). We introduce the superscript x to denote the various scenarios, e.g. re-opening of kindergartens and elementary schools, or continued closure of kindergartens and elementary schools. Then, the time-varying reproduction numbers in the forecast period/scenarios were calculated through

$$R^x_{m,t,\tilde{d}} = \begin{cases} \frac{p_{m,[0-4]}R^x_{m,t,[0-4]} + p_{m,[5-9]}R^x_{m,t,[5-9]} + \frac{2}{5}p_{m,[10-14]}R^x_{m,t,[10-14]}}{p_{m,[0-4]} + p_{m,[5-9]} + \frac{2}{5}p_{m,[10-14]}} & \text{if } \tilde{d} = [0-11] \\ \frac{\frac{3}{5}p_{m,[10-14]}R^x_{m,t,[10-14]} + p_{m,[15-19]}R^x_{m,t,[15-19]}}{\frac{3}{5}p_{m,[10-14]} + p_{m,[15-19]}} & \text{if } \tilde{d} = [12-19] \\ \sum_{a\in\tilde{d}} \frac{p_{m,a}}{\sum_{k\in d} p_{m,k}} R^x_{m,t,a} & \text{if } \tilde{d} > 19, \end{cases} \tag{S72}$$

and the number of daily new cases through

$$c^x_{m,t,\tilde{d}} = \begin{cases} c^x_{m,t,[0-4]} + c^x_{m,t,[5-9]} + \frac{2}{5}c^x_{m,t,[10-14]} \text{ if } \tilde{d} = [0-11] \\ \frac{3}{5}c^x_{m,t,[10-14]} + c^x_{m,t,[15-19]} \text{ if } \tilde{d} = [12-19] \\ \sum_{a\in\tilde{d}} c^x_{m,t,a} \text{ if } \tilde{d} > 19, \end{cases} \tag{S73}$$

and the number of daily deaths through

$$d^x_{m,t,\tilde{d}} = \begin{cases} d^x_{m,t,[0-4]} + d^x_{m,t,[5-9]} + \frac{2}{5}d^x_{m,t,[10-14]} \text{ if } \tilde{d} = [0-11] \\ \frac{3}{5}d^x_{m,t,[10-14]} + d^x_{m,t,[15-19]} \text{ if } \tilde{d} = [12-19] \\ \sum_{a\in\tilde{d}} d^x_{m,t,a} \text{ if } \tilde{d} > 19, \end{cases} \tag{S74}$$

and the contribution of age group $\tilde{d}$ to onward spread on day t in location m and scenario x through

$$S^x_{m,t,\tilde{d}} = \begin{cases} S^x_{m,t,[0-9]} + \frac{2}{10}S^x_{m,t,[10-19]} \text{ if } \tilde{d} = [0-11] \\ \frac{8}{10}S^x_{m,t,[10-19]} \text{ if } \tilde{d} = [12-19] \\ S^x_{m,t,d} \text{ if } \tilde{d} > 19. \end{cases} \tag{S75}$$

Predicted excess infections and deaths, percent increases in infections and deaths. Based on (S72-S75), the excess number of cases in the re-opening scenarios versus the continued closure scenario was calculated as

$$c^{\text{excess}}_{m,t,\tilde{d}} = c^{\text{reopen}}_{m,t,\tilde{d}} - c^{\text{close}}_{m,t,\tilde{d}}, \tag{S76}$$

and the percent increase in cases was calculated as

$$c^{\text{pc-increase}}_{m,t,\tilde{d}} = c^{\text{reopen}}_{m,t,\tilde{d}} / c^{\text{close}}_{m,t,\tilde{d}} - 1. \tag{S77}$$

Predicted excess deaths and percent increases in deaths were calculated analogously. Predicted percent increase in the time varying reproduction number were also calculated analogously.

S4 Supplementary Text: Comparison of model outputs to estimated contact intensities during the pandemic

The SARS-CoV-2 transmission model presented in Section S3.1 makes detailed predictions on the time evolution of age-specific contact patterns during the pandemic. As a form of external model validation, we here compare the model predictions against data from contact survey studies.

In the United States, the Berkeley Interpersonal Contact Study (BICS) was designed to measure the effects of social distancing on contact patterns during the pandemic, and began in spring 2020 [83]. Their study included adults aged 18+ and wave 0 was conducted between March 22 to April 08, 2020. In this wave, approximately half the study participants were from five cities (New York, San Francisco Bay Area, Atlanta, Phoenix, Boston) with the rest from around the rest of the US. In their initial analyses, the study authors found that individuals had a mean of 2.7 conversational contacts with similar IQR when compared to the study of Jarvis et al. [63] in the UK: 85% of respondents reported four or fewer contacts. Despite wide confidence intervals, these figures indicate substantial reductions in the overall number of contacts in the early phase of the pandemic, and early after lockdown or stay at home orders were issued.

We compared the estimates from the two contact surveys to the average number of contacts at the midpoint of the wave 0 period of the BICS study, March 28, 2020 (Table S14). To match the study sample of the BICS study, we report estimates for two metropolitan areas included in the model analysis (New York City and District of Columbia), and an overall estimate for the United States obtained by averaging across all states evaluated, New York City, and the District of Columbia. Overall, the COVID-19 contact and infection model estimates similar strong reductions in the number of daily contacts, with a probability of one that overall, the average number of daily contacts by individuals of all ages was at most four.

	Number of daily contacts [95% credible intervals]	Posterior probability of at most 4 daily contacts
District of Columbia	2.56 [1.8 - 3.75]	100%
New York City	2.75 [2.13 - 3.59]	100%
United States	2.75 [2.56 - 2.94]	100%

Table S14: **Estimated number of contacts on March 28, 2020 (midpoint of BICS wave0 study).** Posterior median and 95% credible intervals in brackets. We include a weighted average across the United States and two cities which were included in the BICS study.

We also compared the age breakdown of daily number of conversational contacts from the BICS study with our model estimates for New York City, District of Columbia and a national average. Figure S31 indicates good agree-

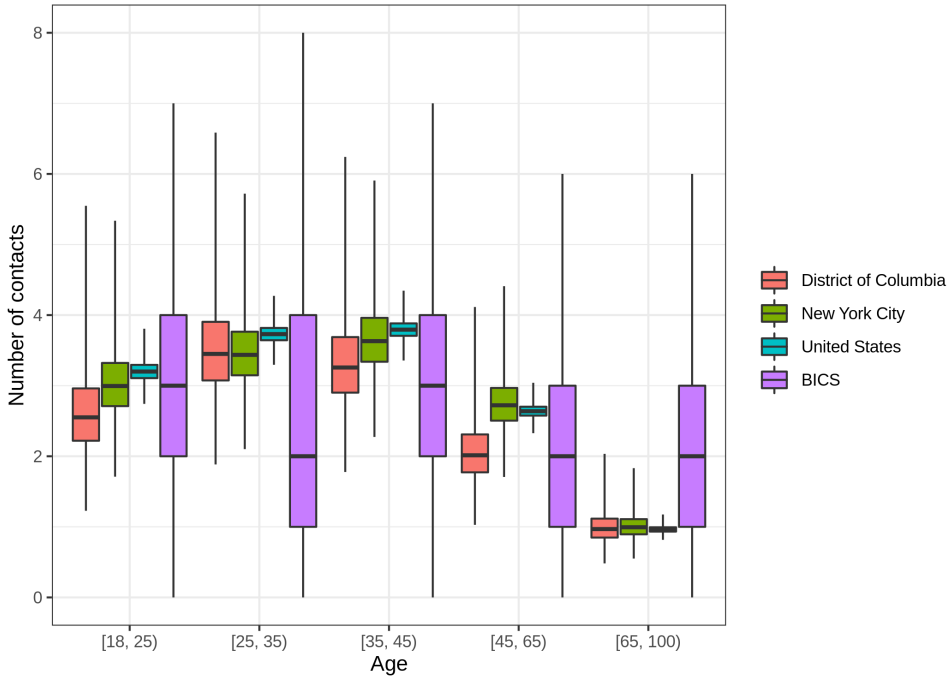

Figure S31: **Estimated daily number of contacts per age band on March 28, 2020 (midpoint of BICS wave0 study).**

ment between the estimates of the BICS study and model fits.

DOI: https://doi.org/10.25561/82551

S5 Supplementary Text: Comparison of model outputs to seroprevalence estimates

To further assess model fit, we reviewed data from several large-scale COVID-19 seroprevalence surveys in the United States, and qualitatively compared the sero-prevalence estimates from the antibody surveys to the estimates under the contact and infection model at location (state or metropolitan area) level.

We included 14 COVID-19 antibody surveys from across the United States in this comparison (Table S15). 13 studies were conducted by the U.S. Centers for Disease Control & Prevention (CDC) in 7 locations, Connecticut, Florida, Louisiana, Missouri, New York City, Utah, and Washington. Two rounds of seroprevalence surveys were done in each location, except Louisiana where one seroprevalence survey was performed. The surveys included individuals who had blood specimens tested for reasons unrelated to COVID-19 [84], and thus the study samples may not be representative of the underlying populations. For instance, the CDC compared the predicted number of total infections obtained under the COVID-19 sero-prevalence estimates to the number of reported cases, and found that in most locations, approximately one in ten cases were reported. However for the study in Connecticut, the ratio was one in six, and for the study in Missouri, the ratio was one in 24, suggesting that the study samples in these locations may not be representative. The final survey included in the comparison was also from New York City [85], and included participants recruited through flyers at the entrances of grocery stores. Individuals who are less likely to visit grocery stores may have lower infection risk (e.g. because of self-isolation) or higher infection risk (e.g. quarantine after infection), and estimates from this study may also be subject to unknown biases.

In all studies, IgM and IgG enzyme-linked immunosorbent assays (ELISA) were used to test for COVID-19 antibodies. Common limitations of these tests are that infected individuals with antibodies may test negative (false negatives), uninfected individuals without antibodies may test positive (false positives), that infected individuals may not yet have developed antibodies (antibody eclipse phase), and that infected individuals may have already lost antibodies (sero-reversion). The above studies adjusted sero-prevalence estimates for false positive and false negative rates, however re-analyses of manufacturer sensitivity and specificity figures suggest that these numbers may have to be considered with caution [53]. To account for the antibody eclipse phase, we calculated as part of the infection model the number of expected infected individuals with antibodies. Specifically, COVID-19 symptoms are estimated to develop on average 6 days after infection (estimated range 2 to 14 days) [87] and individuals are estimated to develop IgG antibodies on average 14 days after symptom onset (estimated range 7 to 21 days) [88, 89]. Based on these estimates, we specified the infection-to-onset-of-symptoms distribution and

the onset-to-antibody distribution as the sum of both components through

$$k(s) = \text{Gamma}(s; 5.1, 0.86) + \text{Normal}(s; 14, 3.57) \tag{S78}$$

where s is in continuous time. We then express the probability that a person in location m and age band a develops antibodies on day s after SARS-CoV-2 infection as

$$k_s = \int_{s-0.5}^{s+0.5} k(u)du = \int_{s-0.5}^{s+0.5} k(u)du \quad \forall s = 2, 3, \ldots, \tag{S79}$$

and $k_s = \int_0^{1.5} k(u)du$ for $s = 1$. Using (S79), the expected number of infected individuals that develop COVID-19 antibodies on day t in age band a in location m is

$$b_{m,t,a} = \sum_{s=1}^{t-1} c_{m,s,a}\, k_{t-s}, \tag{S80}$$

where $c_{m,s,a}$ is the expected number of new cases on day s in age band a in location m, (S14). With regards to sero-reversion, we note that the above studies were completed by early June. Based on the resulting short time frame since onset of the pandemic, we assumed that infected individuals did not seroревert. We thus calculated the expected proportion of individuals with COVID-19 antibodies on day t in location m as

$$s_{m,t} = \Big(\sum_a \sum_{s=1}^{t} b_{m,s,a} \Big) / N_m, \tag{S81}$$

Study	Round	Period	Number of participants
Connecticut	1	Apr 26 - May 3	1431
	2	May 21 - May 26	1800
Louisiana	1	Apr 1 - Apr 8	1184
	2	-	-
Minnesota	1	Apr 30 - May 12	860
	2	May 25 - Jun 7	1323
Missouri	1	Apr 20 - Apr 26	1882
	2	May 25 - May 30	1831
New York City Metro Area	1	Mar 23 - Apr 1	2482
	2	Apr 25 - May 6	1116
Philadelphia Metro Area	1	Apr 13 - Apr 25	824
	2	May 26 - May 30	1743
San Francisco Bay Area	1	Apr 23 - Apr 27	1224
	2	-	-
South Florida	1	Apr 6 - Apr 10	1742
	2	Apr 20 - Apr 24	1280
Utah	1	Apr 20 - May 3	1132
	2	May 25 - Jun 5	1940
Western Washington Region	1	Mar 23 - Apr 1	3264
	2	Apr 27 - May 11	1719

Table S15: **Characteristics of large-scale antibody studies used for the comparison.** All dates are for the year 2020. Data were retrieved from the CDC dashboard [86].

where N_m is the number of individuals in location m. The day of comparison was set to the last day of the study period. For the New York City study [85], the Utah study, and the second round of the Florida study, individuals up to age 18 were excluded from calculation of the sero-prevalence estimate (S81), because of small sample sizes in the surveys.

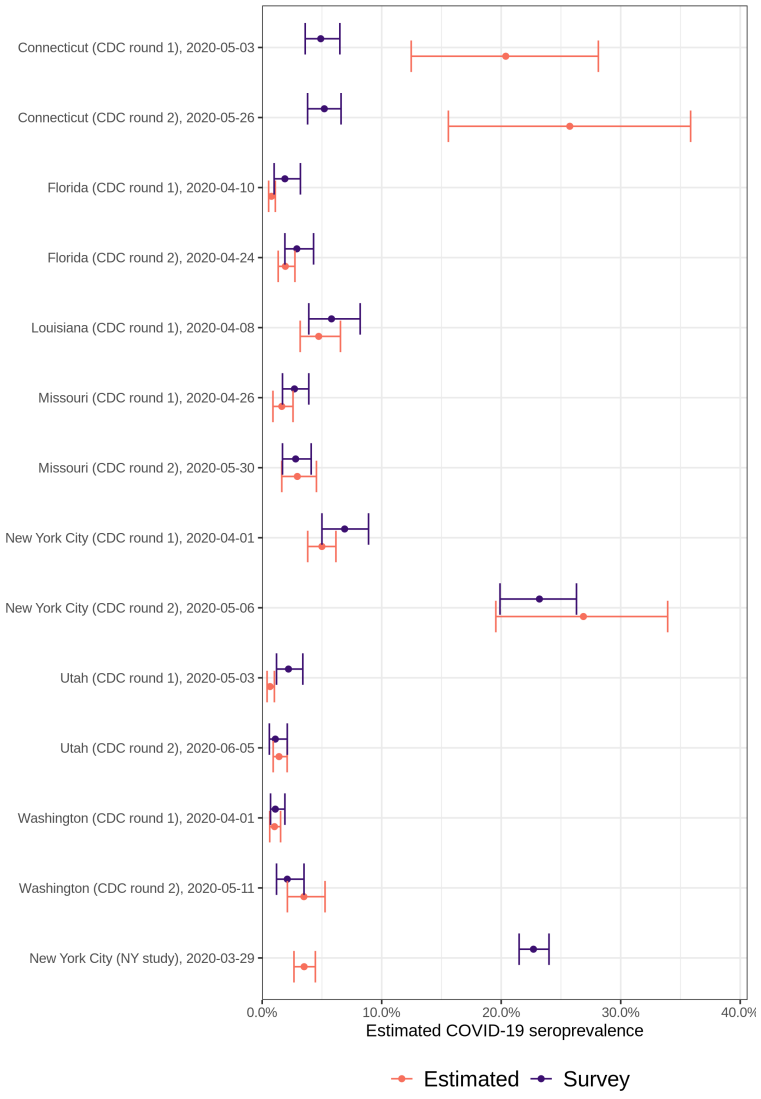

Figure S32: **Comparison between estimates of COVID-19 seroprevalence under the contact and infection model with those from large-scale antibody studies.** Shown are posterior medians and 95% credible intervals for model output, and estimates as reported from the antibody studies, for the dates reported by the studies.

Figure S32 compares the expected proportion of individuals with COVID-19 antibodies (S81) to study estimates.

For Connecticut, the model estimates considerably higher seroprevalence levels than the CDC study. However under the estimates of the CDC study, the ratio of expected to observed cases was unusually low at 6:1, suggesting that seroprevalence was likely underestimated in that study by a factor of two. For Florida, survey samples were collected in South Florida, which experienced higher numbers of reported cases and contributed disproportionately towards total deaths within the state. This suggests that survey estimates likely overstated seroprevalence compared to the state as a whole, and the implications on our comparison are unclear. For the round 1 study in Missouri, we note the ratio of expected to observed cases was unusually high at 24:1, suggesting that seroprevalence was likely overestimated in the study by a factor of two. For the New York metropolitan area, the catchment area increased from round 1 to round 2 to include Long Island, suggesting that the survey estimates could understate seroprevalence compared to New York City in early May. For Utah, the round 2 point estimate is significantly lower than that of round 1. For Washington, survey samples were collected in the Western region, which also experienced higher case and death numbers than the Eastern part of Washington state, suggesting that survey estimates could have overstated state-level seroprevalence. The second New York City study [85] found considerably higher seroprevalence estimates at a time point before the first CDC study in New York City. Our model estimates appear to be more in line with the sero-prevalence estimates of the two CDC studies in New York City. Based on these considerations, we focus on a broad, more qualitative comparison between the model and seroprevalence estimates. Using previous version of the contact-and-infection model with infection fatality ratio priors based on [66] and on [53], the model estimates were consistently 30% to 50% below the survey estimates. This prompted us to revisit previous infection fatality ratio estimates as described in Supplementary Text S3, suggesting greater uncertainty in infection fatality ratio estimates among individuals aged 40 and below. In turn, this uncertainty allowed the model to explore the possibility of more cases among individuals aged 40 and below, and lead to inferences that appear to be overall more consistent with available sero-prevalence estimates. The corresponding cumulative attack rates estimates are presented in Table S3.

S6 Supplementary Text: Sensitivity analyses

S6.1 Alternative assumptions on age-specific infection fatality ratios

The central analysis is based on the prior density (S45) on infection fatality ratios (IFR). The contact and infection model is sensitive to the assumed IFR prior, as any model that infers disease dynamics from COVID-19 attributable deaths [54]. In sensitivity analyses, we considered an alternative IFR prior density using the predicted mean and 95% prediction intervals of age-specific IFRs derived in the meta-analysis of Levin and colleagues [68]. The meta-analysis estimated age-specific IFRs for ages 35 and above, however for the model analysis estimates for younger age groups are required. We thus extrapolated the predicted mean and 95% prediction intervals in [68] under their linear model as shown in Figure S33. We refer to the resulting IFR prior density as the log IFR prior constructed from the Levin et al meta-analysis.

Then, we refitted the contact-and-infection model using the log IFR prior constructed from the Levin et al meta-analysis. Figure S35 compares the cumulative attack rates estimated under the central model to those under the model with log IFR prior constructed from the Levin et al. meta-analysis. The greater uncertainty in IFR values for young individuals translates into greater uncertainty on cumulative attack rates, with the central model less certain about how many individuals have been infected to date in several states. In addition, the posterior median estimates of cumulative attack rates are higher under the central model, when the IFR prior density allows exploring the possibility of more infections among young individuals. Figure S36 compares the seroprevalence estimates under both models to the estimates of the antibody study described in Supplementary Text S5. Seroprevalence estimates are lower when the model is used in conjunction with the log IFR prior constructed from the Levin et al. meta-analysis, suggesting larger differences relative to the estimates of the CDC antibody studies when seroprevalence is low, and smaller differences relative to the estimates of the CDC antibody studies when seroprevalence is high. On this basis we chose the infection fatality ratio prior with larger uncertainty for the central analysis.

Figure S37 compares estimates of age-specific reproduction numbers, and the contribution of age groups to onward spread under the central and alternative model. Both models make similar inferences on age-specific disease spread, with larger uncertainty estimates under the central model.

DOI: https://doi.org/10.25561/82551

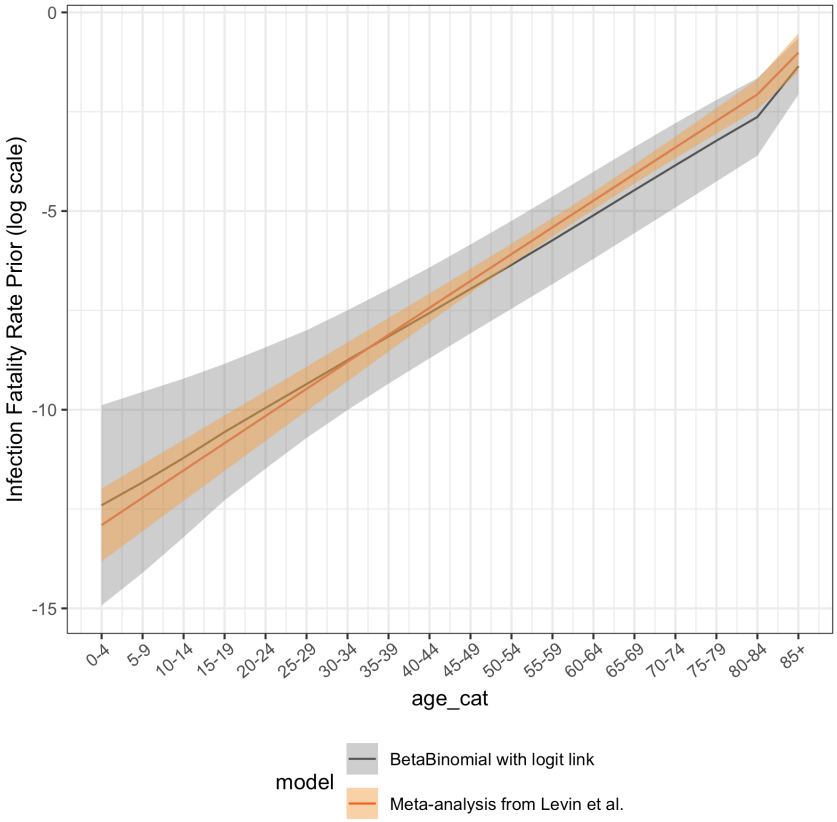

Figure S33: **Comparison of the IFR prior used in the central analysis to the log IFR prior constructed from the Levin et al meta-analysis**. Mean and 95% uncertainty ranges of the two prior densities are shown as lines and ribbons, with the IFR prior used in the central analysis (S45) shown in grey, and the log IFR prior constructed from the Levin et al meta-analysis shown in orange.

DOI: https://doi.org/10.25561/82551

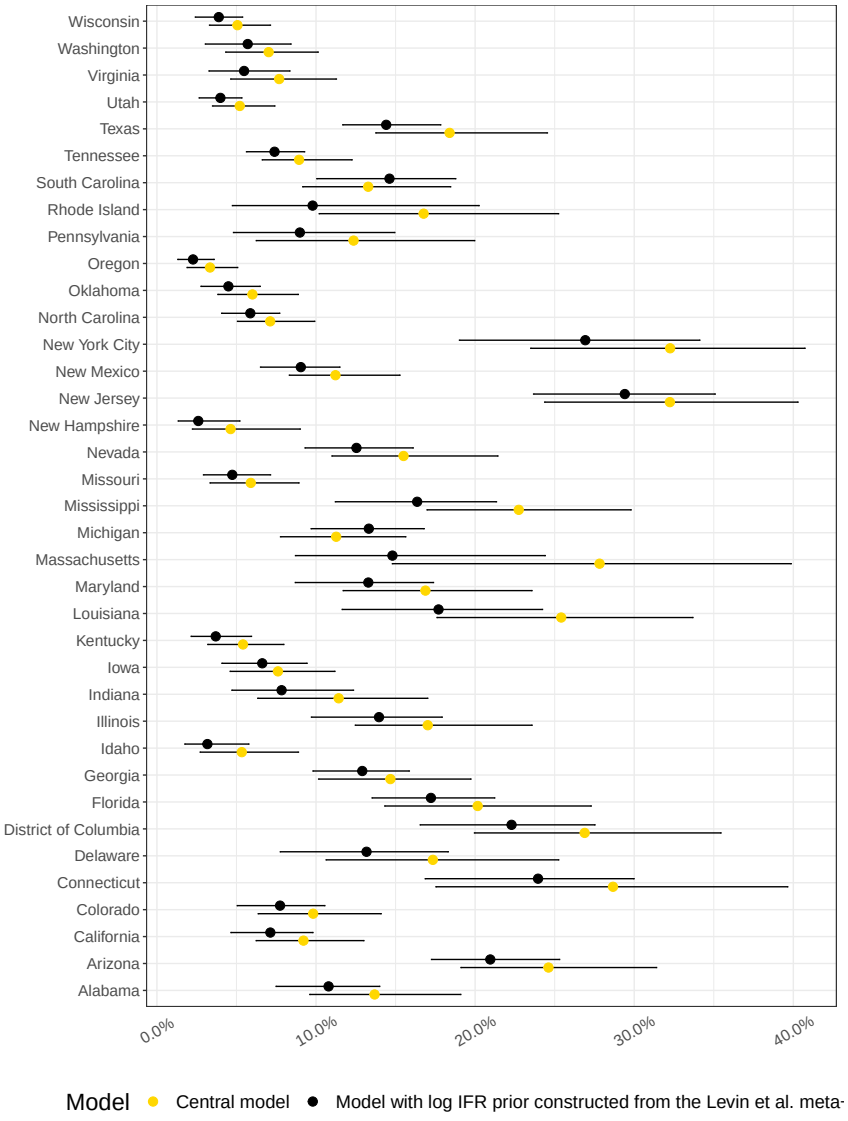

Figure S34: **Overall cumulative attack rate estimates under the central model and under the model using the log IFR prior constructed from the Levin et al meta-analysis, as of August 23, 2020.** Dots and error bars indicate the median posterior and the 95% confidence intervals, respectively. Central model in yellow and alternative model in black.

DOI: https://doi.org/10.25561/82551

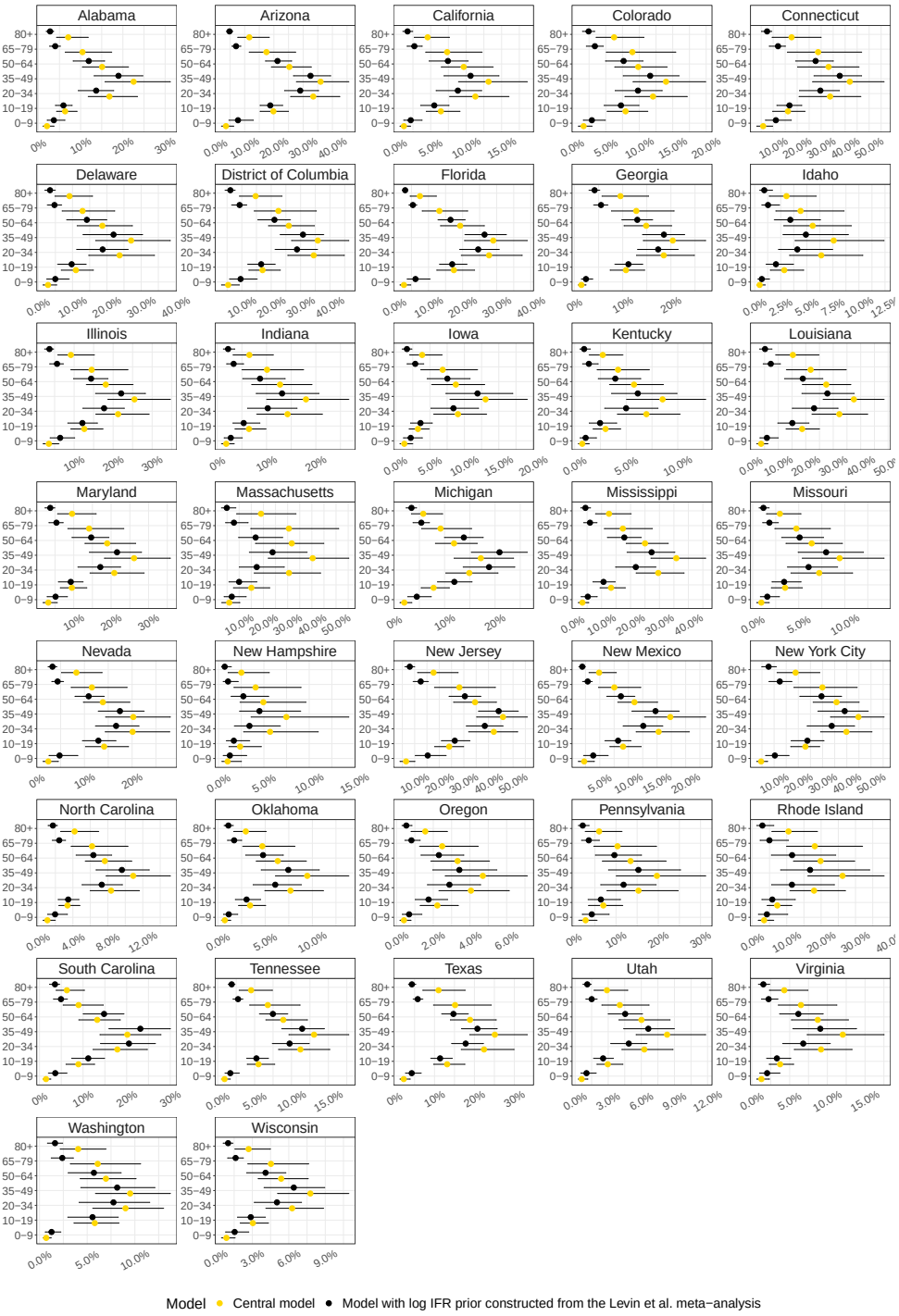

Figure S35: **Age-specific cumulative attack rate estimates under the central model and under the model using the log IFR prior constructed from the Levin et al. meta-analysis, as of August 23, 2020.** Dots and error bars indicate the median posterior and the 95% confidence intervals, respectively. Central model in yellow and alternative model in black.

DOI: https://doi.org/10.25561/82551

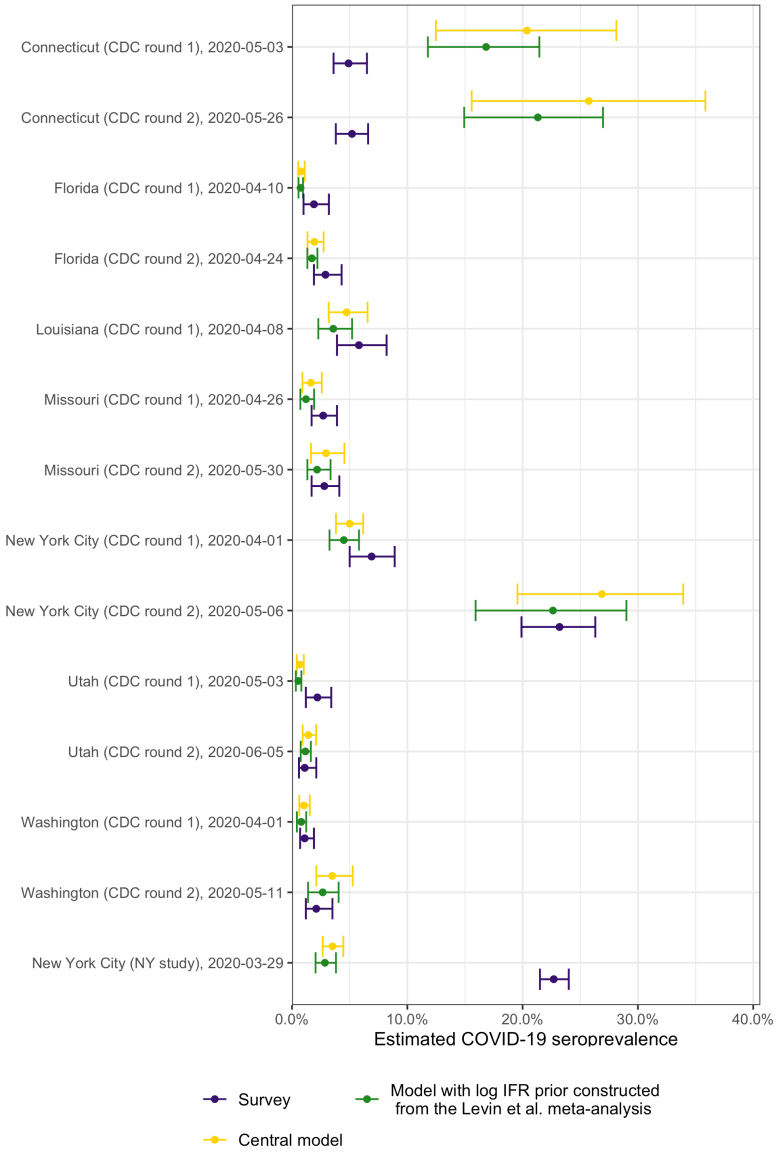

Figure S36: **Comparison of large-scale seroprevalence studies estimates with the expected seroprevalence under the central model and the model using the log IFR prior constructed from the Levin et al. meta-analysis.** Shown are posterior medians and 95% credible intervals for model output, and estimates as reported from seroprevalence studies, for the dates reported by the studies and assuming a 0-day lag.

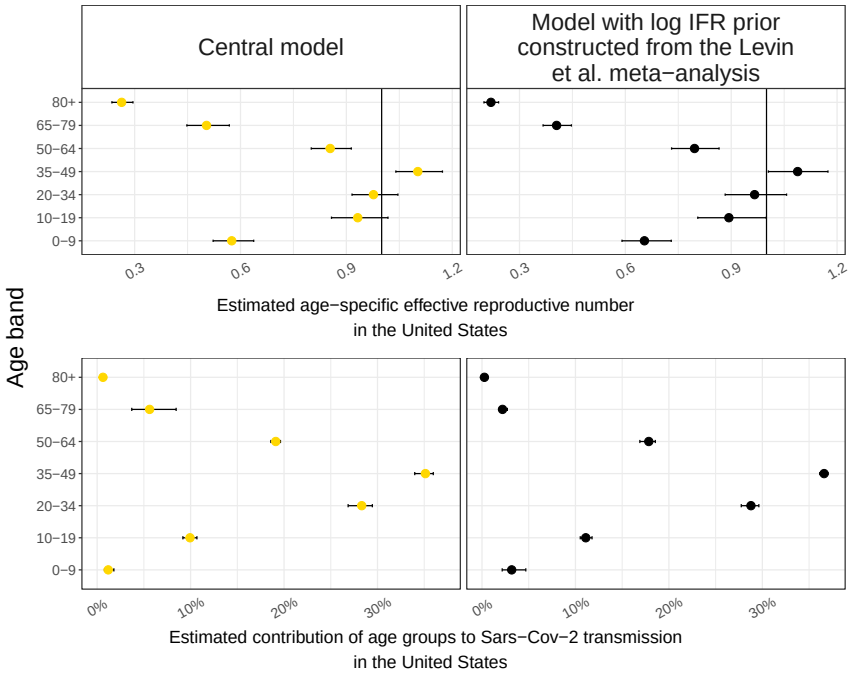

Figure S37: **Age-specific weekly reproduction numbers and contribution of age groups to onward spread under the central model and under the model using the log IFR prior constructed from the Levin et al meta-analysis.** (Top) Estimated weekly age-specific reproduction numbers for the week starting on August 17, 2020 under the central model (yellow) and the model using the log IFR prior constructed from the Levin et al meta-analysis (black). Dots and error bars indicate the median posterior and the 95% confidence intervals, respectively. (Bottom) Estimated cumulative contribution of age groups to onward spread as of August 24, 2020.

S6.2 Alternative assumptions on contact intensities from and to children aged 0-14 during the pandemic

The cell-phone derived population-level mobility data used in this study were only available for individuals aged $18+$. We rely on limited data from two contact surveys performed in the United Kingdom and China [63, 51] as described in Section S3.2 to characterise contact patterns from and to younger individuals during the pandemic. Specifically, in the central analysis, the $3 * 3 + (18 - 3) * 3 + 3 * (18 - 3) = 99$ contact intensities from or to children aged 0-14 were set to the corresponding, average contact intensities observed during lockdown in the study of Zhang and colleagues [51], as specified in (S23).

In sensitivity analyses we explored the impact of lower or higher contact intensities from or to children aged 0-14 during school closures. We approached this by reformulating (S23) to the following form,

$$\mathbf{C}_{m,t,a,a'} = \begin{cases} \mathbf{C}_{m,a,a'} & \text{if } t < t_m^{\text{school-close}} \\ \tau \mathbf{C}_{a,a'}^{COVID-0-14} & \text{if } t \geq t_m^{\text{school-close}}, \end{cases} \quad \text{(S82)}$$

where $a \in \{[0-4], [5-9], [10-14]\}$ and a' is one of the 5-year age bands of the infection-and-contact model, or a is one of the 5-year age bands and $a' \in \{[0-4], [5-9], [10-14]\}$, $t_m^{\text{school-close}}$ is the time index when school closures were ordered or recommended in location m, $\mathbf{C}_{m,a,a'}$ are the baseline pre-COVID-19 contact intensities described in location m in Section S3.2.2, $\mathbf{C}_{a,a'}^{COVID-0-14}$ are the average contact intensities derived from [51], and τ is a new scaling factor that we introduce for the purpose of sensitivity analyses.

To gauge a reasonable range of τ values, we first calculated the contact intensity ratios between the city-level contact matrices in [51] with the contact intensities $\mathbf{C}_{a,a'}^{COVID-0-14}$ that were used in the central analysis. The maximum contact intensity ratio was 2.00 and the minimum was 0.15. Using data from the UK post lockdown contact survey of Jarvis and colleagues [63], we also computed the mean contact intensities from individuals aged $18+$ with children aged $0-4$ and children age $5-17$. We repeated calculations for the average post-lock down contact matrix $\mathbf{C}^{COVID-0-14}$ of Zhang [51]. The minimum and maximum ratio in the corresponding contact intensities were 1.15 and 1.82. We thus performed two sensitivity analyses using $\tau = 0.5$ and 2, subject to the constraint that the resulting contact intensities during lockdown were not larger than those at baseline.

Further, we undertook a fourth sensitivity analysis in which the mobility trends seen among individuals 18-24 were extrapolated to younger individuals aged 0-17. In this analysis, time-varying contact intensities were estimated based on Equation (S15) for all age groups, and the data from the Zhang et al. contact surveys were not used. Figure S38 compares, for one location, the implied contact intensities used in the sensitivity analyses to those in the central analysis, which are shown as $\tau = 1$.

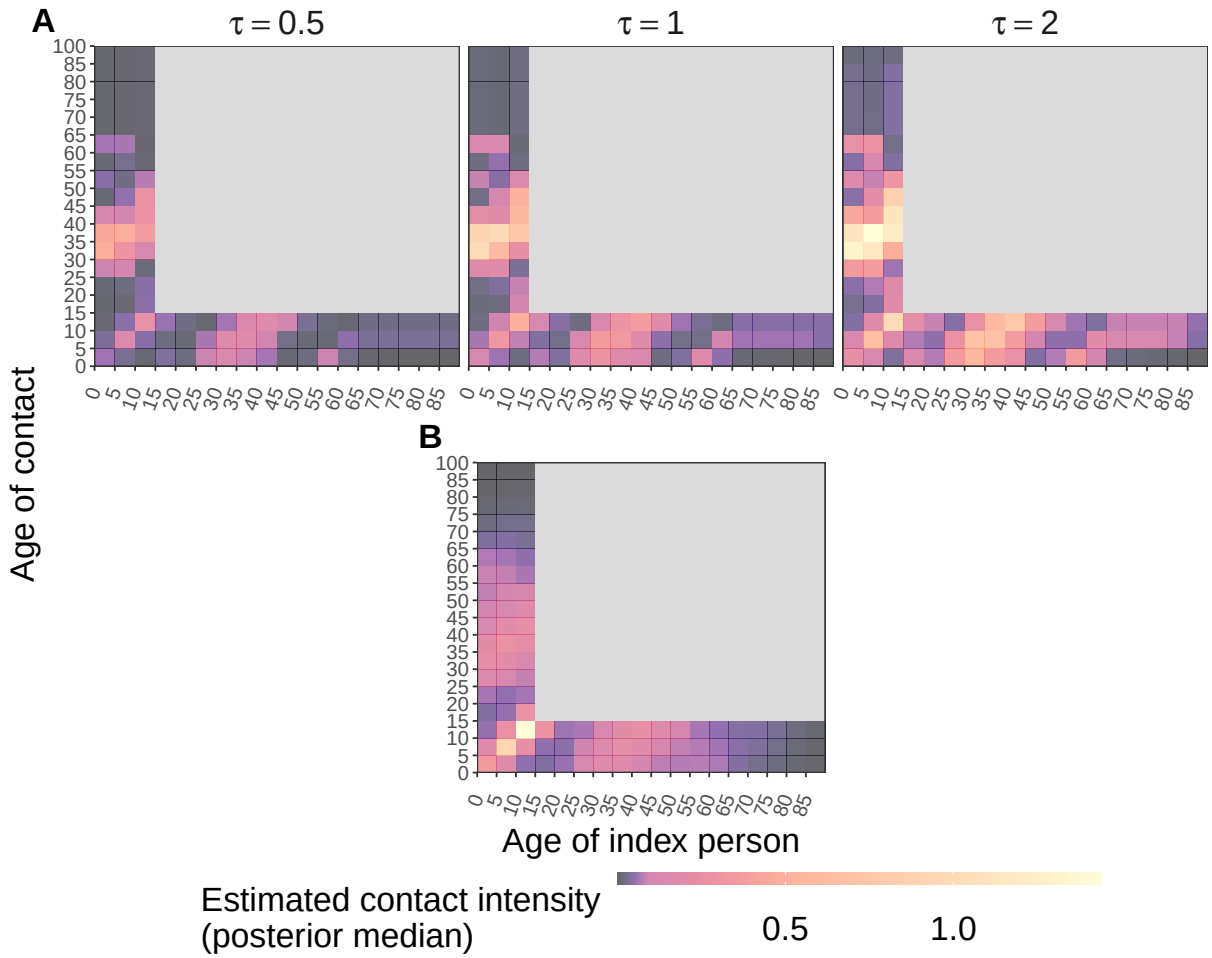

Figure S38: **Comparison of contact intensities from and to children aged 0-14 during periods of school closures in the sensitivity analyses. (A)** Rescaled contact intensities based on estimates of Zhang and colleagues [51]. Shown are contact intensities from and to children under Equation (S82) for different values of τ. The value $\tau = 1$ corresponds to the central model. **(B)** Inferred contact intensities from and to children based on extrapolating mobility trends of individuals aged 18-24 to younger individuals. Shown are the estimated contact intensities in California on April 15, 2020. Parts of the time varying contact matrices that are the same in the central model and the sensitivity analyses are plotted in grey.

Then, we re-fitted the contact-and-infection model. Figure S39 compares estimates of age-specific reproduction numbers, and the contribution of age groups to onward spread under the central and alternative models. The alternative model assumptions lead to considerable differences in estimated reproduction numbers by age groups. For children aged $0-9$, we estimate reproduction numbers ranged from 0.30 [0.26, 0.34] to 0.75 [0.66, 0.86] as τ

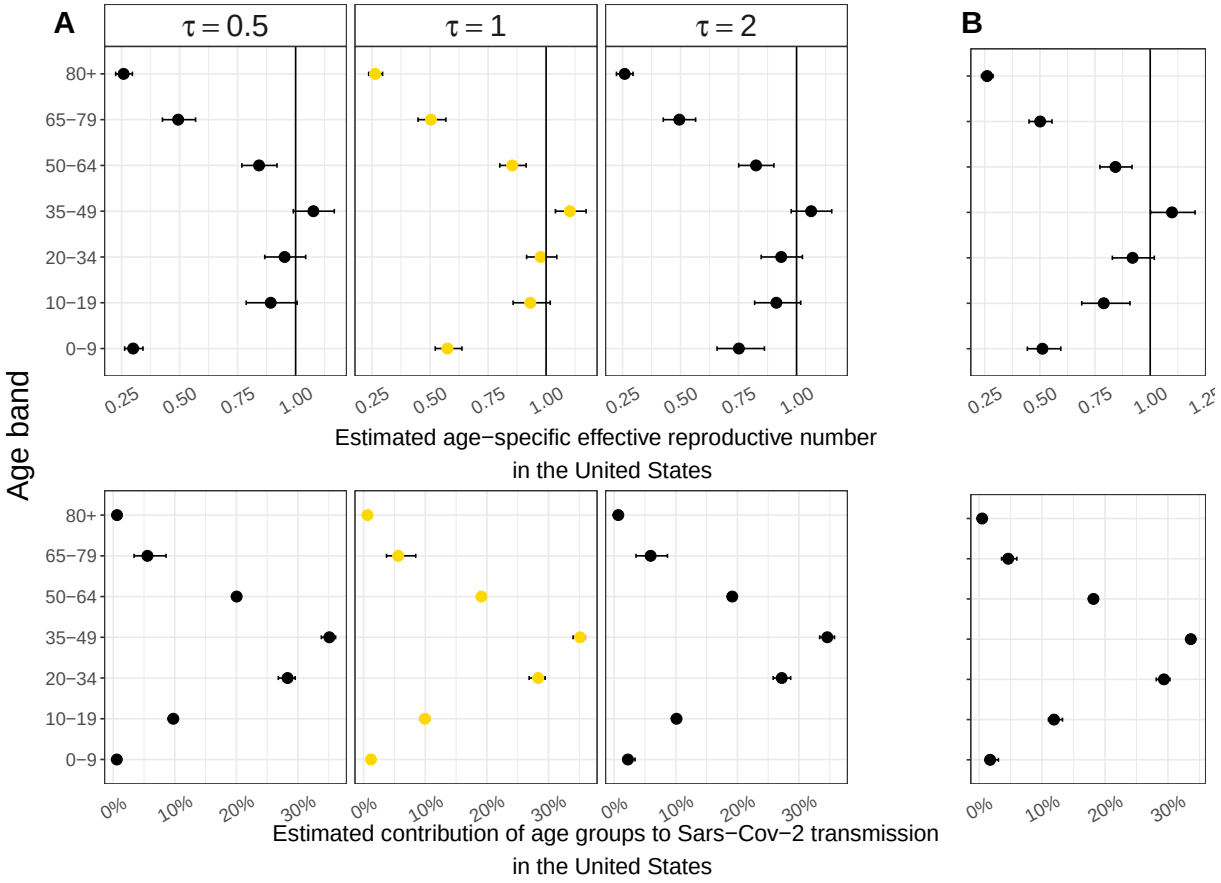

Figure S39: **Age-specific weekly reproduction numbers and contribution of age groups to onward spread under the central model and under the alternative models using different assumption on contact intensities from and to children aged** 0-14**.** Shown are on top the estimated age-specific weekly reproduction numbers for the week starting on August 17, 2020 under the central model (yellow) and the alternative models (black), and below the estimated cumulative contribution of age groups to onward spread as of August 24, 2020. (**A**) Results for contact intensities from and to children aged 0-14 under different τ parameters, see (S82). The value $\tau = 1$ corresponds to the central model. (**B**) Results for contact and intensities from and to children aged 0-14 that are obtained by extrapolating the mobility trends from individuals 18-24 to younger individuals. Dots and error bars indicate the median posterior and the 95% confidence intervals, respectively.

increased from 0.5 to 2, and for individuals aged 10-19 we estimate reproduction numbers ranged from 0.89 [0.79, 1.01] to 0.91 [0.82, 1.02] as τ increased from 0.5 to 2. Reproduction numbers were similar to those obtained under the central model under the alternative model in which mobility trends for individuals aged 18-24 were extrapolated to younger individuals. However these differences had little impact on the estimated contribution of different age groups to onward spread. For children aged $0-9$, we estimate the contribution to onward spread increased from 0.59% [0.38%-0.93%] to 2.23% [1.50%-3.38%] as τ increased from 0.5 to 2. For individuals aged 10-19, we estimate the contribution to onward spread increased from 9.76% [8.96%-10.56%] to 10.13% [9.39%-10.90%] as τ increased from 0.5 to 2. In the alternative model in which mobility trends for individuals aged 18-24 were extrapolated to younger individuals, the estimated contribution to onward spread from children aged 0-9 was 1.74% [1.03%-3.06%], and the estimated contribution to onward spread from individuals aged 10-19 was 11.90% [11.03%-13.25%].

DOI: https://doi.org/10.25561/82551

References

[1] Waksman, A. "Phones, Lambdas and the Joy of Snap-to-Place Technology". Available at https://enterprise.foursquare.com/intersections/article/phones-lambdas-and-the-joy-of-snap-to-place-techn/. 2018.

[2] Foursquare Inc. "Pilgrim SDK". Available at https://enterprise.foursquare.com/products/pilgrim. 2020.

[3] E Dong, H Du, and L Gardner. "An interactive web-based dashboard to track COVID-19 in real time". eng. In: *The Lancet. Infectious diseases* (Feb. 2020), pp. 1473–3099. ISSN: 1474-4457. URL: https://pubmed.ncbi.nlm.nih.gov/32087114https://www.ncbi.nlm.nih.gov/pmc/articles/PMC7159018/.

[4] M Smith et al. "Coronavirus (Covid-19) Data in the United States". Available at https://github.com/nytimes/covid-19-data. 2020.

[5] New York City Department of Health. "Coronavirus data". Available at https://github.com/nychealth/coronavirus-data. 2020.

[6] Alabama Public Health. "Demographics on Deaths". Available at https://alpublichealth.maps.arcgis.com/apps/opsdashboard/index.html#/6d2771faa9da4a2786a509d82c8cf0f7. 2020.

[7] Alaska Department of Health and Social Services Coronavirus Response. "Demographic Distribution of Confirmed Cases". Available at https://coronavirus-response-alaska-dhss.hub.arcgis.com/datasets/summary-tables. 2020.

[8] Arizona Department of Health Services. "COVID-19 Deaths". Available at https://www.azdhs.gov/preparedness/epidemiology-disease-control/infectious-disease-epidemiology/covid-19/dashboards/index.php. 2020.

[9] California Department of Public Health. "Statewide Case Statistics". Available at https://public.tableau.com/views/COVID-19CasesDashboard_15931020425010/Cases?:embed=y&:showVizHome=no. 2020.

[10] Colorado Department of Public Health & Environment. "DPHE COVID19 State-Level Open Data Repository". Available at https://data-cdphe.opendata.arcgis.com/datasets/cdphe-covid19-state-level-open-data-repository?geometry=-125.744%2C35.977%2C-85.358%2C41.950. 2020.

[11] Connecticut Open Data. "COVID-19 Cases and Deaths by Age Group". Available at https://data.ct.gov/Health-and-Human-Services/COVID-19-Cases-and-Deaths-by-Age-Group/ypz6-8qyf. 2020.

[12] Delaware Environmental Public Health Tracking Network. "Demographic Breakdown of Deaths". Available at https://myhealthycommunity.dhss.delaware.gov/locations/state. 2020.

[13] Government of the District of Columbia. "Coronavirus Data". Available at https://coronavirus.dc.gov/page/coronavirus-data. 2020.

[14] Florida Division of Emergency Management. "Coronavirus: characteristics of Florida resident cases". Available at https://www.floridadisaster.org/covid19/covid-19-data-reports/. 2020.

[15] Georgia Department of Public Health. "Deaths in Georgia". Available at https://dph.georgia.gov/covid-19-daily-status-report. 2020.

[16] Idaho Division of Public Health. "COVID-19 Demographics". Available at https://public.tableau.com/profile/idaho.division.of.public.health#!/vizhome/DPHIdahoCOVID-19Dashboard_V2/Story1. 2020.

[17] Illinois Department of Public Health. "Age Demographics". Available at https://www.dph.illinois.gov/covid19/covid19-statistics. 2020.

[18] Indiana State Department of Health. "Statewide Demographics for Deaths". Available at https://www.coronavirus.in.gov/. 2020.

[19] Iowa Department of Public Health. "Deaths by Age Group". Available at https://coronavirus.iowa.gov/pages/outcome-analysis-deaths. 2020.

[20] Kansas Department of Health and Environment. "Death summary". Available at https://www.coronavirus.kdheks.gov/160/COVID-19-in-Kansas. 2020.

[21] Kentucky Department for Public Health. "Deaths by Age Group". Available at https://kygeonet.maps.arcgis.com/apps/opsdashboard/index.html#/543ac64bc40445918cf8bc34dc40e334. 2020.

[22] Louisiana Department of Health. "Cases and Deaths by Age". Available at https://www.arcgis.com/apps/opsdashboard/index.html#/4a6de226701e45bdb542f09b73ee79e1. 2020.

[23] Maine Center for Disease Control & Prevention. "Maine COVID-19 summary". Available at https://www.maine.gov/dhhs/mecdc/infectious-disease/epi/airborne/coronavirus/data.shtml. 2020.

[24] Maryland Department of Health. "Cases and Deaths Data Breakdown by Age Range and Gender". Available at https://coronavirus.maryland.gov/. 2020.

[25] Massachusetts Department of Public Health. "Deaths and Death Rate by Age Group". Available at https://www.mass.gov/info-details/archive-of-covid-19-cases-in-massachusetts. 2020.

[26] Michigan Department of Health and Human Services. "Deaths by Demographic Characteristics". Available at https://www.michigan.gov/coronavirus/0,9753,7-406-98163_98173---,00.html. 2020.

[27] Michigan Department of Health and Human Services. "Data requested to the Department of Health and Human Services". Available at https://github.com/MJHutchinson/US-covid19-data-scraping/blob/master/data/req/michigan%20weekly.csv. 2020.

[28] Mississippi State Department of Health. "COVID-19 Cases and Deaths by Age Group". Available at https://msdh.ms.gov/msdhsite/_static/14,0,420.html. 2020.

[29] Missouri Department of Health and Senior Services. "Deaths by Age Range". Available at https://health.mo.gov/living/healthcondiseases/communicable/novel-coronavirus/results.php. 2020.

[30] State of Nevada Department of Health and Human Services. "Results Filter For Demographics". Available at https://nvhealthresponse.nv.gov/. 2020.

[31] New Hampshire Department of Health and Human Services. "Laboratory-confirmed COVID-19 cases". Available at https://www.nh.gov/covid19/dashboard/summary.htm. 2020.

[32] New Jersey Department of Health. "Deaths by Age Group". Available at https://njhealth.maps.arcgis.com/apps/opsdashboard/index.html#/81a17865cb1a44db92eb8eb421703635. 2020.

[33] New Mexico Department of Health. "Updated New Mexico COVID-19 cases". Available at https://cv.nmhealth.org/newsroom/. 2020.

[34] New York City Department of Health. "NYC COVID-19 Deaths Among Confirmed Cases". Available at https://www1.nyc.gov/site/doh/covid/covid-19-data-archive.page. 2020.

[35] North Carolina Department of Health and Human Services. "Demographic Data". Available at https://covid19.ncdhhs.gov/dashboard/about-data. 2020.

[36] North Dakota Department of Health. "Cases by Age Group". Available at https://www.health.nd.gov/diseases-conditions/coronavirus/north-dakota-coronavirus-cases. 2020.

[37] Oklahoma State Department of Health. "Total Deaths by Age Group". Available at https://looker-dashboards.ok.gov/embed/dashboards/76. 2020.

[38] Oregon Health Authority COVID-19. "Oregon's COVID-19 Cases by Demographic Group". Available at https://public.tableau.com/profile/oregon.health.authority.covid.19#!/vizhome/OregonCOVID-19CaseDemographicsandDiseaseSeverityStatewide/DemographicData?:display_count=y&:toolbar=n&:origin=viz_share_link&:showShareOptions=false. 2020.

[39] Pennsylvania State Department of Health. "Deaths Demographic". Available at https://experience.arcgis.com/experience/cfb3803eb93d42f7ab1c2cfccca78bf7. 2020.

[40] Rhode Island Department of Health. "COVID-19 Rhode Island Data". Available at https://docs.google.com/spreadsheets/d/1c2QrNMz8pIbYEKzMJL7Uh2dtThOJa2j1sSMwiDo5Gz4/edit#gid=31350783. 2020.

[41] South Carolina Department of Health and Environmental Control. "Reported COVID-19 Deaths By Age Group". Available at https://www.scdhec.gov/infectious-diseases/viruses/coronavirus-disease-2019-covid-19/sc-demographic-data-covid-19. 2020.

[42] Tennessee Department of Health. "Case counts by 10-year age groups by day for all of Tennessee". Available at https://www.tn.gov/health/cedep/ncov/data/downloadable-datasets.html. 2020.

[43] Texas Department of State Health Services. "Age of Confirmed Fatalities". Available at https://dshs.texas.gov/coronavirus/TexasCOVID19CaseCountData.xlsx. 2020.

[44] Utah Department of Health. "Total Deaths by Age". Available at https://coronavirus.utah.gov/case-counts/. 2020.

[45] Vermont Department of Health. "COVID-19 Cases and Deaths by Age Group". Available at https://vcgi.maps.arcgis.com/apps/opsdashboard/index.html#/f2d395572efa401888eddceebddc318f. 2020.

[46] Virginia Department of Health. "Cumulative (total) number of COVID-19 cases, hospitalizations, and deaths for each health district in Virginia". Available at https://data.virginia.gov/Government/VDH-COVID-19-PublicUseDataset-Cases_By-Age-Group/uktn-mwig. 2020.

[47] Washington State Department of Health. "Deaths by Age Group". Available at https://www.doh.wa.gov/Emergencies/NovelCoronavirusOutbreak2020COVID19/DataDashboard. 2020.

[48] Wisconsin Department of Health Services. "Percent of COVID-19 deaths by age group". Available at https://hub.arcgis.com/datasets/wi-dhs::covid-19-historical-data-table. 2020.

[49] Imperial College London COVID-19 Response Team. "COVID-19 Age specific Mortality Data Repository". Available at https://github.com/ImperialCollegeLondon/US-covid19-agespecific-mortality-data. 2020.

[50] Y Liu et al. "The reproductive number of COVID-19 is higher compared to SARS coronavirus". In: *Journal of Travel Medicine* (2020). ISSN: 17088305.

[51] Juanjuan Zhang et al. "Changes in contact patterns shape the dynamics of the COVID-19 outbreak in China". In: *Science* (2020).

[52] Qifang Bi et al. “Epidemiology and transmission of COVID-19 in 391 cases and 1286 of their close contacts in Shenzhen, China: a retrospective cohort study”. In: *The Lancet Infectious Diseases* 20.8 (Aug. 2020), pp. 911–919. URL: https://doi.org/10.1016/s1473-3099(20)30287-5.

[53] Andrew T Levin et al. *Assessing the Age Specificity of Infection Fatality Rates for COVID-19: Meta-Analysis & Public Policy Implications*. 2020.

[54] Seth Flaxman, Swapnil Mishra, Axel Gandy, et al. “Estimating the effects of non-pharmaceutical interventions on COVID-19 in Europe”. In: *Nature* (2020), pp. 1–8.

[55] Thang Hoang et al. “A Systematic Review of Social Contact Surveys to Inform Transmission Models of Close-contact Infections”. In: *Epidemiology* 30.5 (Sept. 2019), pp. 723–736. URL: https://doi.org/10.1097/ede.0000000000001047.

[56] Gail E. Potter et al. “Estimating within-school contact networks to understand influenza transmission”. In: *The Annals of Applied Statistics* 6.1 (Mar. 2012), pp. 1–26. URL: https://doi.org/10.1214/11-aoas505.

[57] Timo Smieszek et al. “How should social mixing be measured: comparing web-based survey and sensor-based methods”. In: *BMC Infectious Diseases* 14.1 (Mar. 2014). URL: https://doi.org/10.1186/1471-2334-14-136.

[58] Allison E. Aiello et al. “Design and methods of a social network isolation study for reducing respiratory infection transmission: The eX-FLU cluster randomized trial”. In: *Epidemics* 15 (June 2016), pp. 38–55. URL: https://doi.org/10.1016/j.epidem.2016.01.001.

[59] Mossong Joel et al. “Social Contacts and Mixing Patterns Relevant to the Spread of Infectious Diseases”. In: *PLOS Medicine* 5.3 (Mar. 2008), pp. 1–1.

[60] Joël Mossong et al. “Social contacts and mixing patterns relevant to the spread of infectious diseases”. In: *PLoS Med* 5.3 (2008), e74.

[61] Jan van de Kassteele, Jan van Eijkeren, Jacco Wallinga, et al. “Efficient estimation of age-specific social contact rates between men and women”. In: *The Annals of Applied Statistics* 11.1 (2017), pp. 320–339.

[62] Jan van de Kassteele. “Contact-patterns”. Available at https://github.com/kassteele/Contact-patterns. 2017.

[63] Christopher I. Jarvis et al. “Quantifying the impact of physical distance measures on the transmission of COVID-19 in the UK”. In: *BMC Medicine* 18 (124 2020).

[64] Thomas Hale et al. “Variation in US states’ responses to COVID-19”. In: *Blavatnik School of Government* (2020).

[65] The Hunt Institute. "COVID-19 Resources & Policy Considerations". Available at http://www.hunt-institute.org/covid-19-resources/state-child-care-actions-covid-19/. 2020.

[66] R Verity et al. "Estimates of the severity of COVID-19 disease". In: *Lancet Infect Dis* (2020).

[67] Thomas Wutzler. *lognorm: Functions for the Lognormal Distribution*. R package version 0.1.6. 2019. URL: https://CRAN.R-project.org/package=lognorm.

[68] Andrew T Levin et al. "ASSESSING THE AGE SPECIFICITY OF INFECTION FATALITY RATES FOR COVID-19: SYSTEMATIC REVIEW, META-ANALYSIS, AND PUBLIC POLICY IMPLICATIONS". In: *medRxiv* (2020). eprint: https://www.medrxiv.org/content/early/2020/08/14/2020.07.23.20160895.full.pdf. URL: https://www.medrxiv.org/content/early/2020/08/14/2020.07.23.20160895.

[69] B Carpenter et al. "*Stan*: A Probabilistic Programming Language". In: *Journal of Statistical Software* 76.1 (2017), pp. 1–32. ISSN: 1548-7660. URL: http://www.jstatsoft.org/v76/i01/.

[70] Geert Molenberghs et al. "Belgian Covid-19 Mortality, Excess Deaths, Number of Deaths per Million, and Infection Fatality Rates (8 March - 9 May 2020)". In: *medrXiv* (June 2020). URL: https://doi.org/10.1101/2020.06.20.20136234.

[71] Office for National Statistics. "2011 UK censuses". Available at https://www.ons.gov.uk/census. 2019.

[72] Helen Ward et al. "Antibody prevalence for SARS-CoV-2 in England following first peak of the pandemic: REACT2 study in 100, 000 adults". In: *medrXiv* (Aug. 2020). URL: https://doi.org/10.1101/2020.08.12.20173690.

[73] Public Heath England. "Excess mortality in England, week ending 17 July 2020". Available at https://fingertips.phe.org.uk/static-reports/mortality-surveillance/excess-mortality-in-england-week-ending-17-Jul-2020.html. 2019.

[74] Javier Perez-Saez et al. "Serology-informed estimates of SARS-CoV-2 infection fatality risk in Geneva, Switzerland". In: *The Lancet Infectious Diseases* (July 2020). URL: https://doi.org/10.1016/s1473-3099(20)30584-3.

[75] Roberto Pastor-Barriuso et al. "SARS-CoV-2 infection fatality risk in a nationwide seroepidemiological study". In: *medrXiv* (Aug. 2020). URL: https://doi.org/10.1101/2020.08.06.20169722.

[76] United Nations, Department of Economic and Social Affairs, Population Division. "World Population Prospects 2019, Online Edition. Rev. 1." Available at https://population.un.org/wpp/Download/Standard/Interpolated/. 2019.

[77] The Swedish Public Health Agency. "Detection of antibodies after reviewed covid-19 in blood samples from outpatient care (Interim report 1)". Available at https://www.folkhalsomyndigheten.se/contentassets/9c5893f84bd049e691562b9eeb0ca280/pavisning-antikroppar-genomgangen-covid-19-blodprov-oppenvarden-delrapport-1.pdf. 2020.

[78] The Swedish Public Health Agency. "Weekly report on covid-19, week 24". Available at https://www.folkhalsomyndigheten.se/globalassets/statistik-uppfoljning/smittsamma-sjukdomar/veckorapporter-covid-19/2020/covid-19-veckorapport-vecka-24_final.pdf. 2020.

[79] N Ferguson et al. *Report 9: Report 9: Impact of non-pharmaceutical interventions (NPIs) to reduce COVID19 mortality and healthcare demand*. 2020. URL: https://spiral.imperial.ac.uk:8443/handle/10044/1/77482/.

[80] S Flaxman, S Mishra, A Gandy, et al. *Report 13: Estimating the number of infections and the impact of non-pharmaceutical interventions on COVID-19 in 11 European countries*. 2020.

[81] Anne Cori et al. "A new framework and software to estimate time-varying reproduction numbers during epidemics". In: *American journal of epidemiology* 178.9 (2013), pp. 1505–1512.

[82] Derek K Chu et al. "Physical distancing, face masks, and eye protection to prevent person-to-person transmission of SARS-CoV-2 and COVID-19: a systematic review and meta-analysis". In: *The Lancet* (2020).

[83] Dennis M. Feehan and Ayesha Mahmud. "Quantifying interpersonal contact in the United States during the spread of COVID-19: first results from the Berkeley Interpersonal Contact Study". In: *medrXiv* (2020).

[84] Fiona P. Havers et al. "Seroprevalence of Antibodies to SARS-CoV-2 in 10 Sites in the United States, March 23-May 12, 2020". In: *JAMA Internal Medicine* (July 2020). URL: https://doi.org/10.1001/jamainternmed.2020.4130.

[85] Eli S. Rosenberg et al. "Cumulative incidence and diagnosis of SARS-CoV-2 infection in New York". In: *Annals of Epidemiology* (June 2020). URL: https://doi.org/10.1016/j.annepidem.2020.06.004.

[86] Centers for Disease Control and Prevention. "Commercial laboratory seroprevalence survey data". Available at https://www.cdc.gov/coronavirus/2019-ncov/cases-updates/commercial-lab-surveys.html. 2020.

[87] Conor G McAloon et al. *The incubation period of COVID-19: A rapid systematic review and meta-analysis of observational research*. 2020. URL: https://doi.org/10.1101/2020.04.24.20073957https://www.medrxiv.org/content/10.1101/2020.04.24.20073957v1.

[88] Li Guo et al. "Profiling early humoral response to diagnose novel coronavirus disease (COVID-19)". In: *Clinical Infectious Diseases* (2020).

[89] Juanjuan Zhao et al. “Antibody responses to SARS-CoV-2 in patients of novel coronavirus disease 2019”. In: *Clinical Infectious Diseases* (2020).